Macrophage proliferation machinery leads to PDAC progression, but susceptibility to innate immunotherapy.

Chong Zuo[1], John M. Baer[1], Brett L. Knolhoff[1], Jad I. Belle[1], Xiuting Liu[1], Graham D. Hogg[1], Christina Fu[5], Natalie L. Kingston[1], Marcus A. Brenden[1], Angela Alarcon De La Lastra[1], Paarth B. Dodhiawala[1], Cui Zhou[1], C. Alston James[2,3], Li Ding[1,2], Kian-Huat Lim[1,2], Ryan C. Fields[2,3], William G. Hawkins[2,3], Guoyan Zhao[4,7], Jason D. Weber[1,6], David G. DeNardo[1,2,4*]

Author affiliations:

[1]Department of Medicine, Washington University School of Medicine, St. Louis, MO 63110, USA

[2]Siteman Cancer Center, Washington University School of Medicine, St. Louis, MO 63110, USA

[3]Department of Surgery, Washington University School of Medicine, St. Louis, MO 63110, USA

[4]Department of Pathology and Immunology, Washington University School of Medicine, St. Louis, MO 63110, USA

[5]Department of Biology, Grinnell College, Grinnell, IA 50112, USA

[6]Department of Cell Biology & Physiology, Washington University School of Medicine, St. Louis, MO 63110, USA

[7]Department of Neuroscience, Washington University School of Medicine, St. Louis, MO 63110, USA

[*]Corresponding author: David G. DeNardo, Department of Medicine, 425 South Euclid Ave, St. Louis, MO 63110. ddenardo@wustl.edu

The authors declare no potential conflicts of interest

Abstract

Tumor-associated macrophages (TAMs) are involved in many aspects of cancer progression and correlate with poor clinical outcomes in many cancer types, including pancreatic ductal adenocarcinomas (PDACs). Previous studies have shown that TAMs can populate PDAC tumors not only by monocyte recruitment but also by local proliferation. However, the impact local proliferation might have on macrophage phenotype and cancer progression is unknown. Here, we utilized genetically engineered cancer models, single-cell RNA-sequencing data, and *in vitro* systems to show that proliferation of TAMs was driven by colony stimulating factor-1 (CSF1) produced by cancer-associated fibroblasts. CSF1 induced high levels of p21 in macrophages, which regulated both TAM proliferation and phenotype. TAMs in human and mouse PDACs with high levels of p21 had more inflammatory and immunosuppressive phenotypes. The p21 expression in TAMs was induced by both stromal interaction and/or chemotherapy treatment. Finally, by modeling p21 expression levels in TAMs, we found that p21-driven macrophage immunosuppression *in vivo* drove tumor progression. Serendipitously, the same p21-driven pathways that drive tumor progression, also drive response to CD40 agonist. These data suggest that stromal or therapy-induced regulation of cell cycle machinery can regulate both macrophage-mediated immune suppression and susceptibility to innate immunotherapy.

Summary

TAMs are indicative of poor clinical outcomes and in PDAC their number is sustained in part by local proliferation. This study shows that stromal desmoplasia drives local proliferation of TAMs, and induces their immunosuppressive ability through altering cell cycle machinery, including p21 expression. Serendipitously, these changes in p21 in TAMs also potentially render tumors more sensitive to CD40 agonist therapy.

Introduction

Macrophages are one of the most abundant immune cell types in the tumor microenvironment (Noy and Pollard, 2014). Extensive studies have shown that macrophages can mediate tumor immunosuppression by both directly interacting with cytotoxic T cells and indirectly affecting T cell functions through secretions of immuno-modulators that create a favorable tumor microenvironment (DeNardo and Ruffell, 2019; Cassetta and Pollard, 2018; Doedens et al., 2010). Aside from their immunosuppressive phenotypes, macrophages are known to promote tumor initiation, angiogenesis, local invasion, and metastatic spread (Ruffell and Coussens, 2015; Hao et al., 2012; Cassetta and Pollard, 2018). Unsurprisingly, the presence of macrophages is found to be associated with a poor clinical outcome in many cancers, including pancreatic cancer (Cassetta and Pollard, 2018; Ino et al., 2013). As such, preclinical and clinical studies have focused on targeting tumor-associated macrophages (TAMs). These approaches, often consisting of macrophage-depleting strategies, have yet to show clinical success, in spite of showing efficacies in preclinical models (DeNardo and Ruffell, 2019; Cannarile et al., 2017; Poh and Ernst, 2018; Xiang et al., 2021). This suggests more studies are needed to understand the varied subset of macrophages in tumors and how they impact tumor immunity and cancer progression.

During tissue damage, macrophage numbers can be increased by multiple mechanisms. These include the expansion of tissue resident macrophage populations by local proliferation or new macrophages can be recruited from blood monocytes (Ginhoux and Guilliams, 2016). This balance is likely regulated by both the tissues and types of damage. In pancreatic ductal adenocarcinoma (PDAC), macrophages are derived from both monocyte and tissue resident sources (Zhu et al., 2017). One consistent characteristic of TAMs from both sources in PDAC mouse models is that they are highly proliferative (Zhu et al., 2017). Notably, proliferation of macrophages is not only observed in tumors, but also in injured and inflamed tissues (Hashimoto et al., 2013; Davies et al., 2011; Van Gassen et al., 2015). Under these conditions, inhibiting macrophage proliferation dramatically reduced macrophage number and inflammation (Tang et al., 2015). These observations raised the possibility that inhibiting macrophage proliferation in PDAC might limit the number of tumor-promoting macrophages.

Macrophage proliferative status is commonly associated with underlying macrophage phenotypes. Interferon gamma (IFN-γ) and lipopolysaccharide (LPS) inhibit macrophage proliferation and induce production of nitric oxide (NO) and inflammatory cytokines (Müller et al., 2017; Xaus et al., 2000; Marchant et al., 1994). Interleukin (IL)-4 promotes macrophage proliferation and drives them to a T_H-2 like phenotype (Jenkins et al., 2013). These observations led to the question of whether the macrophage proliferation machinery plays a role in regulating macrophage phenotypes.

In this study, we aimed to understand how the PDAC microenvironment drove local macrophage proliferation and what the net outcome of this was on tumor immunity and progression. We discovered that while cancer-associated fibroblast-induced macrophage proliferation was important for sustaining TAM number, induction of p21 in TAMs by stromal colony stimulating factor-1 (CSF1) resulted in immunosuppression and tumor progression.

Results

Tumor infiltrating macrophages are highly proliferative in PDAC.

To evaluate human PDAC infiltration by TAMs, we utilized multiplex immunohistochemistry (mpIHC) to stain for CD68$^+$ macrophages and CK19$^+$ tumor cells in human PDAC tissues and found that CD68$^+$ TAMs were more frequent in PDAC tissues when compared to adjacent normal pancreas tissues (Fig. 1 A). To further study infiltrating macrophages, we utilized a p48$^-$Cre$^+$/LSL-Kras^{G12D}/p53$^{flox/flox}$ (KPC) genetically engineered mouse model (GEMM), which spontaneously develops PDAC tumors and recapitulates the pathological features of human PDAC (Hingorani et al., 2003, 2005). As in human PDAC, we found that the number of F4/80$^+$ TAMs increased paralleling disease progression (Fig. 1 B and Fig. S1 A). Our previous studies have shown that these PDAC infiltrating TAMs were sustained by both local proliferation and monocyte recruitment in animal models (Zhu et al., 2017). However, these studies did not assess the potential impact macrophage proliferation might have on tumor progression or tumor immunity.

To further investigate the significance and mechanisms of local proliferation of TAMs, we more deeply studied pancreatic tissues from GEMMs and human PDAC patients. We first evaluated the frequency of proliferating macrophages in human PDAC tumors by mass cytometry time of flight (CyTOF). Distinguishing major leukocyte populations based on surface markers, we found that CD68$^+$CD64$^+$ macrophages composed >15% of all infiltrating leukocytes (Fig. 1, C and D and Fig. S1 B). Notably, these macrophages expressed high levels of the proliferation markers PCNA and Ki67 **(**Fig. 1 C**)**. Ki67$^+$ macrophages made-up 20% of total macrophages, and this percentage was significantly higher than that of other leukocyte populations, such as neutrophils (Fig. 1 E and Fig. S1 C). Next, we examined proliferating macrophages in tumors from KPC GEMMs. We observed >10% of F4/80$^+$ cells were also Ki67^{high} by mpIHC analysis (Fig. 1, H and I). In addition, we generated and analyzed single-cell RNA-sequencing (scRNAseq) data from normal pancreas, pancreatic tissues from KPC GEMMs, orthotopic PDAC tumors, and previously published human PDAC datasets (Peng et al., 2019) (Fig. S1 D). In human PDACs, we found populations carrying both myeloid and proliferating signatures (Fig. 1, F and G). Similarly, in mouse datasets, we identified TAMs independent of cell cycle genes (Fig. 1 J and Fig. S1 E), then upon reclustering, we easily identified discrete clusters with cell cycle gene signatures (Fig. 1 K). As expected, this cluster was expanded in PDACs compared to normal tissues (Fig. 1, L and M). Taken together, these data suggest that a significant portion of macrophages are actively proliferating in both murine and human PDAC tissues**.**

Cancer-associated fibroblasts drive macrophage proliferation through CSF1.

To identify the cellular players that drove macrophage proliferation in PDAC, we investigated the cellular composition in the PDAC tumor microenvironment (TME). As others have shown, PDAC tumors contain dense fibrotic stroma (Elyada et al., 2019; Schnittert et al., 2019; Waghray et al., 2013), and immunohistochemistry (IHC) staining of PDAC tissues from KPC GEMMs revealed abundant PDPN$^+$ cancer-associated fibroblasts (CAFs) surrounding CK19$^+$ tumor cells (Fig. 2 A). We next performed proximity analysis and found that TAMs were within 100 μm to both tumor cells and CAFs, but more frequently closer to PDPN$^+$ CAFs than CK19$^+$ tumor cells (Fig. 2 B). To test whether fibroblasts and tumor cells drove macrophage proliferation, we co-cultured bone marrow-derived macrophages (BMDMs) with either PDAC cell lines from KPC GEMMs or primary pancreatic fibroblasts. We found that PDAC cells and fibroblasts both led to increases in macrophage proliferation, as measured by BrdU incorporation. However, fibroblasts induced significantly higher levels of proliferation and increases in the number of macrophages (Fig. 2 C). Additionally, macrophage proliferation was not further enhanced by triple culture of PDAC cells and fibroblasts, suggesting the effects were not additive (Fig. 2 C, grey bars). To determine if fibroblasts induced macrophage proliferation in a cell contact-dependent manner or through secreted factors, we repeated these assays in a Transwell system. We found that without direct contact to BMDMs, fibroblasts still drove macrophage proliferation at almost a comparable level as the strong mitogen, CSF1 (Fig. 2 D).

To identify the relevant secreted factors from fibroblasts that drove macrophage proliferation, we profiled 111 soluble factors derived from two PDAC cell lines (KP-1, KP-2), or fibroblast-conditioned media and found that fibroblasts secreted significantly higher levels of CSF1 (Fig. 2 E). We measured the levels of CSF1 secreted by fibroblasts and three different PDAC cell lines (KP-1, KP-2, and KI) through ELISAs and confirmed that only fibroblasts produced high levels of CSF1 (Fig. 2 F). Next we sought to determine if CSF1 was necessary and sufficient for fibroblasts to drive macrophage proliferation. Both the addition of neutralizing αCSF1 IgG to the co-culture of BMDMs and fibroblasts, and knocking-down CSF1 in fibroblasts by siRNA in Transwell assays, resulted in a loss of fibroblast-driven macrophage proliferation and number expansion **(**Fig. 2, G,H and I**)**. These data suggest that CSF1 secreted from fibroblasts is both necessary and sufficient for macrophage proliferation *in vitro*.

To confirm CAFs drive TAMs proliferation in *in vivo* pancreatic tissue, we analyzed scRNAseq datasets from both mouse and human. In a previously published dataset (Hosein et al., 2019) of pancreatic tumors from three GEMM models, including *Kras*$^{LSL\text{-}G12D/+}$*Ink4a*$^{fl/fl/}$*Ptf1a*$^{Cre/+}$ *(KIC), Kras*$^{LSL\text{-}G12D/+}$*Trp53*$^{LSL\text{-}R172H/+}$*Ptf1a*$^{Cre/+}$ *(KP*$^{R172H/+}$*C),* and *Kras*$^{LSL\text{-}G12D/+}$*Trp53*$^{fl/fl/}$*Pdx1*$^{Cre/+}$ (*KPfC*), we found that fibroblasts expressed higher levels of CSF1 than other cell types (Fig. 3, A and B). In a human PDAC dataset (Peng et al., 2019) comprised of 21 PDAC samples, fibroblasts also expressed a higher level of CSF1 than tumor cells and other cells within the TME (Fig. 3, C and D). Others have also detected CSF1 in the cultures of primary CAFs from PDAC patients (Samain et al., 2021). Collectively, these data suggest that fibroblasts are the main producers of CSF1 in the PDAC TME. Next, we injected αCSF1 IgG into mice bearing orthotopic KP-2 tumors and measured macrophage proliferations 12 and 24 h after the injection. Similar to the *in vitro* experiments, we found a significant reduction in the percentage of macrophages undergoing proliferation, measured by BrdU incorporation (Fig. 3, E, F and G). We have previously shown that sustained CSF1 depletion, exceeding 48 h, led to macrophage depletion by apoptosis (Zhu et al., 2014). To eliminate the possibility that the decrease in proliferation came from macrophage death, we quantified macrophage numbers and found no change (Fig. 3 H). Additionally, we found that proliferation of monocytes was minimal and not significantly affected by αCSF1 IgG treatment (Fig. 3 I), confirming that the reduction of proliferation was mainly from macrophages. Taken together, these data suggest that CSF1 secreted by cancer-associated fibroblasts drives local macrophage proliferation in pancreatic cancer.

The p21 cell cycle-dependent kinase inhibitor was induced in TAMs by CAF-derived CSF1.

We next asked whether the macrophage proliferation machinery regulated by CAF-derived CSF1 could impact the TAM phenotype. We first examined the expressions of several critical cell cycle regulators in BMDMs following treatment with either CSF1, the proliferative mitogen, or lipopolysaccharide (LPS), which is known to blunt macrophage proliferation (Liu et al., 2016) (Fig. S2 A). We found that when BMDMs were treated with CSF1, overall protein levels of c-Myc and cyclin D1 were upregulated while p27$^{\mathrm{Kip1}}$ was reduced (Fig. 4 A). BMDMs treated with LPS showed the opposite result. These changes are consistent with the existing roles of cell cycle promoters (c-Myc and cyclin D1) and a cell cycle inhibitor (p27$^{\mathrm{Kip1}}$) (Liu et al., 2016; Matsushime et al., 1991). However, surprisingly, we found p21$^{\mathrm{Waf/Cip1}}$, a cell cycle inhibitor (Cazzalini et al., 2010; Dutto et al., 2015; Brugarolas et al., 1999), was strongly induced by both CSF1 and CAF co-culturing (Fig. 4, B and D). To further investigate this p21 induction, we performed a kinetic study of p21 expression in BMDMs and found that the p21 protein was induced by CSF1 within 6–12 h, which was prior to S phase entry at 24–48 h after CSF1 administration, as measured by BrdU (Fig. 4, B and C). Similar kinetics and cell cycle transit were found when BMDMs were cultured with fibroblasts in a Transwell assay (Fig. 4, D and E). These data suggest that p21 induction by stoma-derived CSF1 could impact both macrophage cell cycle and phenotype.

To test if p21 induction impacted macrophage phenotype, we knocked-down p21 expression in BMDMs by siRNA in the presence of CSF1. We found that p21 knockdown resulted in a significant increase in the number of macrophages that entered S phase, confirming p21's inhibitory role in the G1/S transition (Fig. S2 B and C). To assess macrophage phenotypic changes after p21 knockdown, we performed gene profiling analysis followed by RT-qPCR validation of altered gene expressions. Transcription profiling revealed > 300 genes that were differentially expressed in BMDMs upon p21 knockdown in the presence of tumor conditioned medium (Fig. 4 F). Overrepresentation analysis of the differentially expressed genes demonstrated that p21 knockdown in BMDMs resulted in the upregulation of genes involved in cell cycle progression, as expected, but also unexpectedly, it upregulated interferon α and γ responses (Fig. 4 G)**.** RT-qPCR validation also found upregulation of interferon-related genes, IFIT3, CD40, IFN-α and IFN-β. Notably, gene expression of cyclins involved in early cell cycle stage (G1), CCND1, CCNE, were unchanged, while CCNA, an S phase cyclin, was upregulated (Fig. 4 H). Together, these data suggest that in addition to its canonical role in regulating S phase entry, p21 might suppress interferon signaling pathways. In a CSF1-rich TME like PDAC, elevated p21 expression in macrophages might play a prominent role in impairing tumor immunity (Hervas-Stubbs et al., 2011).

Based on the significant presence of CSF1-producing CAFs in the PDAC TME, we hypothesized that p21 might be chronically high in TAMs and thus might drive their immune-suppressive phenotype. We first evaluated p21 expression in human PDAC tumors by CyTOF, and found PDAC TAMs frequently expressed high levels of p21 (Fig. 4 I). Similarly, KPC tumors also had significant numbers of F4/80^{+} TAMs expressing high levels of p21 evaluated by mpIHC (Fig. S2, H and I). Finally, scRNAseq analysis suggested that TAMs from both human and murine PDAC tissues had higher levels of p21 gene expression than macrophages in normal tissues (Fig. 4 J; Fig. S2 F). The elevation of p21 in PDAC tumors could be a result of increased number of macrophages entering cell cycle as shown in Figure 1, G and L. However, we observed in CyTOF, TAMs that were high in p21 expression, were not necessarily high in the expression of PCNA or Ki67 (Fig. 4 I; Fig. 1 C), suggesting p21 expression was not only up in proliferating TAMs. In addition, we did not find a significant difference in the p21 protein levels between Ki67$^+$ vs. Ki67$^-$ TAMs by CyTOF, nor did we find significant difference in p21 gene expression in proliferating and non-proliferating clusters of TAMs in scRNAdeq data (Fig. S2, D and G). Collectively, these results suggest that elevated p21 expression in PDAC TAMs is unlikely to be solely caused by cell cycle entry/progression, it may become elevated by other factors in the TME and regulate TAMs phenotype.

To further assess the potential phenotypic differences in TAMs based on p21 expression, we generated and analyzed data from four scRNAseq data sets, including one from human (Peng et al., 2019) and three from PDAC mouse models (Hosein et al., 2019). We identified macrophage populations in each mouse dataset and myeloid populations in human dataset based on known macrophage markers after unsupervised clustering and UMAP projection (Fig. 1, F and J; Fig. 3 B). We then stratified macrophages (myeloid cells in human) based on p21 gene expressions to the p21^{High} and p21^{Low} grouped in each data set (Fig. 4 K). Notably, UMAP dimension reduction revealed the similar spatial distributions of p21^{High} and p21^{Low} macrophages in tumors from mouse GEMM and orthotopic models, suggesting shared characteristics among the same group of TAMs in different models (Fig. S2 E). To understand what these common phenotypes were, we performed Gene Set Enrichment Analysis between p21^{High} and p21^{Low} macrophages in each dataset. Across all four datasets and both species, we found that hallmarks typically associated with the tumor necrosis factor alpha (TNF-α) signaling pathway, hypoxia, and STAT5 signaling were upregulated in p21^{High} macrophages (p21^{High} myeloid cells in human), while oxidative phosphorylation pathways were upregulated in p21^{Low} macrophages (p21^{Low} myeloid cells in human) (Fig. 4 L). Although TNF-α and its signaling pathway are proinflammatory, they are frequently considered immunosuppressive in tumors. In this respect, TNF-α can mediate T cell exhaustion, CD8$^+$ T cell death, and expansion of myeloid-derived suppressor cells and regulatory T cells (T$_{Regs}$) to promote tumor progression and metastasis (Salomon et al., 2018; Balkwill, 2006). Consistent with the enrichment for TNF-α via the NF-κB signaling pathway, expressions of IL-1α, IL-1β, and NF-κB components were also upregulated in p21^{High} macrophages (Fig. 4 M). Together, these data suggest that TAMs with high p21 expression acquire an inflammatory but potentially immunosuppressive gene signature.

PDAC patients are frequently treated with cytotoxic chemotherapies, that can impact both tumor cells as well as stromal cells. Therefore, we sought to next determine if chemotherapy could impact TAM proliferation and p21 expression and thus influence TAM-immunosuppressive programs. First, we treated KPC GEMM with modified FOLFIRINOX (5-FU, Irinotecan, and Oxaliplatin), and analyzed p21^{High}F4/80$^+$ TAMs 24 hours later by mpIHC. We found that the number of p21^{High} TAMs significantly increased after chemotherapy treatment (Fig. 4 N). To determine if this was a direct effect of chemotherapeutic exposure, we treated BMDMs with four different chemotherapeutics for 24 h and observed similar inductions of p21 (Fig. 4 O). Finally, to assess if this induction of p21 by chemotherapy correlates with changes in macrophage phenotype, we analyzed TAMs from KPC GEMMs treated with vehicle or gemcitabine and paclitaxel (GEM/PTX) by scRNAseq. We found striking similarity in the pathways enriched in TAMs from mice treated with GEM/PTX compared to vehicle and pathways found when we stratified TAMs in vehicle treatment mice by p21 expression (Fig. 4 P). Similarly, TAMs from GEM/PTX treated KPC mice showed higher expression of the $p21^{High}$ gene signature when compared to vehicle. (Fig. S2 J). These data suggested that p21 was induced by both stromal interaction and amplified by chemotherapy treatment, and correlated with inflammatory and likely immunosuppressive phenotypes in PDAC TAMs. Next, we analyzed the $p21^{High}$ TAM signature in TCGA data sets and found strong correlation with signatures of “T cell exhaustion” (Tirosh et al., 2016) and “immune escape” (Lin et al., 2007) (Fig. 4 Q). Additionally, the p21 signature strongly correlated with CSF1 expression (Fig. 4 Q). These data suggest that stromal-CSF1 induced p21 expression in TAMs may drive dysfunctional T cell mediated tumor control.

Expression of p21 drove the tumor promoting phenotype in macrophages.

To better understand the impact of induction of p21 expression on the macrophage phenotype, and on the PDAC TME, we engineered a mouse designed to constitutively express p21 in myeloid cells. The construct contained the *p21* gene under the control of a CAG promoter and a lox-stop-lox case. Downstream of the *p21* gene, the construct also contained an internal ribosome entry site (IRES) and YFP gene for visualization. The construct was then integrated into the ROSA locus of pure C57/B6 mice (ROSA-CAG-LSL-p21-IRES-YFP, $p21^{+/wt}$) (Fig. 5 A). Then, $p21^{+/wt}$ mice were crossed with LysMCre mice to specifically induce p21 expression in macrophages. The resulting $LysM^{+/+}/p21^{+/wt}$ mice were termed “p21 constitutive expression” ($p21^{CE}$) mice.

To confirm that p21 expression was induced in macrophages from $p21^{CE}$ mice, we measured p21 protein levels in BMDMs from $p21^{CE}$ mice in the presence and absence of CSF1. We found BMDMs from $p21^{CE}$ mice expressed significantly higher levels of p21 protein in the absence of CSF1 compared to control BMDMs (Fig. 5 B). However, in the presence of CSF1, which strongly induced p21 expression in wildtype BMDMs (Fig. 4, A and B), both $p21^{CE}$ and $p21^{WT}$ BMDMs had similar p21 expressions. These data indicated that macrophages from the $p21^{CE}$ mouse model retained high p21 expression without stimuli and that the expression was at a physiological level comparable to CSF1 exposure or fibroblast co-cultures.

Given LysMCre is known to be expressed in various myeloid compartments, including granulocytes and monocytes (Abram et al., 2014), we next examined whether the hematopoietic system was altered in $p21^{CE}$ mice. Flow cytometry analysis of non-tumor-bearing $p21^{CE}$ mice revealed that YFP, a surrogate for transgenic p21, was mainly expressed in mature monocytes, macrophages, and granulocytes/neutrophils in the blood, bone marrow, spleen, and pancreas, but minimally expressed in bone marrow progenitors and lymphocytes (Fig. 5 C). Corresponding to the lack of expression in progenitor cells, we did not find major changes in the cellular composition of bone marrow or blood in p21^{CE} mice compared to controls, as assessed by flow cytometry or by complete blood count analysis (Fig. 5 D; Fig. S3, A, B and C). Taken together, these data suggested that p21 was expressed mainly in mature myeloid cells in p21^{CE} mice, but minimal in progenitors and it did not greatly impact hematopoiesis.

As shown above in the scRNAseq data and gene profiling analysis after p21 siRNA knockdown, p21 expression regulated the macrophage phenotype. To assess whether macrophages from p21^{CE} mice had similar phenotypic changes, we profiled gene expressions of BMDMs from p21^{WT}, p21^{CE}, and p21$^{-/-}$ (Jax mice) mice in the presence of CSF1. We found that inflammatory cytokines/chemokines, CXCL1, CXCL2, IL-1α, IL-1β, IL-6, and TNF-α were upregulated in p21^{CE} mice but reduced or not changed in p21$^{-/-}$ mice (Fig. 5 E). In addition, the interferon regulatory factor 4 (IRF4)-mediated macrophage alternative activated genes, YM1 and transforming growth factor beta (TGF-β), were also upregulated. In contrast, p21$^{-/-}$ BMDMs had elevated levels of the interferon-related genes, IRF1, BATF, IFIT3 and CD40, which were consistent with the changes in macrophages with siRNA-mediated knockdown of p21 (Fig. 5 E and Fig. 4 H). Taken together, these data suggest that constitutive p21 expression regulates the macrophage phenotype and represses anti-tumor immunity.

Next, we examined the impact of constitutive p21 expression in myeloid cells on PDAC progression. We orthotopically implanted KP-2 cells into p21^{CE} and p21^{WT} mice and analyzed tumors at the end point by flow cytometry. Similar to YFP expression patterns in non-tumor-bearing mice, we found in PDAC tissues that the majority of TAMs, monocytes, and neutrophils were YFP^{+} , but the vast majority of tumor infiltrating cDCs, lymphocytes, and bone marrow progenitors were YFP^{-} (Fig. 5 F). Corresponding to lack of expression in DCs, we found no major changes in the numbers of cDC1s and cDC2s in pancreatic tissues from p21^{CE} tumor-bearing mice (Fig. S3 D). Additionally, the number of other myeloid cells that were not largely dependent on proliferation was also not changed in p21^{CE} when compared to p21^{WT} (Fig. S3, D - F). With constitutive expression of p21, we found a reduction in TAM proliferation, as measured by BrdU, as well as a decrease in total TAM numbers (Fig. 5, G and H). These data suggest that local proliferation of TAMs is necessary to sustain a local TAM pool. Interestingly, while TAM depletion in other studies typically slowed tumor growth (Zhu et al., 2014; Borgoni et al., 2018; Candido et al., 2018), we saw a significant increase in tumor burden in p21^{CE} mice (Fig. 5 I). These data suggest that changes in myeloid phenotype mediated by p21 drives tumor progression. Before evaluating the phenotypic changes of TAMs in p21^{CE} mice, we examined the tumor promoting effects on other tumor models. Similar to orthotopic KP-2, the PDA.69 PDAC model (Lee et al., 2016) and PyMT mammary tumor model showed decreased TAM proliferations and numbers, but accelerated tumor progression (Fig. 5, J and K). Together, these data suggest that constitutive expression of p21 in myeloid cells reduces TAM proliferations and numbers, but also alters TAM phenotype to drive tumor progression.

The p21 expression in macrophages led to an inflammatory but immunosuppressive phenotype.

We next sought to explore how high p21 expression in myeloid cells affected their phenotype *in vivo*. We conducted scRNAseq analyses on sorted CD45$^+$ cells from PDAC tissues in p21^{WT} and p21^{CE} mice. An unsupervised clustering algorithm identified 19 clusters (Fig. S4 A), which mainly included C1qa-expressing macrophages, Ly6C2-expressing monocytes, S100a8-expressing granulocytes, Cd3d-expressing T cells, and Ms4a1-expressing B cells (Fig. 6 A**;** Fig. S4 B). To assess transgene expression, we analyzed the expression of YFP sequences. Consistent with flow cytometry data, myeloid compartments, including macrophages, monocytes, neutrophils, and eosinophils had high YFP expressions, while DCs had minimal and non-myeloid cells had no expression (Fig. 6 B).

To more accurately define myeloid subpopulations identified by scRNAseq and evaluate the phenotypic changes in each, starting from TAMs, we computationally separated macrophage/monocyte clusters and reanalyzed these at a higher resolution. This approach generated 17 clusters, which were grouped into four major populations, including macrophages with high MHCII expression (MHCII^{hi} Macs), low MHCII expression (MHCII^{low} Macs), monocytes (Mono, Mono2), and proliferating macrophages (ProMacs) (Fig. 6 C). After identifying major macrophage subsets, we first performed cell cycle analysis on all macrophages and confirmed that their proliferations were reduced (Fig. 6 D). Second, we observed that a higher percentage of TAMs in p21^{CE} was in the MHCII^{low} cluster, and that this change was also observed at the protein level by flow cytometry (Fig. 6, E and F), indicating that TAMs in p21^{CE} potentially had impaired cross-presentation. Third, we performed Gene Set Enrichment Analysis (GSEA) between p21^{CE} TAMs and p21^{WT} TAMs and found that consistent with *in vitro* experiments, TAMs in p21^{CE} were enriched in TNF-α signaling, as well as pathways associated with hypoxia and inflammatory responses (Fig. 6H**;** Fig. S5 A). Notably, we also observed downregulation of genes associated with antigen processing and presentation of H2-Aa, H2-Ab1, H2-Eb1, and Cd74, and with the complement components of C1qa, C1qb, and Lyz, whereas tissue remodeling markers of Arg1, Mmp19, Vegfa, and Mmp9 were upregulated in TAMs from p21^{CE} tumor-bearing mice (> 1.5-fold, adjusted $p < 0.05$) (Fig. 6 I). Taken together, these data suggest that TAMs in p21^{CE} are more inflammatory, characterized by high TNF-α signaling, and are more immunosuppressive, characterized by both impaired anti-tumor functions and expressions of M2-like gene signatures. In addition, we found an increase of eosinophils within the TME of PDAC from p21^{CE} tumor-bearing mice **(**Fig. S4 C**),** which further illustrated that the TME was more inflammatory.

To further confirm that the p21^{CE} model recapitulated the characteristics of p21^{High} TAMs identified in mouse PDAC tissues in Fig. 4 K, we examined the expression levels of p21^{High} gene signature defined in Fig. 4 M in TAMs from p21^{CE} and p21^{WT} tumor-bearing mice. We found that TAMs in p21^{CE} expressed significantly higher levels of the p21^{High} gene signatures (Fig. S4 D). In addition, a gene encoded for the common γ chain of the FC receptor (*Fcer1g*) was significantly reduced in p21^{High} TAMs across three mouse scRNAseq datasets in Fig. 4 M. Cross-linking of FcγRs and the common γ chain is required for IgG-mediated response and phagocytosis (Castro-Dopico and Clatworthy, 2019). Therefore, we evaluated whether p21^{CE} macrophages had impaired FcγR-mediated phagocytosis. We cultured BMDMs from p21^{CE}

or p21^{WT} non-tumor-bearing mice with IgG-coated beads and found significantly less phagocytosis in p21^{CE} BMDMs **(**Fig. 6 G**)**. These data suggest TAMs with high p21 expression have impaired effector functions which could contribute to tumor progression. Finally we analyzed a gene expression signature derived from TAMs in p21^{CE} mice in human PDAC expression datasets. Our analysis found that the p21^{CE} signature was also associated with “immune escape” signatures (Lin et al., 2007) and poor progression free survival (Fig. 6, J and K).

To understand the changes in other myeloid cells from p21^{CE} mice, we compared the numbers of significantly changed genes in each myeloid population between the two genotypes. We found that TAMs showed the largest number of differentially expressed genes (DEGs) (80 genes), followed by monocytes (34 genes), and only a few genes in neutrophils and granulocytes (Fig. S4 F). These data suggest macrophages are likely the predominant driver of tumor burden differences. To confirm macrophage contribution to the tumor difference between the two genotypes, we administered αCSF1 IgG and clodronate-containing liposomes to p21^{CE} and p21^{WT} tumor-bearing mice throughout tumor development. We found that the number of TAMs was significantly reduced, while the number of monocytes did not after the treatment in both genotypes of mice (Fig. S4, I and J). Only in the setting of macrophage depletion were the tumor promoting effects observed in p21^{CE} mice abolished **(**Fig. S4 H). Therefore, these data suggest that macrophages are the main driver for tumor acceleration in p21^{CE} mice.

Although YFP was not significantly expressed by DCs, DCs play a critical role in antigen processing and presentation as well as CD8^{+} T cell activity and could potentially affect tumor progression (Gardner and Ruffell, 2016). To evaluate the changes in DCs in p21^{CE} tumors, we reclustered DC populations from scRNAseq data at a higher resolution and identified seven major subsets: cDC1, cDC2a, cDC2b, migratory DC (MigDC), pDC, and proliferating cDC1 and cDC2 (Fig. S4 E). The cDC1 expressed classical DC1 markers of *Xcr1*, *Clec9a*, and also *Baft3* and *Irf8*, while the cDC2 subsets expressed *Cd11b*, *Irf4*, and *Sirpa*, and were further separated into cDC2a and cDC2b based on *Epcam* expression (Merad et al., 2013; Kaplan, 2017). We did not observe significant changes in the percentages of cDC1s, cDC2s, migratory DCs, and proliferating DCs as the total number of DCs between two genotypes, nor did we observe a change in genes associated with cross-presentation. We saw a decrease in pDCs and an increase of cDC2bs as the percentage of total DCs (Fig. S4 F). Because pDCs are one of the major producers of type-I interferon (Koucký et al., 2019) and could potentially drive anti-tumor immunity, this reduction could impact tumor immune suppression.

The p21 expression in macrophages impaired effector T cells.

To determine if impaired antigen processing and presentation in macrophages directly affected T cell numbers and functions, we reanalyzed T cell clusters from the scRNAseq experiment at a higher resolution. Unsupervised clustering generated 12 clusters and were manually assigned into natural killer cells (NK cells), regulatory T cells (T_{Regs}), two clusters of CD4^{+} (CD4#1 and CD4#2), two clusters of CD8^{+} (CD8#1 and CD8#2), double negative T cells (DNs), and a gamma delta T cell based on known cell type markers (Fig. 7 A). Among CD8$^+$ T cells, cluster #2 expressed the higher effector genes, *Gzma*, *Gzmb*, and *Cd74*, and therefore was considered as cytotoxic effectors (Fig. 7 A). We observed that this CD8$^+$ effector cluster was reduced as a percentage in p21^{CE} tumor-bearing mice (Fig. 7 B) and the expressions of effector genes, *Gzma*, *Gzmk*, *Klrg1*, were also significantly lower (Fig. 7 D). In contrast, we saw an increase in the percentage of CD4#2 T cell populations, which are T$_H$2 polarized, with high levels of Gata3, *IL-4* and *IL-13* (Fig. 7 B) (Zheng and Flavell, 1997). If mapping the upregulated genes in cytotoxic CD8$^+$ T cells from p21^{CE} tumors to known signaling pathways, we found enrichment in apoptosis and IL-2-STAT5 signaling, suggesting overexpressed p21 in macrophages may cause more cytotoxic CD8$^+$ T cell death (Fig. 7 C). To confirm this, we co-cultured activated CD8$^+$ T cells with BMDMs generated from p21^{CE} and p21^{WT} mice *in vitro*, and found p21^{CE} BMDMs led to more apoptosis of CD8$^+$ T cells, measured by 7-AAD (Fig. 7 E). To extend the findings to human PDAC patients, we analyzed the correlations between the p21^{CE} signature in TAMs with "T cell exhaustion"(Tirosh et al., 2016) and found strong positive correlations (Fig. 7 K). Taken together, these data suggest high p21 expression in TAMs dampens cytotoxic CD8$^+$ T cell mediated tumor control.

To corroborate these findings, we used a T cell-focused CyTOF panel. CD45$^+$TCRb$^+$CD90$^+$NK1.1$^-$ TCR$^-$$\gamma\delta$T$^-$ cells were selected for further clustering based on 20 T cell functional markers. This approach generated 18 clusters that could be mainly grouped into three major populations: CD4$^+$ T cells, regulatory CD4$^+$ T cells (T$_{Regs}$), and CD8$^+$ T cells (Fig. 7, F and G). We next evaluated changes in each subpopulation and found a significant decrease in the numbers of cytotoxic effectors (cluster 4), which expressed high levels of granzyme B and KLRG1. In addition, we observed an expansion of the CD4$^+$T$_{reg}$ (cluster 5) that expressed high levels of PD1 (Fig. 7 H). In addition, we found that CD8$^+$ T cells as a whole in p21^{CE} tumors expressed lower levels of KLRG1 and CD90, but higher levels of CD44, Tim3, and PD1, indicating a more exhausted and less functional phenotype (Fig. 7 I). Finally, to determine whether accelerated tumor progression in p21^{CE} mice was driven by T cells, we depleted CD4$^+$ and CD8$^+$ T cells in both p21^{CE} and p21^{WT} mice through injection of αCD4 IgG and αCD8 IgG. We no longer observed difference in tumor burdens between the two groups (Fig. 7 J). These data suggest that p21-driven TAM immunosuppressive phenotype not only reduces the number of anti-tumor T cells but also impairs the functions of remaining T cells.

We next asked whether innate immune agonist therapy, CD40 agonist, could reeducate TAMs and restore their effector functions (Coveler et al., 2020). To test this, we treated p21^{CE} and p21^{WT} mice bearing orthotopic KP-2 tumors with CD40 agonist therapy and found that while the dual treatment had limited effect on p21^{WT} mice, it dramatically reduced the tumor burden in p21^{CE} mice (Fig. 7 L). These data suggest, although stromal or chemo-induced p21 expression drives an inflammatory and immunosuppressive phenotype in TAMs, these same pathways may make tumor uniquely susceptible to CD40 agonist therapy.

Discussion

Macrophage proliferation has been observed in several non-cancer pathological conditions, including helminth infections (Jenkins et al., 2011), atherosclerosis (Tang et al., 2015), and obesity-associated adipose tissues (Amano et al., 2014). In these conditions, proliferation of macrophages, albeit under the control of different factors, is necessary to sustain total macrophage numbers at each tissue site. In our studies, we found in pancreatic tumors that macrophage proliferation was mainly driven by CAF-derived CSF1. These data implied that although the general need for macrophage expansion was common, the activated signaling pathways and resulting macrophage phenotypes were largely tissue- and context-dependent. Stromal rich tumors may increase TAM numbers more frequently by local proliferation. Interestingly, CSF1 levels were reported to be higher in the blood of patients suffering from melanoma, breast cancer, or pancreatic cancer. In these patients and also in corresponding mouse models, macrophages were found to be proliferative (Bottazzi et al., 1990; Franklin et al., 2014; Tymoszuk et al., 2014). These data suggested that CSF1-driven macrophage proliferation was common in multiple cancer types.

An earlier study examined the CSF1 effects on CSF1R-expressing human breast cancer cell lines, and found that CSF1 inhibited cell proliferation through inducing p53 independent, but MAPK-dependent, p21 expression (Lee et al., 1999). This result may seem contradictory to ours as we showed CSF1 induced BMDM proliferation. However, we also showed that knocking-down p21 expression or constitutively expressing it promoted or inhibited macrophage proliferation. These data suggested that CSF1 induction of p21 in macrophages acted as a checkpoint for S phase entry. The ultimate cell cycle transit required additional signaling, and the signals could be synthesized according to the expression level of p21. One group reported that Raf signal intensity determined either induction of DNA synthesis or inhibition of proliferation in fibroblasts by $p21^{Cip1}$ expression levels (Sewing et al., 1997). A recent study further showed that p21 not only determined the cell cycle fate of mother cells but could also be carried into daughter cells and regulated the proliferation after mitosis (Yang et al., 2017). Therefore, it is not surprising that the p21 expression level is known to protect cells from chemotherapy-induced apoptosis (Hsu et al., 2019).

Aside from p21's canonical role as a cell cycle checkpoint, several groups reported its role in regulating inflammation, with some contradictory results. One group demonstrated that $p21^{-/-}$ mice were more sensitive to LPS-induced septic shock due to inflammation (Trakala et al., 2009). Likewise, $p21^{-/-}$ mice showed enhanced experimental inflammatory arthritis and severe articular destruction (Mavers et al., 2012).Contrastingly, in a serum transfer model of arthritis, $p21^{-/-}$ mice were more resistant (Scatizzi et al., 2006). Furthermore, disruption of p21 attenuated lung inflammation in mice (Yao et al., 2008). These data suggested that regardless of whether p21 promoted or inhibited inflammation, it was established that p21 regulated inflammation. In a chronic pancreatitis model, one study found that p21 expression was significantly increased overall, while knocking-down its expression resolved inflammation and prevented pancreatic injury through reducing the release of NF-κB-mediated proinflammatory cytokines, such as TNF-α, IL-6, and CXCL1(Seleznik et al., 2018). These data suggested that at least in the pancreas, p21 played a role in promoting inflammation, independent of KRAS mutations that are commonly observed in PDAC and are known to drive inflammation (Kitajima et al., 2016). However, this study did not identify the main drivers for p21-mediated inflammation.

Macrophages are known to exhibit plasticity, which gives them the capability to quickly respond to environmental challenges. Expression levels of p21 could be an important regulator in macrophage plasticity. Expression of p21 inhibited macrophage activation during LPS-induced septic shock, as p21$^{-/-}$ macrophage expressed higher levels of CD40 and enhanced activation of NF-κB (Trakala et al., 2009). One study further demonstrated that expression of p21 acted more like a buffer system for inflammation as it could adjust the equilibrium between p65-p50 and p50-p50 NF-κB pathways to mediate macrophage plasticity in LPS treatment (Rackov et al.). However, none of these studies investigated p21 effects on macrophage polarization in tumor settings. From scRNAseq data, we showed that stratifying macrophages based on p21 expressions into p21^{Hi} and p21^{Low} resulted in two phenotypically distinct macrophages independent of the cell cycle, with the first being more inflammatory. TNF-α and NF-κB were upregulated when p21 expression was high, which is consistent with previous findings. We further illustrated that constitutive expression of p21 in macrophages impaired their phagocytosis capabilities *in vitro*, lowered expression of genes associated with antigen cross-presentation in orthotopic PDAC tumors, and hindered cytotoxic T cell functions, which eventually led to faster tumor progression. These observations are important because as we showed both stromal interaction and therapeutic interventions targeting cell cycle could induce p21 expression in TAMs and lead to an inflammatory yet immunosuppressive phenotype. Given TAMs are usually abundant in TME, these p21-driven phenotypic changes could eventually lead to resistance for treatments.

We also found that in human and mouse PDACs, although p21 expression was highest in macrophages, it was expressed by other myeloid populations. If p21 regulates inflammatory responses through NF-κB in macrophages, it is possible that other immune cells mediate inflammation, like granulocytes and neutrophils, which could also be polarized by p21 in a similar way. One group observed that p21 expression in neutrophils regulated inflammation in infections (Martin et al., 2016). In addition, we observed that p21 expression was induced by chemotherapy not only in macrophages, but also in other myeloid cells, which suggested that inflammatory but immunosuppressive phenotypes could be further strengthened by myeloid cells, in addition to macrophages.

Understanding how the TME and cancer cell intrinsic factors regulate macrophage tumor supportive vs. tumor suppressive functions is critical to therapeutically targeting TAMs in cancer patients. In total, our data suggested that CAF-induced macrophage proliferation was important for sustaining TAM number and induction of p21, which also resulted in immunosuppression and tumor progression. Lastly, expression of p21 in TAMs might sensitize tumors to CD40 agonist treatment.

Materials and methods

Contacts for reagent and resource sharing

Further information and requests for resources and reagents should be directed to and will be fulfilled by the lead contact, David G. DeNardo (ddenardo@wustl.edu).

Murine PDAC models

Mice were maintained in the Laboratory for Animal Care barrier facility at the Washington University School of Medicine. All studies were approved by the Washington University School of Medicine Institutional Animal Studies Committee.

KPC mice (p48-Cre;Kras$^{LSL\text{-}G12D}$;Trp53$^{fl/fl}$) used in these studies have been rapidly bred to the C57Bl/6J background in our laboratory using speed-congenics and further backcrossed more than five times. All mice were housed, bred, and maintained under specific pathogen-free conditions in accordance with NIH-AALAC standards and were consistent with the Washington University School of Medicine IACUC regulations (protocols #20160265 and #19-0856).

The KP-1 cell line was derived from PDAC tissues of the 2.2-month-old p48-CRE^{+}/LSL-Kras^{G12D}/p53$^{flox/flox}$ (KPC); the KP-2 cell line was derived from the 6-month-old p48-CRE^{+}/LSL-Kras^{G12D}/p53$^{flox/+}$ mice(KP$^{fl/+C}$) (Jiang et al., 2016). The KI cell line was derived from the Pdx1-Cre;LSL-Kras^{G12D};Ink/Arf$^{fl/fl}$ as previously described (Mitchem et al., 2013). Cells were grown on collagen-coated tissue culture flasks for < 12 passages, and were tested for cytokeratin-19, smooth muscle actin, vimentin, and CD45 to verify their carcinoma identity and purity. The PDA.69 cell line was a kind gift from Dr. Gregory L. Beatty, and was maintained in tissue culture flasks with DMEM supplemented with 1% glutamax and 0.167% gentamycin for less than 13 passages. To establish orthotopic PDAC models, either 50,000 or 200,000 KP-2 cells, and 10,000 or 50,000 PDA.69 cells in 50 µL of Cultrex (Trevigen, Gaithersburg, MD, USA) were injected into the pancreas of 8–12-week-old C57BL/6 mice or transgenic mice according to published protocols (Kim et al., 2009). Tumor-bearing mice were sacrificed when the palpable tumor size was > 1 cm (21–27days).

Other mouse models

The p21^{CE} mouse was developed at the Washington University Mouse Embryonic Stem Cell Core using the construct of Cdkn1a (p21, accession #NM_007669). Briefly, the construct contained the p21 gene under the control of a CAG promoter and a lox-stop-lox case. Downstream of the p21 gene, the construct also contained an internal ribosome entry site (IRES) and YFP gene for visualization. The construct was then integrated into the ROSA locus of pure C57/B6 mice (ROSA-CAG-LSL-p21-IRES-YFP) and injected into C57 blastocyst (p21$^{+/wt}$). Successful chimeras were selected and verified by DNA sequencing across ROSA junctions (primers are listed in Table S2) and subsequent founder mice were identified via genomic PCR (primers are listed in Table S2). Then, p21$^{+/wt}$ mice were crossed with LysMCre mice to specifically induce p21 expression in macrophages. The resulting LysM$^{+/+}$/p21$^{+/wt}$ mice are termed "p21 constitutive expression" (p21^{CE}) mice.

Tissue harvest

Mice were euthanized by intracardiac perfusion with 15 mL of phosphate-buffered saline (PBS)-heparin under isoflurane anesthesia. Blood was obtained by cardiac puncture and deposited in heparin-PBS (Alfa Aesar Lonza, Haverhill, MA, USA) solution. Blood was then incubated in red blood cell lysis buffer (Biolegend, San Diego, CA, USA) for 10 min on ice and quenched with 1% fetal bovine serum (FBS; Atlanta Biologicals, Flowery Branch, GA, USA) containing PBS. Normal and tumor tissues were manually minced and digested in 20 mL of Hank's Balanced Salt Solution (Thermo Fisher Scientific, Waltham, MA, USA) supplemented with 2 mg/mL of collagenase A (Roche, Basel, Switzerland) and 1× DNase I (Sigma-Aldrich, St. Louis, MO, USA) for 30 min (20 min for normal tissue) at 37°C with agitation. After digestion, the cell suspensions were quenched with 5 mL of PBS and filtered through 40 μm nylon mesh. The filtered suspensions were then pelleted by centrifugation (1,800 rpm for 4 min at 4°C) and resuspended in flow cytometry buffer [PBS containing 1% bovine serum albumin (BSA) and 5 mM EDTA] as a single cell suspension.

Flow cytometry

Following tissue digestion, single cell suspensions were blocked with rat anti-mouse CD16/CD32 antibodies (eBioscience, Waltham, MA, USA) for 10 min on ice, and pelleted by centrifugation. The cells were subsequently labeled with 100 μL of fluorophore-conjugated anti-mouse extracellular antibodies at recommended dilutions for 30 min on ice in flow cytometry buffer. Intracellular staining was conducted using eBioscience Transcription Factor Staining Buffer using the manufacturer's recommended procedures. All antibodies are listed in Table S3. For live analysis of YFP, fluorophore-labeled cells were analyzed immediately without fixation on X-20 cytometers.

For proliferation assays, mice were injected with BrdU, 1 mg i.p. at 3 h prior to sacrifice. A BD Biosciences Cytofix/Cytoperm kit (BD Biosciences, San Jose, CA, USA) was used following extracellular staining to stain for BrdU.

Human samples

Human PDAC samples were obtained from consenting patients diagnosed at Washington University and the Siteman Cancer Center. Patients underwent pancreaticoduodenectomy. The Washington University Ethics committee approved the study under IRB protocol #201704078.

Mass cytometry

Human tumor samples were collected on different days right after surgery and digested in Hank's Balanced Salt Solution supplemented with 2 mg/mL collagenase A (Roche), 2.5 U/mL hyaluronidase (Sigma-Aldrich), and DNase I at 37°C for 30 min with agitation to generate single cell suspensions. Cell suspensions were counted and stained in 5 μM cisplatin per million cells for exactly 3 min on ice and washed with Cy-FACS buffer (PBS, 0.1% BSA, 0.02% NaN_3, and 2 mM EDTA) twice. The cells were then incubated with FcR blocking reagent plus surface-antibody cocktail for 40 min on ice. After incubation, surface marker-stained cells were washed twice with Cy-FACS buffer. Cells were then fixed with 4% paraformaldehyde (PFA) for 10 min on ice and permeabilized with permeabilization buffer containing the intracellular stain cocktail (Invitrogen, Carlsbad, CA, USA) for 40 min. All antibodies are listed in Table S5. The cells were then washed and fixed a second time in 4% PFA in PBS at 4°C at least overnight. One day prior to acquisition, the cells were washed twice and stained with 200 μL of DNA intercalator per million cells. Cells were acquired on a CyTOF2 mass cytometer (South San Francisco, CA, USA) and were normalized with the MATLAB normalizer (v.7.14.0.739 run in MATLAB R2012a) (Finck et al., 2013). The normalized data were uploaded into Cytobank and manually gated to exclude normalization beads, cell debris, dead cells, doublets, and $CD45^-$ cells. The filtered sample from each individual specimen was then exported and batch normalized by the date of acquisition using the R Cydar package NormalizeBatch function (mode = “range”) to compute a quantile function from the pooled distribution of the input expression data (Lun et al., 2017). In brief, batch expression was scaled between the upper and lower bounds of the pooled reference distribution, with zero values fixed at zero. A total of 10,245 events per batch of corrected sample was then visualized using the standard t-SNE algorithm in Cytobank. Populations of interest were manually gated and verified based on lineage marker expressions.

For mouse samples in Fig. 7 F-I, seven mice per group were individually stained for surface and intracellular stains (the antibodies are listed in Table S6), and fixed overnight as described above. Each sample was then barcoded with a unique combination of palladium metal barcodes using the manufacturer’s instructions (Fluidigm). Following bar coding, the cells were pooled together and incubated overnight in 2% PFA containing 40 nM iridium nucleic acid intercalator (Fluidigm). On the day of acquisition, the barcoded samples were washed and suspended in water containing 10% EQ Calibration Beads (Fluidigm) before acquisition on a CyTOF2 mass cytometer (Fluidigm). Sample barcodes were interpreted using a single cell debarcoder tool (Zunder et al., 2015). FCS files were then uploaded to Cytobank and manually gated to exclude normalization beads, cell debris, dead cells, and doublets. Classical T cells were classified as $CD45^+$, $Cisplatin^-$, $Thy1.2^+$, $NK1.1^-$, $TCRgd^-$, and $TCRb^+$. All T cells were exported as new FCS files and analyzed using the R CATALYST package (Nowicka et al., 2017) in R, version 3.8.2 (The R Project for Statistical Computing, Vienna, Austria). In brief, FCS files were down-sampled to equivalent cell counts, before clustering with the R implementation of the Phenograph algorithm (Levine et al., 2015). All markers were used for clustering analysis except markers used for T cell gating (see above). Dimensional reduction and visualization were performed using the UMAP algorithm (McInnes et al., 2020). Finally, differential cluster abundance testing was performed with the R diffcyt package, utilizing a generalized linear mixed model (Weber et al., 2019).

Macrophage depletion

In Fig. 3 F, 8–12-week-old C57BL/6 mice were orthotopically implanted with 200,000 KP-2 cells. When the tumor was palpable, mice were intraperitoneally treated with one dose of 1 mg CSF1 neutralizing antibody (clone 5A1; BioXCell, Lebanon, NH, USA) and sacrificed at 12 and 24 h after treatments.

In Fig. S4, H - J, to deplete tissue resident macrophages, 8–12-weeks-old p21^{CE} and p21^{WT} mice were implanted orthotopically with 50,000 KP-2 cells on day 0, then were treated with three doses of CSF1 neutralizing antibody (1 mg, 0.5 mg, and 0.5 mg on days 3, 10, and 17) and two doses of clodronate-containing liposomes (200 μL each on days 5 and 12). Control mice were treated with the same doses/volumes of IgG (clone HRPN, BioXCell) and PBS liposomes.

In Vitro co-culture and siRNA treatment

All cell lines were maintained in DMEM (Lonza, Basel, Switzerland) supplemented with 10% FBS (Atlanta Biological) and penicillin/streptomycin (Gibco, Gaithersburg, MD, USA). All cell lines tested negative for mycoplasma.

Pancreatic fibroblasts were harvested from the pancreas of healthy 8-week-old C57BL/6 mice, passaged three times on tissue culture plates, and tested negative for mycoplasma. An immortal pancreatic fibroblast cell line was established by passage more than 18 times. Soluble factors in primary pancreatic fibroblasts and immortal pancreatic fibroblasts medium were measured, compared, and found to be similar.

Bone marrow cells were obtained from both femur and tibia of the mouse and differentiated for five days in DMEM supplemented with 10ng of CSF1 (PeproTech, NJ, USA) for five days to generate BMDMs.

A total of 75,000 fibroblasts or 50,000 KP-2 cells or both cell types were co-cultured with 100,000 BMDMs in 6-well cell culture plates (Costar, San Jose, CA, USA). BrdU was added 6 h prior to harvest at each time point. For Transwell assays, 150,000 fibroblasts were cultured in the Transwell assay with 200,000 BMDMs, and BrdU was added 6 h prior to harvest.

Small interfering RNAs (siRNAs) targeting mouse CSF1 and p21 were purchased from Integrated DNA Technologies (Coralville, IA, USA). Sequences are listed in Table S2. The siRNA transfections for primary BMDMs and pancreatic fibroblasts were performed using the Mouse Macrophage Nucleofector™ Kit (Lonza) and Nucleofector™ 2b Device (Lonza) with prewritten program Y-001 for BMDMs and V-013 for fibroblasts, following the manufacturer's instructions. RNA and protein from transfected primary cells were harvest 24 h after the transfections.

Microarray and RT-qPCR analysis

Total RNA was isolated from BMDMs derived from p21^{CE}, p21^{WT},or p21$^{-/-}$, or from siRNA targeting for p21-treated BMDMs using the E.N.Z.A. Total RNA Kit (Omega Chemicals, Cowpens, SC, USA) according to the manufacturer's instructions. Microarrays were performed on p21 knocked-down BMDMs with the treatment of tumor-conditioned medium for 24 h. A differential gene list was generated with detected fold-changes > 1.5, adjusted p < 0.05. The filtered differential gene list was loaded into R and a hypergeometric test was used to compare known catalogs of functional annotations (enricher) with a FDR of p < 0.05. Top differentially-regulated genes are listed in Table S1. RNAs from BMDMs of $p21^{CE}$, $p21^{WT}$,and $p21^{-/-}$ were reversed-transcribed to cDNAs by using the qScript cDNA SuperMix (QuantaBio, Beverly, MA, USA). Quantitative real-time PCR Taqman primer probe sets specific for targets listed in Table S7 (Applied Biosystems, Foster City, CA, USA) were used, and the relative gene expression for each target was determined on a ABI7900HT quantitative PCR machine (Applied Biosystems) using a Taqman Gene Expression Master Mix (Applied Biosystems). The threshold cycle method was used to determine fold-changes of gene expressions normalized to *Gapdh*, *Hprt,* and *Tbp.*

ELISA and the cytokine array

Conditioned media from fibroblasts and tumor cells were harvested after changing the medium to 0.1% FBS for 24 h with > 80% confluency. The cytokine array were conducted by using a Proteome Profiler Mouse XL Cytokine Array kit (R&D Systems, Minneapolis, MN, USA) following the manufacturer's instructions. The membranes from each conditioned medium were placed in an autoradiography film cassette and exposed to X-ray filming for 5–8 min. Positive signals were quantified by ImageJ software (National Institutes of Health, Bethesda, MD, USA). Conditioned media were concentrated using a Pierce Concentrator (Thermo Fisher Scientific) based on the manufacturer's instructions. CSF1 levels were measured by a Mouse M-CSF Matched Antibody Pair Kit (ab218788) following the manufacturer's instructions.

Single cell RNA sequencing

Normal pancreas tissues were taken from three 10-week-old B6 mice, processed to single cell suspension as explained in the tissue harvest section, pooled together, and sorted for live macrophages ($CD45^+CD11b^+F4/80^+CD3^-CD19^-Siglecf^-Ly6G^-Ly6C^-7AAD^-$) by using an Aria II cell sorter (BD Biosciences)

Pancreatic tumors were taken from three 1.5-month-old KPC mice, processed to a single cell suspension, pooled, and sorted for live macrophages and DC-enriched populations ($CD45^+CD3^-CD19^-SiglecF^-Ly6G^-7AAD^-$).

Orthotopic KP-2 tumors were taken from $p21^{CE}$ and $p21^{WT}$ mice, and three from each genotype were pooled as one sample and sorted for live CD45+ cells ($CD45^+7AAD^-$). Two libraries were created for each genotype.

Sorted cells from each sample were encapsulated into droplets and libraries were prepared using Chromium Single Cell 3'v3 Reagent kits according to the manufacturer's protocol (10x Genomics, Pleasanton, CA, USA). The generated libraries were sequenced by a NovaSeq 6000 sequencing system (Illumina, San Diego, CA, USA) to an average of 50,000 mean reads per cell. Cellranger mkfastq pipeline (10X Genomics) was used to demultiplex illumine base call files to FASTQ files. Files from the normal pancreas, pancreatic tumors, and orthotopic tumors were demultiplexed with > 97% valid barcodes, and >

94% q30 reads. YFP sequences were inserted into the mm10 reference (v.3.1.0; 10X Genomics) using the Cellranger Mkref pipeline. Afterwards, fastq files from each sample were processed with Cellranger counts and aligned to the mm10 reference (v.3.1.0, 10X Genomics) or mm10 containing YFP for p21^{CE} orthotopic tumor samples and the generated feature barcode matrix.

Human scRNAseq data were obtained from a publicly available dataset (Peng et al., 2019). FASTQ files were realigned to the human GRCh38 reference and generated feature barcode matrix, including 24 PDAC samples and 11 normal samples. However, only 21 PDAC samples and six normal samples successfully passed the Cellranger count function.

Mouse scRNAseq data (mPDAC GEMM-1) used in Fig. 3 A,B and Fig. 4 L,M and Fig. S2 F were obtained from a published paper (Hosein et al., 2019).

Mouse scRNAseq data analysis

The filtered feature barcode matrix from the normal pancreas, KPC pancreatic tumors, and p21^{WT} orthotopic tumors were loaded into Seurat as Seurat objects (Seurat v.3). For each Seurat object, genes that were expressed in less than three cells and cells that expressed less than 1,000 or more than 8,000 genes, were excluded. Cells with greater than 6% mitochondrial RNA content were also excluded, resulting in 9,821 cells for normal, 6,091 for KPC tumors, and 16,904 for orthotopic tumors. SCTransform with default parameters was used on each individual sample to normalize and scale the expression matrix against the sequence depths and percentages of mitochondrial genes. Cell cycle scores and the corresponding cell cycle phase for each cell were calculated, and assigned after SCTransform based on the expression signatures for S and G2/M genes (CellCycleScoring). The differences between the S phase score and G2/M score were regressed-out by SCTransform on individual samples. Variable features were calculated for each sample independently and ranked, based on the number of samples they were independently identified (SelectIntegrationFeatures). The top 3,000 shared variable features were used for multi-set canonical correlation analysis to reduce dimensions and identify projection vectors that defined shared biological states among samples and maximized overall correlations across datasets. Mutual nearest neighbors (MNNS; pairs of cells, with one from each dataset) were calculated and identified as “anchors” (FindIntegrationAnchors). Multiple datasets were then integrated based on these calculated “anchors” and guided order trees with default parameters (IntegrateData). Principle component analysis (PCA) was performed on the 3,000 variable genes calculated earlier (function RunPCA). A UMAP dimensional reduction was performed on the scaled matrix using the first 25 PCA components to obtain a two-dimensional representation of cell states. Then, these defined 25 dimensionalities were used to refine the edge weights between any two cells based on Jaccard similarity (FindNeighbors), and were used to cluster cells through FindClusters functions, which implemented shared nearest neighbor modularity optimization with a resolution of 0.3, leading to 21 clusters.

To characterize clusters, the FindAllMarkers function with logfold threshold = 0.25 and minimum 0.25-fold difference and MAST test were used to identify signatures alone with each cluster. The macrophage/monocytes (clusters 0, 1, 2, 4, 6, 13, and 17)(Fig. S1 E) were selected and the top 3,000 variable features were recalculated to recluster to a higher resolution of 1. Macrophages were selected based on clusters with high expressions of known macrophage marker genes, including *Csf1r*, *C1qa*, *C1qb*, *and H2-Aa,* and confirmed by the absence of *Cd3e*, *Ms4a1*, *Krt19*, *Zbtb46*, and *Flt3*, and further confirmed by identifying DEGs associated with potential macrophage clusters, when compared to known macrophage specific marker genes. In Fig. 1 J, we reran SCTransform without regressing-out cell cycle scores to visualize proliferating macrophage clusters. In Fig. 4, L and M, monocyte clusters were removed based on expressions of monocyte markers, *Ly6c2*, *Plac8*, and *Vcan*. Macrophages were then stratified based on p21 expression into $p21^{High}$ (top 10%) and $p21^{Low}$ (bottom 10%), resulting in 219 of $p21^{High}$ vs. 182 of $p21^{Low}$ TAMs in KPC tumor, and 475 of $p21^{High}$ vs. 526 of $p21^{Low}$ TAMs in KP-2 orthotopic tumors. For GSEA comparisons, the $\log_2$ (fold-change) of all genes detected with min.pct > 0.1 and past MAST test was used as a ranking metric. GSEA was performed using GO terms, KEGG pathways, Reactome, and MSigDB gene sets with Benjamini-Hochberg FDR < 0.05 in ClusterProfiler (Wu et al., 2021). For DEGs between the two groups in each mouse PDAC model, we filtered genes with a Bonferroni-corrected p-value < 0.05 and fold-change >1.2 or <0.8.

For the mouse dataset (Hosein et al., 2019), the filtered feature barcode matrices, containing KIC, KPC, and KPFC, were processed similarly with major cell types annotated in Fig. 3 B. Macrophages were then selected and stratified based on p21 expressions into $p21^{High}$ (top 10%) and $p21^{Low}$ (bottom 10%), resulting in 263 of $p21^{High}$ TAMs vs. 237 of $p21^{Low}$ TAMs.

For $p21^{CE}$ and $p21^{WT}$ comparisons, the filtered feature barcode matrix was processed similarly, ending with 16,931 cells for $p21^{WT}$ tumors, and 9,519 cells for $p21^{CE}$ tumors. Cell cycle scores and the corresponding cell cycle phase for each cell were calculated and assigned after SCTransform based on the expression signatures for S and G2/M associated genes (CellCycleScoring). The top 3,000 variable genes, 25 dimensionalities, and resolution of 0.3 generated 19 clusters (Fig. S4, A and B) , including 16,093 cells for $p21^{CE}$ tumors and 8,996 cells for $p21^{WT}$ tumors. Each population, including macrophages (clusters 1, 3, 5, 12, 15, and 18), monocytes (cluster 2), DCs (clusters 4, 11, 9, and 16), neutrophils (cluster 14), and eosinophils (cluster 0) were subsetted, at 15 dimensionalities and resolutions of 1 to generate Fig. 6 C and Fig. 7 A and Fig. S4 E. Cell cycle effects were also regressed-out when subsetting on each cell type, except for macrophages. DEGs with minimum percentage > 0.1, a Bonferroni-corrected p-value < 0.05. and fold-change > 1.3 or < 0.75 were considered significant. The $\log_2$ (fold-change) of all genes detected with minimum percentage > 0.1 and past MAST tests were used as a ranking metric for GSEA analysis. Gene sets with FDR < 0.05 were considered significant.

Human scRNAseq data analysis

For the human dataset (Peng et al., 2019), cells with greater than 15% mitochondrial genes were retained and cells that expressed less than 500 genes were excluded. SCTransform with default parameters was used on each individual sample to normalize and scale the expression matrix against sequence depth and percentage of mitochondrial genes. Cell cycle scores and the corresponding cell cycle phase for each cell were calculated, then assigned after SCTransform based on the expression signatures for S and G2/M genes (CellCycleScoring). The differences between S phase scores and G2/M scores were regressed-out by SCTransform on individual samples. Variable features were calculated for every sample in the dataset independently and ranked based on the number of samples they were independently identified (SelectIntegrationFeatures). The top 3,000 shared variable features were used for PCA. The calculated PCA embedding of each cell was then used as an input for the soft k-means clustering algorithm. Briefly, through iteration, the algorithm designated the cluster-specific centroids and cell-specific correction factors corresponding to batch effects. The correction factors were used to assign cells into clusters until the assignment was stable (RunHarmony). Afterwards, similar steps were taken; UMAP reduction used the first 20 PCA components and FindClusters with a resolution of 0.3, leading to 12 clusters (Fig. 3 D). Immune cell clusters (3, 4, 9, and 10) were reclustered, reintegrated (RunHarmony), and UMAP reduction was used with a resolution of 0.5 to generate 11 clusters. The clusters were further grouped into NKT cells, T_{regs}, T cells, Myeloid cells, and B cells in Fig. 1, F and G.

The mpIHC

Mouse tissues were fixed in 10% formalin for 24 h and embedded in paraffin after graded ethanol dehydration. Embedded tissues were sectioned into 6-μm sections and loaded into BOND R_Xm (Leica Biosystems, Wetzlar, Germany) for a series of staining including F4/80, p21, PDPN, Ki67, and CK19. Based on antibody host species, default manufacturer protocols were used (IntenseR and Polymer Refine), containing antigen-retrieval with citrate buffer, goat serum and peroxide block, primary antibody incubation, post-primary incubation, and chromogenically visualized with an AEC substrate (Abcam, Cambridge, UK). Between each two cycles of staining, the slides were manually stained for hemoxylin and eosin, then scanned by Axio Scan.Z1 (Zeiss, Jena, Germany). The slides were then destained by a gradient of ethanol plus a 2% hydrochloride wash and blocked with extra avidin/biotin (Vector Laboratories, Burlingame, CA, USA) and a Fab fragment block (Jackson Laboratory, Bar Harbor, ME, USA).

Images of the same specimen but different stains were cropped into multiple segments by Zen software (Zeiss). Each segment was then deconvoluted (Deconvolution, v.1.0.4; Indica Labs, Albuquerque, NM, USA) for individual staining and fused using HALO software (Zeiss) with the default manufacturer's settings. Markers of interest were pseudo-colored and quantified through the High plex FL, v.4.0.3 algorithm (Indica Labs).

Acknowledgements:

We thank the Washington University Transgenic Vector Center for generating constructs of $p21^{CE}$ mice. We thank the Washington University Center for Cellular Imaging for imaging experiments. We thank The CHiiPs Immunomonitoring Laboratory for CyTOF experiments. We thank the Flow Cytometry & Fluorescence

Activated Cell Sorting Core for sorting and flow cytometry experiments. We thank the Genome Technology Access Center for scRNAseq and microarray experiments.

Online supplemental material:

Fig. S1 examine mpIHC staining and identifies cell types in Human CyTOF and murine scRNAseq analysis. **Fig. S2** supports siRNA knockdown of p21 in BMDMs *in vitro,* and shows p21 expression in TAMs and its connection to cell-cycle states. Representative images used to evaluate mpIHC staining of murine PDAC tissues are included. **Fig. S3** demonstrates flow cytometry and complete blood count analysis of the immune compositions in non-tumor bearing p21^{CE} and p21^{WT} mice, and in tumor bearing p21^{CE} and p21^{WT} mice. **Fig. S4** identifies major clusters in scRNAseq analysis performed on tumor bearing p21^{CE} and p21^{WT} mice. It also provides bar plots for macrophage depletion experiment. **Fig. S5** shows the GSEA results when comparing TAMs from p21^{CE} to p21^{WT}. **Table S1** includes the top 50 differentially expressed genes in p21-deprived BMDMs cultured in tumor conditioned medium. **Table S2** includes all siRNA sequences used in the current paper. **Table S3** includes antibodies used for flow cytometry. **Table S4** includes all antibodies used for mpIHC. **Tables S5** and **S6** include all antibodies used for CyTOF. **Table S7** lists all primers used for qPCR. Table **S8** lists all organisms and strains used. **Table S9** lists all softwares and algorithms. Chemicals and recombinant proteins used could be found in **Table S10**. **Table S11** shows all the commercial assays used.

References:

Abram, C.L., G.L. Roberge, Y. Hu, and C.A. Lowell. 2014. Comparative analysis of the efficiency and specificity of myeloid-Cre deleting strains using ROSA-EYFP reporter mice. *J Immunol Methods*. 408:89–100. doi:10.1016/j.jim.2014.05.009.

Amano, S.U., J.L. Cohen, P. Vangala, M. Tencerova, S.M. Nicoloro, J.C. Yawe, Y. Shen, M.P. Czech, and M. Aouadi. 2014. Local proliferation of macrophages contributes to obesity-associated adipose tissue inflammation. *Cell Metab*. 19:162–171. doi:10.1016/j.cmet.2013.11.017.

Balkwill, F. 2006. TNF-alpha in promotion and progression of cancer. *Cancer Metastasis Rev*. 25:409–416. doi:10.1007/s10555-006-9005-3.

Borgoni, S., A. Iannello, S. Cutrupi, P. Allavena, M. D'Incalci, F. Novelli, and P. Cappello. 2018. Depletion of tumor-associated macrophages switches the epigenetic profile of pancreatic cancer infiltrating T cells and restores their anti-tumor phenotype. *Oncoimmunology*. 7:e1393596. doi:10.1080/2162402X.2017.1393596.

Bottazzi, B., E. Erba, N. Nobili, F. Fazioli, A. Rambaldi, and A. Mantovani. 1990. A paracrine circuit in the regulation of the proliferation of macrophages infiltrating murine sarcomas. *J Immunol*. 144:2409–2412.

Brugarolas, J., K. Moberg, S.D. Boyd, Y. Taya, T. Jacks, and J.A. Lees. 1999. Inhibition of cyclin-dependent kinase 2 by p21 is necessary for retinoblastoma protein-mediated G1 arrest after γ-irradiation. *Proc Natl Acad Sci U S A*. 96:1002–1007.

Candido, J.B., J.P. Morton, P. Bailey, A.D. Campbell, S.A. Karim, T. Jamieson, L. Lapienyte, A. Gopinathan, W. Clark, E.J. McGhee, J. Wang, M. Escorcio-Correia, R. Zollinger, R. Roshani, L.

Drew, L. Rishi, R. Arkell, T.R.J. Evans, C. Nixon, D.I. Jodrell, R.W. Wilkinson, A.V. Biankin, S.T. Barry, F.R. Balkwill, and O.J. Sansom. 2018. CSF1R+ Macrophages Sustain Pancreatic Tumor Growth through T Cell Suppression and Maintenance of Key Gene Programs that Define the Squamous Subtype. *Cell Reports*. 23:1448–1460. doi:10.1016/j.celrep.2018.03.131.

Cannarile, M.A., M. Weisser, W. Jacob, A.-M. Jegg, C.H. Ries, and D. Rüttinger. 2017. Colony-stimulating factor 1 receptor (CSF1R) inhibitors in cancer therapy. *Journal for ImmunoTherapy of Cancer*. 5:53. doi:10.1186/s40425-017-0257-y.

Cassetta, L., and J.W. Pollard. 2018. Targeting macrophages: therapeutic approaches in cancer. *Nature Reviews Drug Discovery*. 17:887–904. doi:10.1038/nrd.2018.169.

Castro-Dopico, T., and M.R. Clatworthy. 2019. IgG and Fcγ Receptors in Intestinal Immunity and Inflammation. *Front Immunol*. 10:805. doi:10.3389/fimmu.2019.00805.

Cazzalini, O., A.I. Scovassi, M. Savio, L.A. Stivala, and E. Prosperi. 2010. Multiple roles of the cell cycle inhibitor p21(CDKN1A) in the DNA damage response. *Mutat Res*. 704:12–20. doi:10.1016/j.mrrev.2010.01.009.

Clausen, B.E., C. Burkhardt, W. Reith, R. Renkawitz, and I. Förster. 1999. Conditional gene targeting in macrophages and granulocytes using LysMcre mice. *Transgenic Res*. 8:265–277. doi:10.1023/a:1008942828960.

Coveler, A.L., D.L. Bajor, A. Masood, E. Yilmaz, A.F. Shields, M.M. Javle, R.K. Paluri, G.M. Vaccaro, M. Zalupski, J.E. Grilley-Olson, H.L. Kindler, M.W. Schmitt, and M. Gutierrez. 2020. Phase I study of SEA-CD40, gemcitabine, nab-paclitaxel, and pembrolizumab in patients with metastatic pancreatic ductal adenocarcinoma (PDAC). *JCO*. 38:TPS4671–TPS4671. doi:10.1200/JCO.2020.38.15_suppl.TPS4671.

Davies, L.C., M. Rosas, P.J. Smith, D.J. Fraser, S.A. Jones, and P.R. Taylor. 2011. A quantifiable proliferative burst of tissue macrophages restores homeostatic macrophage populations after acute inflammation. *European Journal of Immunology*. 41:2155–2164. doi:https://doi.org/10.1002/eji.201141817.

DeNardo, D.G., and B. Ruffell. 2019. Macrophages as regulators of tumor immunity and immunotherapy. *Nat Rev Immunol*. 19:369–382. doi:10.1038/s41577-019-0127-6.

Deng, C., P. Zhang, J.W. Harper, S.J. Elledge, and P. Leder. 1995. Mice lacking p21CIP1/WAF1 undergo normal development, but are defective in G1 checkpoint control. *Cell*. 82:675–684. doi:10.1016/0092-8674(95)90039-x.

Doedens, A.L., C. Stockmann, M.P. Rubinstein, D. Liao, N. Zhang, D.G. DeNardo, L.M. Coussens, M. Karin, A.W. Goldrath, and R.S. Johnson. 2010. Macrophage expression of hypoxia-inducible factor-1 alpha suppresses T-cell function and promotes tumor progression. *Cancer Res*. 70:7465–7475. doi:10.1158/0008-5472.CAN-10-1439.

Dutto, I., M. Tillhon, O. Cazzalini, L.A. Stivala, and E. Prosperi. 2015. Biology of the cell cycle inhibitor p21CDKN1A: molecular mechanisms and relevance in chemical toxicology. *Arch Toxicol*. 89:155–178. doi:10.1007/s00204-014-1430-4.

Elyada, E., M. Bolisetty, P. Laise, W.F. Flynn, E.T. Courtois, R.A. Burkhart, J.A. Teinor, P. Belleau, G. Biffi, M.S. Lucito, S. Sivajothi, T.D. Armstrong, D.D. Engle, K.H. Yu, Y. Hao, C.L. Wolfgang, Y. Park, J. Preall, E.M. Jaffee, A. Califano, P. Robson, and D.A. Tuveson. 2019. Cross-Species Single-Cell Analysis of Pancreatic Ductal Adenocarcinoma Reveals Antigen-Presenting Cancer-Associated Fibroblasts. *Cancer Discov*. 9:1102–1123. doi:10.1158/2159-8290.CD-19-0094.

Finck, R., E.F. Simonds, A. Jager, S. Krishnaswamy, K. Sachs, W. Fantl, D. Pe'er, G.P. Nolan, and S.C. Bendall. 2013. Normalization of mass cytometry data with bead standards. *Cytometry Part A*. 83A:483–494. doi:https://doi.org/10.1002/cyto.a.22271.

Franklin, R.A., W. Liao, A. Sarkar, M.V. Kim, M.R. Bivona, K. Liu, E.G. Pamer, and M.O. Li. 2014. The cellular and molecular origin of tumor-associated macrophages. *Science*. 344:921–925. doi:10.1126/science.1252510.

Gardner, A., and B. Ruffell. 2016. Dendritic Cells and Cancer Immunity. *Trends Immunol*. 37:855–865. doi:10.1016/j.it.2016.09.006.

Ginhoux, F., and M. Guilliams. 2016. Tissue-Resident Macrophage Ontogeny and Homeostasis. *Immunity*. 44:439–449. doi:10.1016/j.immuni.2016.02.024.

Hao, N.-B., M.-H. Lü, Y.-H. Fan, Y.-L. Cao, Z.-R. Zhang, and S.-M. Yang. 2012. Macrophages in Tumor Microenvironments and the Progression of Tumors. *Clinical and Developmental Immunology*. 2012:e948098. doi:https://doi.org/10.1155/2012/948098.

Hashimoto, D., A. Chow, C. Noizat, P. Teo, M.B. Beasley, M. Leboeuf, C.D. Becker, P. See, J. Price, D. Lucas, M. Greter, A. Mortha, S.W. Boyer, E.C. Forsberg, M. Tanaka, N. van Rooijen, A. García-Sastre, E.R. Stanley, F. Ginhoux, P.S. Frenette, and M. Merad. 2013. Tissue-resident macrophages self-maintain locally throughout adult life with minimal contribution from circulating monocytes. *Immunity*. 38:792–804. doi:10.1016/j.immuni.2013.04.004.

Hervas-Stubbs, S., J.L. Perez-Gracia, A. Rouzaut, M.F. Sanmamed, A.L. Bon, and I. Melero. 2011. Direct Effects of Type I Interferons on Cells of the Immune System. *Clin Cancer Res*. 17:2619–2627. doi:10.1158/1078-0432.CCR-10-1114.

Hingorani, S.R., E.F. Petricoin, A. Maitra, V. Rajapakse, C. King, M.A. Jacobetz, S. Ross, T.P. Conrads, T.D. Veenstra, B.A. Hitt, Y. Kawaguchi, D. Johann, L.A. Liotta, H.C. Crawford, M.E. Putt, T. Jacks, C.V.E. Wright, R.H. Hruban, A.M. Lowy, and D.A. Tuveson. 2003. Preinvasive and invasive ductal pancreatic cancer and its early detection in the mouse. *Cancer Cell*. 4:437–450. doi:10.1016/S1535-6108(03)00309-X.

Hingorani, S.R., L. Wang, A.S. Multani, C. Combs, T.B. Deramaudt, R.H. Hruban, A.K. Rustgi, S. Chang, and D.A. Tuveson. 2005. Trp53R172H and KrasG12D cooperate to promote chromosomal instability and widely metastatic pancreatic ductal adenocarcinoma in mice. *Cancer Cell*. 7:469–483. doi:10.1016/j.ccr.2005.04.023.

Hosein, A.N., H. Huang, Z. Wang, K. Parmar, W. Du, J. Huang, A. Maitra, E. Olson, U. Verma, and R.A. Brekken. 2019. Cellular heterogeneity during mouse pancreatic ductal adenocarcinoma progression at single-cell resolution. *JCI Insight*. 4. doi:10.1172/jci.insight.129212.

Hsu, C.-H., S.J. Altschuler, and L.F. Wu. 2019. Patterns of Early p21 Dynamics Determine Proliferation-Senescence Cell Fate after Chemotherapy. *Cell*. 178:361-373.e12. doi:10.1016/j.cell.2019.05.041.

Ino, Y., R. Yamazaki-Itoh, K. Shimada, M. Iwasaki, T. Kosuge, Y. Kanai, and N. Hiraoka. 2013. Immune cell infiltration as an indicator of the immune microenvironment of pancreatic cancer. *Br J Cancer*. 108:914–923. doi:10.1038/bjc.2013.32.

Jenkins, S.J., D. Ruckerl, P.C. Cook, L.H. Jones, F.D. Finkelman, N. van Rooijen, A.S. MacDonald, and J.E. Allen. 2011. Local macrophage proliferation, rather than recruitment from the blood, is a signature of TH2 inflammation. *Science*. 332:1284–1288. doi:10.1126/science.1204351.

Jenkins, S.J., D. Ruckerl, G.D. Thomas, J.P. Hewitson, S. Duncan, F. Brombacher, R.M. Maizels, D.A. Hume, and J.E. Allen. 2013. IL-4 directly signals tissue-resident macrophages to proliferate beyond homeostatic levels controlled by CSF-1. *J Exp Med*. 210:2477–2491. doi:10.1084/jem.20121999.

Jiang, H., S. Hegde, B.L. Knolhoff, Y. Zhu, J.M. Herndon, M.A. Meyer, T.M. Nywening, W.G. Hawkins, I.M. Shapiro, D.T. Weaver, J.A. Pachter, A. Wang-Gillam, and D.G. DeNardo. 2016. Targeting focal adhesion kinase renders pancreatic cancers responsive to checkpoint immunotherapy. *Nat Med*. 22:851–860. doi:10.1038/nm.4123.

Kaplan, D.H. 2017. Ontogeny and function of murine epidermal Langerhans cells. *Nature Immunology*. 18:1068–1075. doi:10.1038/ni.3815.

Kim, M.P., D.B. Evans, H. Wang, J.L. Abbruzzese, J.B. Fleming, and G.E. Gallick. 2009. Generation of orthotopic and heterotopic human pancreatic cancer xenografts in immunodeficient mice. *Nat Protoc*. 4:1670–1680. doi:10.1038/nprot.2009.171.

Kitajima, S., R. Thummalapalli, and D.A. Barbie. 2016. Inflammation as a Driver and Vulnerability of KRAS Mediated Oncogenesis. *Semin Cell Dev Biol*. 58:127–135. doi:10.1016/j.semcdb.2016.06.009.

Korsunsky, I., N. Millard, J. Fan, K. Slowikowski, F. Zhang, K. Wei, Y. Baglaenko, M. Brenner, P. Loh, and S. Raychaudhuri. 2019. Fast, sensitive and accurate integration of single-cell data with Harmony. *Nat Methods*. 16:1289–1296. doi:10.1038/s41592-019-0619-0.

Koucký, V., J. Bouček, and A. Fialová. 2019. Immunology of Plasmacytoid Dendritic Cells in Solid Tumors: A Brief Review. *Cancers (Basel)*. 11:470. doi:10.3390/cancers11040470.

Lee, A.W., S. Nambirajan, and J.G. Moffat. 1999. CSF-1 activates MAPK-dependent and p53-independent pathways to induce growth arrest of hormone-dependent human breast cancer cells. *Oncogene*. 18:7477–7494. doi:10.1038/sj.onc.1203123.

Lee, J.W., C.A. Komar, F. Bengsch, K. Graham, and G.L. Beatty. 2016. Genetically Engineered Mouse Models of Pancreatic Cancer: The KPC Model (LSL-Kras(G12D/+) ;LSL-Trp53(R172H/+) ;Pdx-1-Cre), Its Variants, and Their Application in Immuno-oncology Drug Discovery. *Curr Protoc Pharmacol*. 73:14.39.1-14.39.20. doi:10.1002/cpph.2.

Levine, J.H., E.F. Simonds, S.C. Bendall, K.L. Davis, E.D. Amir, M.D. Tadmor, O. Litvin, H.G. Fienberg, A. Jager, E.R. Zunder, R. Finck, A.L. Gedman, I. Radtke, J.R. Downing, D. Pe'er, and G.P. Nolan. 2015. Data-Driven Phenotypic Dissection of AML Reveals Progenitor-like Cells that Correlate with Prognosis. *Cell*. 162:184–197. doi:10.1016/j.cell.2015.05.047.

Lin, K.-Y., D. Lu, C.-F. Hung, S. Peng, L. Huang, C. Jie, F. Murillo, J. Rowley, Y.-C. Tsai, L. He, D.-J. Kim, E. Jaffee, D. Pardoll, and T.-C. Wu. 2007. Ectopic expression of vascular cell adhesion molecule-1 as a new mechanism for tumor immune evasion. *Cancer Res*. 67:1832–1841. doi:10.1158/0008-5472.CAN-06-3014.

Liu, L., Y. Lu, J. Martinez, Y. Bi, G. Lian, T. Wang, S. Milasta, J. Wang, M. Yang, G. Liu, D.R. Green, and R. Wang. 2016. Proinflammatory signal suppresses proliferation and shifts macrophage metabolism from Myc-dependent to HIF1α-dependent. *PNAS*. 113:1564–1569. doi:10.1073/pnas.1518000113.

Lun, A.T.L., A.C. Richard, and J.C. Marioni. 2017. Testing for differential abundance in mass cytometry data. *Nat Methods*. 14:707–709. doi:10.1038/nmeth.4295.

Marchant, A., C. Bruyns, P. Vandenabeele, M. Ducarme, C. Gérard, A. Delvaux, D. De Groote, D. Abramowicz, T. Velu, and M. Goldman. 1994. Interleukin-10 controls interferon-gamma and tumor necrosis factor production during experimental endotoxemia. *Eur J Immunol*. 24:1167–1171. doi:10.1002/eji.1830240524.

Martin, C., D. Ohayon, M. Alkan, J. Mocek, M. Pederzoli-Ribeil, C. Candalh, G. Thevenot, A. Millet, N. Tamassia, M.A. Cassatella, N. Thieblemont, P.-R. Burgel, and V. Witko-Sarsat. 2016. Neutrophil-Expressed p21/waf1 Favors Inflammation Resolution in Pseudomonas aeruginosa Infection. *Am J Respir Cell Mol Biol*. 54:740–750. doi:10.1165/rcmb.2015-0047OC.

Matsushime, H., M.F. Roussel, R.A. Ashmun, and C.J. Sherr. 1991. Colony-stimulating factor 1 regulates novel cyclins during the G1 phase of the cell cycle. *Cell*. 65:701–713. doi:10.1016/0092-8674(91)90101-4.

Mavers, M., C.M. Cuda, A.V. Misharin, A.K. Gierut, H. Agrawal, E. Weber, D.V. Novack, G.K. Haines, D. Balomenos, and H. Perlman. 2012. Cyclin-dependent kinase inhibitor p21, via its C-terminal domain, is essential for resolution of murine inflammatory arthritis. *Arthritis Rheum*. 64:141–152. doi:10.1002/art.33311.

McInnes, L., J. Healy, and J. Melville. 2020. UMAP: Uniform Manifold Approximation and Projection for Dimension Reduction. *arXiv:1802.03426 [cs, stat]*.

Merad, M., P. Sathe, J. Helft, J. Miller, and A. Mortha. 2013. The Dendritic Cell Lineage: Ontogeny and Function of Dendritic Cells and Their Subsets in the Steady State and the Inflamed Setting. *Annu Rev Immunol*. 31. doi:10.1146/annurev-immunol-020711-074950.

Mitchem, J.B., D.J. Brennan, B.L. Knolhoff, B.A. Belt, Y. Zhu, D.E. Sanford, L. Belaygorod, D. Carpenter, L. Collins, D. Piwnica-Worms, S. Hewitt, G.M. Udupi, W.M. Gallagher, C. Wegner, B.L. West, A. Wang-Gillam, S.P. Goedegebuure, D.C. Linehan, and D.G. DeNardo. 2013. Targeting tumor-infiltrating macrophages decreases tumor-initiating cells, relieves immunosuppression and improves chemotherapeutic responses. *Cancer Res*. 73:1128–1141. doi:10.1158/0008-5472.CAN-12-2731.

Müller, E., P.F. Christopoulos, S. Halder, A. Lunde, K. Beraki, M. Speth, I. Øynebråten, and A. Corthay. 2017. Toll-Like Receptor Ligands and Interferon-γ Synergize for Induction of Antitumor M1 Macrophages. *Front. Immunol.* 8. doi:10.3389/fimmu.2017.01383.

Nowicka, M., C. Krieg, H.L. Crowell, L.M. Weber, F.J. Hartmann, S. Guglietta, B. Becher, M.P. Levesque, and M.D. Robinson. 2017. CyTOF workflow: differential discovery in high-throughput high-dimensional cytometry datasets. *F1000Res*. 6:748. doi:10.12688/f1000research.11622.3.

Noy, R., and J.W. Pollard. 2014. Tumor-associated macrophages: from mechanisms to therapy. *Immunity*. 41:49–61. doi:10.1016/j.immuni.2014.06.010.

Peng, J., B.-F. Sun, C.-Y. Chen, J.-Y. Zhou, Y.-S. Chen, H. Chen, L. Liu, D. Huang, J. Jiang, G.-S. Cui, Y. Yang, W. Wang, D. Guo, M. Dai, J. Guo, T. Zhang, Q. Liao, Y. Liu, Y.-L. Zhao, D.-L. Han, Y. Zhao, Y.-G. Yang, and W. Wu. 2019. Single-cell RNA-seq highlights intra-tumoral heterogeneity and malignant progression in pancreatic ductal adenocarcinoma. *Cell Res*. 29:725–738. doi:10.1038/s41422-019-0195-y.

Poh, A.R., and M. Ernst. 2018. Targeting Macrophages in Cancer: From Bench to Bedside. *Front. Oncol.* 0. doi:10.3389/fonc.2018.00049.

Rackov, G., E. Hernández-Jiménez, R. Shokri, L. Carmona-Rodríguez, S. Mañes, M. Álvarez-Mon, E. López-Collazo, C. Martínez-A, and D. Balomenos. p21 mediates macrophage reprogramming through regulation of p50-p50 NF-κB and IFN-β. *J Clin Invest*. 126:3089–3103. doi:10.1172/JCI83404.

Ruffell, B., and L.M. Coussens. 2015. Macrophages and Therapeutic Resistance in Cancer. *Cancer Cell*. 27:462–472. doi:10.1016/j.ccell.2015.02.015.

Salomon, B.L., M. Leclerc, J. Tosello, E. Ronin, E. Piaggio, and J.L. Cohen. 2018. Tumor Necrosis Factor α and Regulatory T Cells in Oncoimmunology. *Front Immunol*. 9. doi:10.3389/fimmu.2018.00444.

Samain, R., A. Brunel, T. Douché, M. Fanjul, S. Cassant-Sourdy, J. Rochotte, J. Cros, C. Neuzillet, J. Raffenne, C. Duluc, A. Perraud, J. Nigri, V. Gigoux, I. Bieche, M. Ponzo, G. Carpentier, I. Cascone, R. Tomasini, H.A. Schmid, M. Mathonnet, R. Nicolle, M.-P. Bousquet, Y. Martineau, S. Pyronnet, C. Jean, and C. Bousquet. 2021. Pharmacologic Normalization of Pancreatic Cancer-Associated Fibroblast Secretome Impairs Prometastatic Cross-Talk With Macrophages. *Cellular and Molecular Gastroenterology and Hepatology*. 11:1405–1436. doi:10.1016/j.jcmgh.2021.01.008.

Scatizzi, J.C., J. Hutcheson, E. Bickel, J.M. Woods, K. Klosowska, T.L. Moore, G.K. Haines, and H. Perlman. 2006. p21Cip1 Is Required for the Development of Monocytes and Their Response to Serum Transfer-induced Arthritis. *The American Journal of Pathology*. 168:1531–1541. doi:10.2353/ajpath.2006.050555.

Schnittert, J., R. Bansal, and J. Prakash. 2019. Targeting Pancreatic Stellate Cells in Cancer. *Trends Cancer*. 5:128–142. doi:10.1016/j.trecan.2019.01.001.

Seleznik, G.M., T. Reding, L. Peter, A. Gupta, S.G. Steiner, S. Sonda, C.S. Verbeke, E. Dejardin, I. Khatkov, S. Segerer, M. Heikenwalder, and R. Graf. 2018. Development of autoimmune pancreatitis is independent of CDKN1A/p21-mediated pancreatic inflammation. *Gut*. 67:1663–1673. doi:10.1136/gutjnl-2016-313458.

Sewing, A., B. Wiseman, A.C. Lloyd, and H. Land. 1997. High-intensity Raf signal causes cell cycle arrest mediated by p21Cip1. *Mol Cell Biol*. 17:5588–5597. doi:10.1128/MCB.17.9.5588.

Stuart, T., A. Butler, P. Hoffman, C. Hafemeister, E. Papalexi, W.M. Mauck, Y. Hao, M. Stoeckius, P. Smibert, and R. Satija. 2019. Comprehensive Integration of Single-Cell Data. *Cell*. 177:1888-1902.e21. doi:10.1016/j.cell.2019.05.031.

Tang, J., M.E. Lobatto, L. Hassing, S. van der Staay, S.M. van Rijs, C. Calcagno, M.S. Braza, S. Baxter, F. Fay, B.L. Sanchez-Gaytan, R. Duivenvoorden, H.B. Sager, Y.M. Astudillo, W. Leong, S. Ramachandran, G. Storm, C. Pérez-Medina, T. Reiner, D.P. Cormode, G.J. Strijkers, E.S.G. Stroes, F.K. Swirski, M. Nahrendorf, E.A. Fisher, Z.A. Fayad, and W.J.M. Mulder. 2015. Inhibiting macrophage proliferation suppresses atherosclerotic plaque inflammation. *Science Advances*. 1:e1400223. doi:10.1126/sciadv.1400223.

Tirosh, I., B. Izar, S.M. Prakadan, M.H. Wadsworth, D. Treacy, J.J. Trombetta, A. Rotem, C. Rodman, C. Lian, G. Murphy, M. Fallahi-Sichani, K. Dutton-Regester, J.-R. Lin, O. Cohen, P. Shah, D. Lu, A.S. Genshaft, T.K. Hughes, C.G.K. Ziegler, S.W. Kazer, A. Gaillard, K.E. Kolb, A.-C. Villani, C.M. Johannessen, A.Y. Andreev, E.M. Van Allen, M. Bertagnolli, P.K. Sorger, R.J. Sullivan, K.T. Flaherty, D.T. Frederick, J. Jané-Valbuena, C.H. Yoon, O. Rozenblatt-Rosen, A.K. Shalek, A. Regev, and L.A. Garraway. 2016. Dissecting the multicellular ecosystem of metastatic melanoma by single-cell RNA-seq. *Science*. 352:189–196. doi:10.1126/science.aad0501.

Trakala, M., C.F. Arias, M.I. García, M.C. Moreno-Ortiz, K. Tsilingiri, P.J. Fernández, M. Mellado, M.T. Díaz-Meco, J. Moscat, M. Serrano, C. Martínez-A, and D. Balomenos. 2009. Regulation of macrophage activation and septic shock susceptibility via p21(WAF1/CIP1). *European Journal of Immunology*. 39:810–819. doi:https://doi.org/10.1002/eji.200838676.

Tymoszuk, P., H. Evens, V. Marzola, K. Wachowicz, M.-H. Wasmer, S. Datta, E. Müller-Holzner, H. Fiegl, G. Böck, N. van Rooijen, I. Theurl, and W. Doppler. 2014. In situ proliferation contributes to accumulation of tumor-associated macrophages in spontaneous mammary tumors. *European Journal of Immunology*. 44:2247–2262. doi:https://doi.org/10.1002/eji.201344304.

Van Gassen, N., E. Van Overmeire, G. Leuckx, Y. Heremans, S. De Groef, Y. Cai, Y. Elkrim, C. Gysemans, B. Stijlemans, M. Van de Casteele, P. De Baetselier, N. De Leu, H. Heimberg, and J.A. Van Ginderachter. 2015. Macrophage dynamics are regulated by local macrophage proliferation and monocyte recruitment in injured pancreas. *Eur J Immunol*. 45:1482–1493. doi:10.1002/eji.201445013.

Waghray, M., M. Yalamanchili, M.P. di Magliano, and D.M. Simeone. 2013. Deciphering the role of stroma in pancreatic cancer. *Curr Opin Gastroenterol*. 29:537–543. doi:10.1097/MOG.0b013e328363affe.

Weber, L.M., M. Nowicka, C. Soneson, and M.D. Robinson. 2019. diffcyt: Differential discovery in high-dimensional cytometry via high-resolution clustering. *Commun Biol*. 2:1–11. doi:10.1038/s42003-019-0415-5.

Wu, T., E. Hu, S. Xu, M. Chen, P. Guo, Z. Dai, T. Feng, L. Zhou, W. Tang, L. Zhan, X. Fu, S. Liu, X. Bo, and G. Yu. 2021. clusterProfiler 4.0: A universal enrichment tool for interpreting omics data. *The Innovation*. 100141. doi:10.1016/j.xinn.2021.100141.

Xaus, J., M. Comalada, A.F. Valledor, J. Lloberas, F. López-Soriano, J.M. Argilés, C. Bogdan, and A. Celada. 2000. LPS induces apoptosis in macrophages mostly through the autocrine production of TNF-α. *Blood*. 95:3823–3831. doi:10.1182/blood.V95.12.3823.

Xiang, X., J. Wang, D. Lu, and X. Xu. 2021. Targeting tumor-associated macrophages to synergize tumor immunotherapy. *Sig Transduct Target Ther*. 6:1–12. doi:10.1038/s41392-021-00484-9.

Yang, H.W., M. Chung, T. Kudo, and T. Meyer. 2017. Competing memories of mitogen and p53 signalling control cell-cycle entry. *Nature*. 549:404–408. doi:10.1038/nature23880.

Yao, H., S.-R. Yang, I. Edirisinghe, S. Rajendrasozhan, S. Caito, D. Adenuga, M.A. O'Reilly, and I. Rahman. 2008. Disruption of p21 attenuates lung inflammation induced by cigarette smoke, LPS, and fMLP in mice. *Am J Respir Cell Mol Biol*. 39:7–18. doi:10.1165/rcmb.2007-0342OC.

Zheng, W., and R.A. Flavell. 1997. The Transcription Factor GATA-3 Is Necessary and Sufficient for Th2 Cytokine Gene Expression in CD4 T Cells. *Cell*. 89:587–596. doi:10.1016/S0092-8674(00)80240-8.

Zhu, Y., J.M. Herndon, D.K. Sojka, K.-W. Kim, B.L. Knolhoff, C. Zuo, D.R. Cullinan, J. Luo, A.R. Bearden, K.J. Lavine, W.M. Yokoyama, W.G. Hawkins, R.C. Fields, G.J. Randolph, and D.G. DeNardo. 2017. Tissue-Resident Macrophages in Pancreatic Ductal Adenocarcinoma Originate from Embryonic Hematopoiesis and Promote Tumor Progression. *Immunity*. 47:323-338.e6. doi:10.1016/j.immuni.2017.07.014.

Zhu, Y., B.L. Knolhoff, M.A. Meyer, T.M. Nywening, B.L. West, J. Luo, A. Wang-Gillam, S.P. Goedegebuure, D.C. Linehan, and D.G. DeNardo. 2014. CSF1/CSF1R Blockade Reprograms Tumor-Infiltrating Macrophages and Improves Response to T-cell Checkpoint Immunotherapy in Pancreatic Cancer Models. *Cancer Res*. 74:5057–5069. doi:10.1158/0008-5472.CAN-13-3723.

Zunder, E.R., R. Finck, G.K. Behbehani, E.D. Amir, S. Krishnaswamy, V.D. Gonzalez, C.G. Lorang, Z. Bjornson, M.H. Spitzer, B. Bodenmiller, W.J. Fantl, D. Pe’er, and G.P. Nolan. 2015. Palladium-based mass tag cell barcoding with a doublet-filtering scheme and single-cell deconvolution algorithm. *Nature Protocols*. 10:316–333. doi:10.1038/nprot.2015.020.

Fig.1

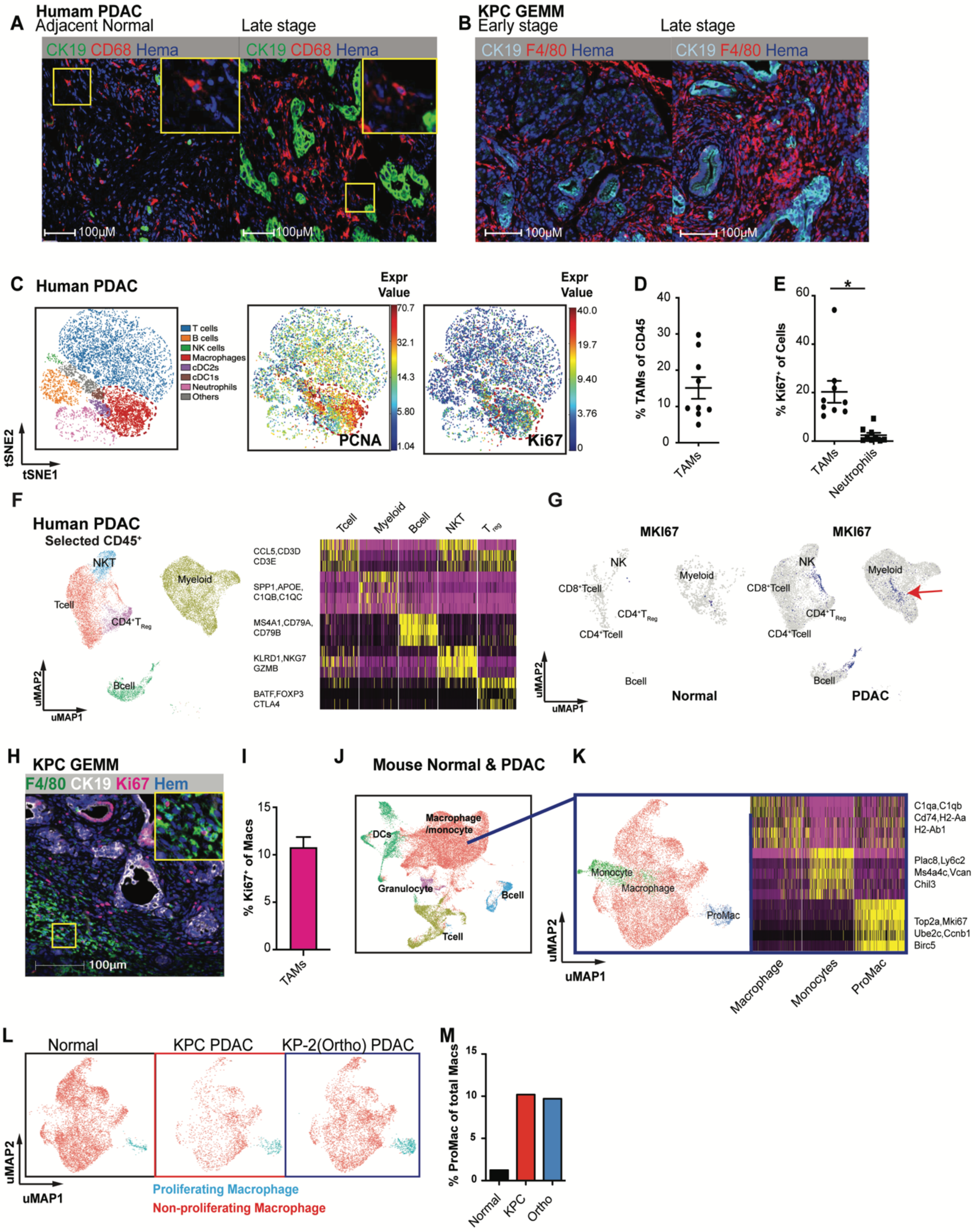
A
Humam PDAC
Adjacent Normal
Late stage
CK19 CD68 Hema
CK19 CD68 Hema
100μM
100μM
B
KPC GEMM
Early stage
Late stage
CK19 F4/80 Hema
CK19 F4/80 Hema
100μM
100μM
C
Human PDAC
T cells
B cells
NK cells
Macrophages
cDC2s
cDC1s
Neutrophils
Others
tSNE2
tSNE1
Expr Value
70.7
32.1
14.3
5.80
1.04
PCNA
Expr Value
40.0
19.7
9.40
3.76
0
Ki67
D
% TAMs of CD45
40
30
20
10
0
TAMs
E
% Ki67+ of Cells
60
40
20
0
*
TAMs
Neutrophils
F
Human PDAC
Selected CD45+
NKT
Tcell
CD4+TReg
Myeloid
Bcell
uMAP2
uMAP1
Tcell
Myeloid
Bcell
NKT
TReg
CCL5,CD3D CD3E
SPP1,APOE, C1QB,C1QC
MS4A1,CD79A, CD79B
KLRD1,NKG7 GZMB
BATF,FOXP3 CTLA4
G
MKI67
MKI67
NK
CD8+Tcell
CD4+TReg
CD4+Tcell
Myeloid
Bcell
Normal
NK
CD8+Tcell
CD4+TReg
CD4+Tcell
Myeloid
Bcell
PDAC
uMAP2
uMAP1
H
KPC GEMM
F4/80 CK19 Ki67 Hem
100μm
I
% Ki67+ of Macs
15
10
5
0
TAMs
J
Mouse Normal & PDAC
DCs
Macrophage /monocyte
Granulocyte
Bcell
Tcell
K
Monocyte
Macrophage
ProMac
uMAP2
uMAP1
C1qa,C1qb Cd74,H2-Aa H2-Ab1
Plac8,Ly6c2 Ms4a4c,Vcan Chil3
Top2a,Mki67 Ube2c,Ccnb1 Birc5
Macrophage
Monocytes
ProMac
L
Normal
KPC PDAC
KP-2(Ortho) PDAC
uMAP2
uMAP1
Proliferating Macrophage
Non-proliferating Macrophage
M
% ProMac of total Macs
15
10
5
0
Normal
KPC
Ortho

Figure 1.

Pancreatic ductal adenocarcinoma (PDAC)-infiltrating macrophages are highly proliferative. (A) Representative immunohistochemistry (IHC) analyses of CD68$^+$ macrophages and CK19$^+$ tumor cells in the late stage of PDAC tissues and adjacent normal tissues from human patients. (**B)** Representative IHC analyses of F4/80$^+$ macrophage and CK19$^+$ tumor cells in early and late stages of KPC genetically engineered mouse models (GEMMs). **(C)** Representative tSNE plots of total normalized CD45$^+$ cells from a PDAC patient, annotated with manually assigned cell identity. The macrophage cluster was marked with a red circle, and expressions of PCNA and Ki67 were explicitly displayed. **(D,E)** Dot plot displaying quantification of tumor-associated macrophages (TAMs), Ki67$^+$ TAMs, and Ki67$^+$ neutrophils across nine human PDAC patients. **(F)** UMAP of realigned and reprocessed publicly available human pancreatic ductal adenocarcinoma (PDAC) dataset (Peng et al., 2019) displaying major CD45$^+$ clusters with expression levels of MKi67 and a heat map showing key gene expressions for each cluster. n = 21 PDAC samples, n = 6 normal samples. **(G)** UMAP plots displaying normalized expression levels of MKI67 across subpopulations with red arrow pointing to MKI67 expressing myeloid cells. **(H,I)** Representative multiplex immunohistochemistry (mpIHC) displaying F4/80$^+$ macrophages, CK19$^+$ tumor cells, and Ki67$^+$ proliferating cells in tumors from p48$^-$Cre$^+$/LSL-Kras^{G12D}/p53$^{flox/flox}$ (KPC) GEMMs with quantification of Ki67$^+$ macrophages; n = 6 mice. **(J)** UMAP dimensionality reduction plot of integrated sorted CD45$^+$ cells from the murine normal pancreas and pancreatic tissues from KPC PDACs and KP-2 orthotopic PDACs with cell type annotations and cell cycle regression. **(K)** UMAP plot of reclustered macrophages/monocytes in **J** without cell cycle regression with a heat map displaying corresponding gene signatures. **(L)** UMAP displaying proliferating macrophages and non-proliferating macrophage clusters across the mouse scRNAseq data set used in **J** with quantification in **(M)**. Data are presented as the mean ± SEM. n.s., not significant; *$p < 0.05$. For comparisons between any two groups, Student's two-tailed *t*-test was used.

Fig.2

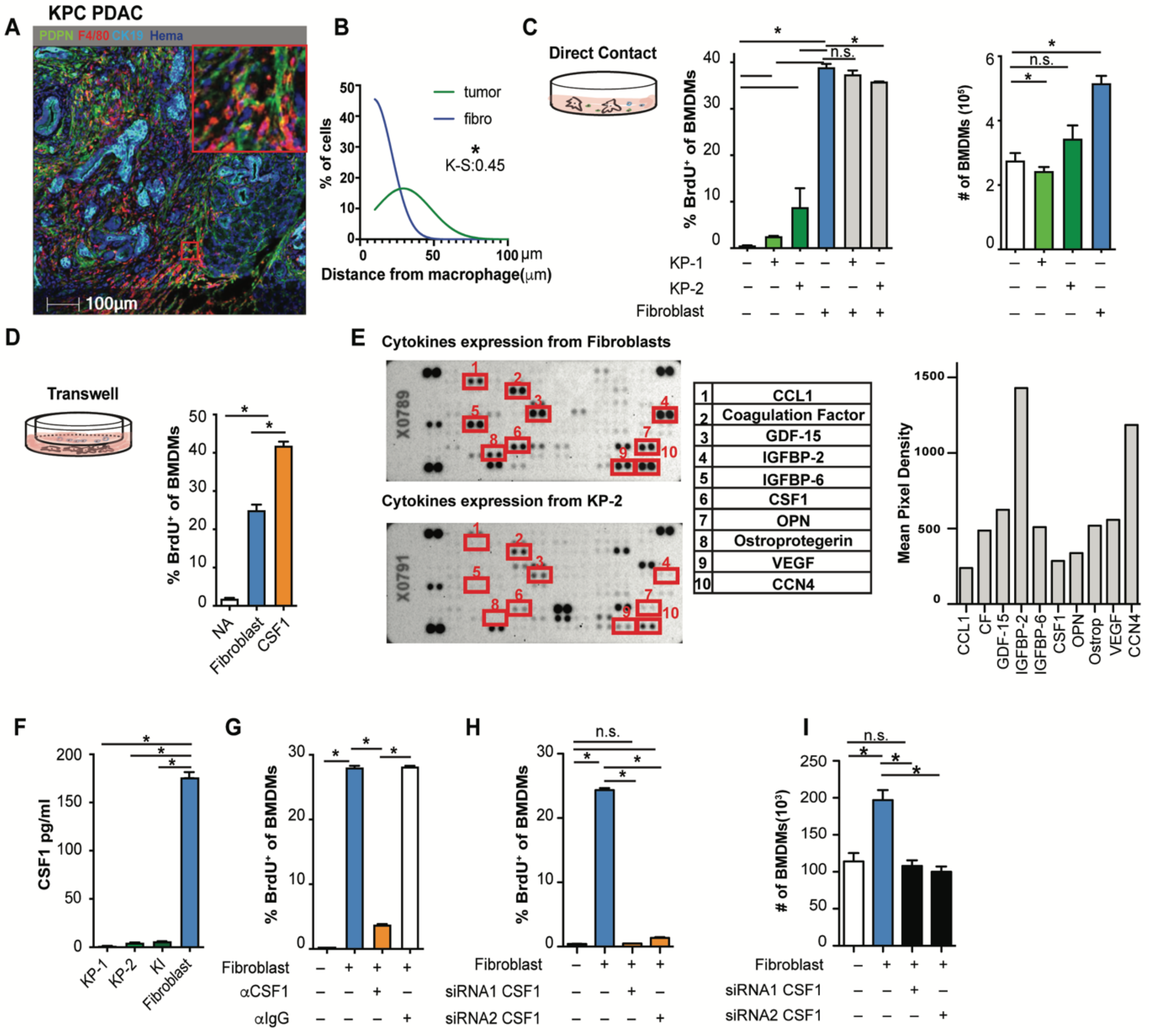

1	CCL1
2	Coagulation Factor
3	GDF-15
4	IGFBP-2
5	IGFBP-6
6	CSF1
7	OPN
8	Ostroprotegerin
9	VEGF
10	CCN4

Figure 2.

Fibroblasts drive macrophage proliferation through colony stimulating factor-1 (CSF1). (A) Representative multiplex immunohistochemistry (mpIHC) image of p48^{-}Cre^{+}/LSL-Kras^{G12D}/p53$^{flox/flox}$ (KPC) mouse pancreatic ductal adenocarcinomas (PDACs) displaying alpha smooth muscle actin (αSMA^{+}) (white) fibroblasts, CK19^{+} (teal) tumor cells, and F4/80^{+} (green) macrophages. **(B)** Frequency distribution of Pdpn^{+} fibroblasts (blue curve) and CK19+ tumor cells (green curve) to a nearest F4/80^{+} macrophage. n = 6 KPC mice. **(C)** The 5-bromo-2'-deoxyuridine (BrdU) incorporation and number of bone marrow-derived macrophages (BMDMs) in co-culture with KP-1, KP-2, fibroblasts, or the combination for 48 h, BrdU pulsed for the last 6 h; n = 6. **(D)** The BrdU incorporation of BMDMs when cultured with fibroblasts in a Transwell assay or 10 ng/mL of CSF1 for 48 h, and BrdU pulsed for the last 6 h; n=3. **(E)** Representative image of a cytokine antibody array resulting from fibroblast- and KP-2-conditioned media, highlighting the top 10 highly expressed cytokines in fibroblast-conditioned medium and the corresponding mean pixel densities. The arrays were repeated two times. **(F)** Bar graph shows the concentrations of CSF1 from three tumor-conditioned media (KP-1, KP-2, and KI) and fibroblast-conditioned medium measured by an ELISA. **(G)** BrdU incorporation of BMDMs in co-culture with fibroblasts treated with 2 µg of αCSF1 or 2 µg of αIgG for 24 h, and BrdU pulsed for the last 6 h; n=3. **(H,I)** BrdU incorporation and number of BMDMs in Transwell cultures with fibroblasts with or without siRNA knockdown for CSF1; n=3. Data are presented as the mean ± SEM. n.s., not significant; *p<0.05. All *in vitro* assays were consistent across at least two independent repeats. For comparisons between any two groups, Student's two-tailed *t*-test was used. Frequency distributions were compared using the nonparametric Kolmogorov-Smirnov test.

Fig.3

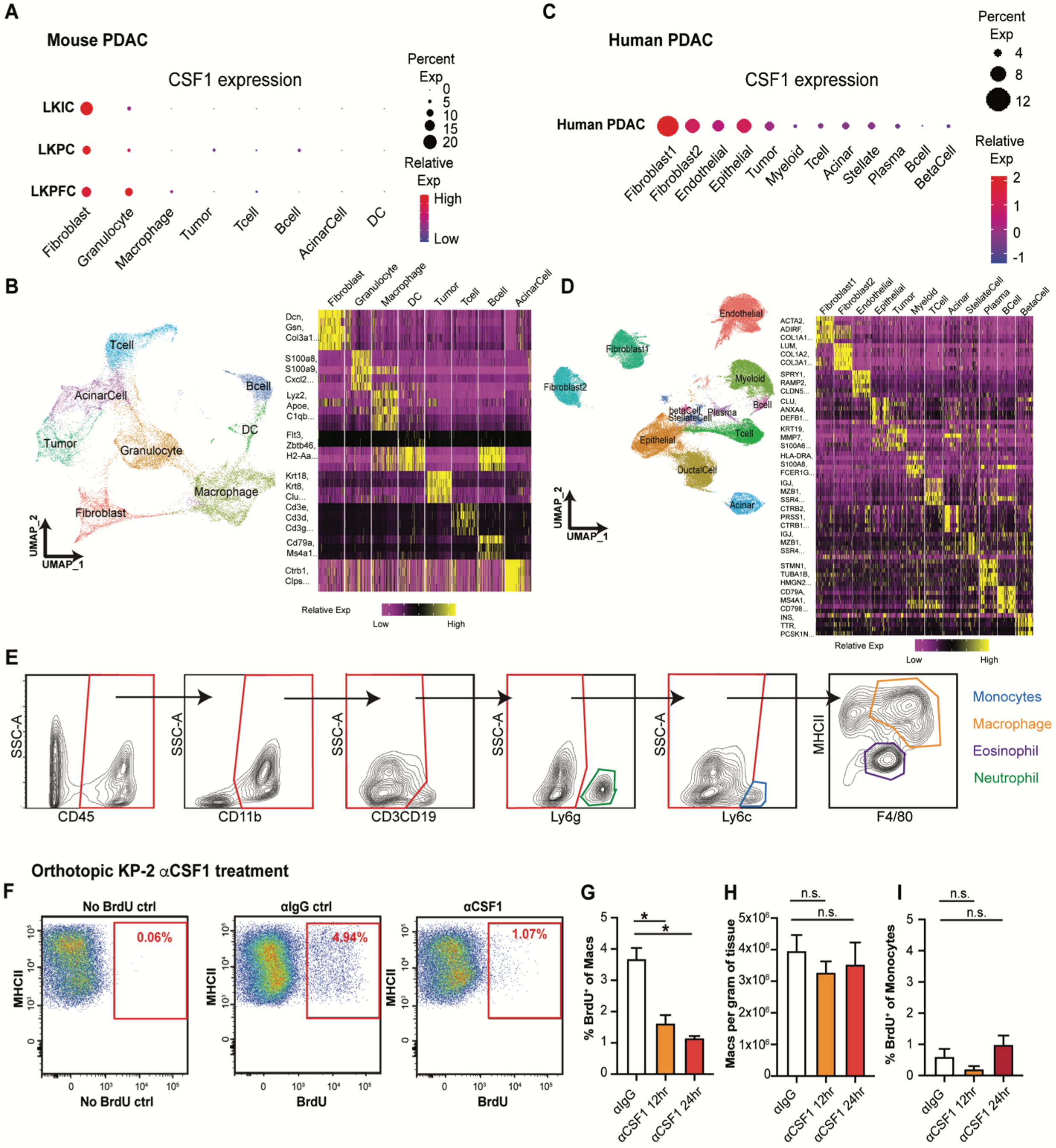
A
Mouse PDAC
CSF1 expression
LKIC
LKPC
LKPFC
Fibroblast
Granulocyte
Macrophage
Tumor
Tcell
Bcell
AcinarCell
DC
Percent Exp
0
5
10
15
20
Relative Exp
High
Low
C
Human PDAC
CSF1 expression
Human PDAC
Fibroblast1
Fibroblast2
Endothelial
Epithelial
Tumor
Myeloid
Tcell
Acinar
Stellate
Plasma
Bcell
BetaCell
Percent Exp
4
8
12
Relative Exp
2
1
0
-1
B
Tcell
AcinarCell
Bcell
DC
Tumor
Granulocyte
Macrophage
Fibroblast
UMAP_2
UMAP_1
Dcn, Gsn, Col3a1...
S100a8, S100a9, Cxcl2...
Lyz2, Apoe, C1qb...
Flt3, Zbtb46, H2-Aa...
Krt18, Krt8, Clu...
Cd3e, Cd3d, Cd3g...
Cd79a, Ms4a1...
Ctrb1, Clps...
Relative Exp
Low
High
D
Endothelial
Fibroblast1
Fibroblast2
Myeloid
betaCell
StellateCell
Plasma
Bcell
Epithelial
Tcell
DuctalCell
Acinar
UMAP_2
UMAP_1
ACTA2, ADIRF, COL1A1...
LUM, COL1A2, COL3A1...
SPRY1, RAMP2, CLDN5...
CLU, ANXA4, DEFB1...
KRT19, MMP7, S100A6...
HLA-DRA, S100A8, FCER1G...
IGJ, MZB1, SSR4...
CTRB2, PRSS1, CTRB1...
IGJ, MZB1, SSR4...
STMN1, TUBA1B, HMGN2...
CD79A, MS4A1, CD79B...
INS, TTR, PCSK1N...
Relative Exp
Low
High
E
SSC-A
CD45
CD11b
CD3CD19
Ly6g
Ly6c
MHCII
F4/80
Monocytes
Macrophage
Eosinophil
Neutrophil
Orthotopic KP-2 αCSF1 treatment
F
No BrdU ctrl
αIgG ctrl
αCSF1
0.06%
4.94%
1.07%
MHCII
No BrdU ctrl
BrdU
BrdU
G
% BrdU⁺ of Macs
*
*
αIgG
αCSF1 12hr
αCSF1 24hr
H
Macs per gram of tissue
n.s.
n.s.
I
% BrdU⁺ of Monocytes
n.s.
n.s.

Figure 3.

Cancer-associated fibroblasts drive tumor associated macrophage proliferation through colony stimulating factor-1 (CSF1). (A) Dot plot summarizing CSF1 expressions in different cell types across three mouse PDAC models from the publicly available scRNAseq dataset (Hosein et al., 2019). **(B)** UMAP dimensionality reduction plot of integrated cells from LKIC, LKP$^{R172H/+}$C, and LKPFC genetically engineered mouse models in scRNAseq dataset used in **A**, annotated with different cell types. Data were filtered and reprocessed as described in the **Methods**. **(C)** Dot plot displaying CSF1 expressions in different cell types across 21 human PDAC patient samples from the publicly available scRNAseq dataset (Peng et al., 2019). **(D)** UMAP dimensionality reduction plot of integrated cells from 21 pancreatic adenocarcinoma patients used in **C**, annotated with different cell types. **(E)** Representative flow cytometry plots showing the gating strategy to identify macrophages, monocytes, neutrophils in orthotopic KP-2 tumors. **(F-I)** Representative flow cytometry plot and quantification bar plot showing BrdU$^+$ macrophages and monocytes, and total number of macrophages following αIgG or αCSF1 injections; n = 6-8 mice per group. Data are presented as the mean ± SEM. n.s., not significant; *p<0.05. For comparisons between any two groups, Student's two-tailed *t*-test was used.

Fig. 4

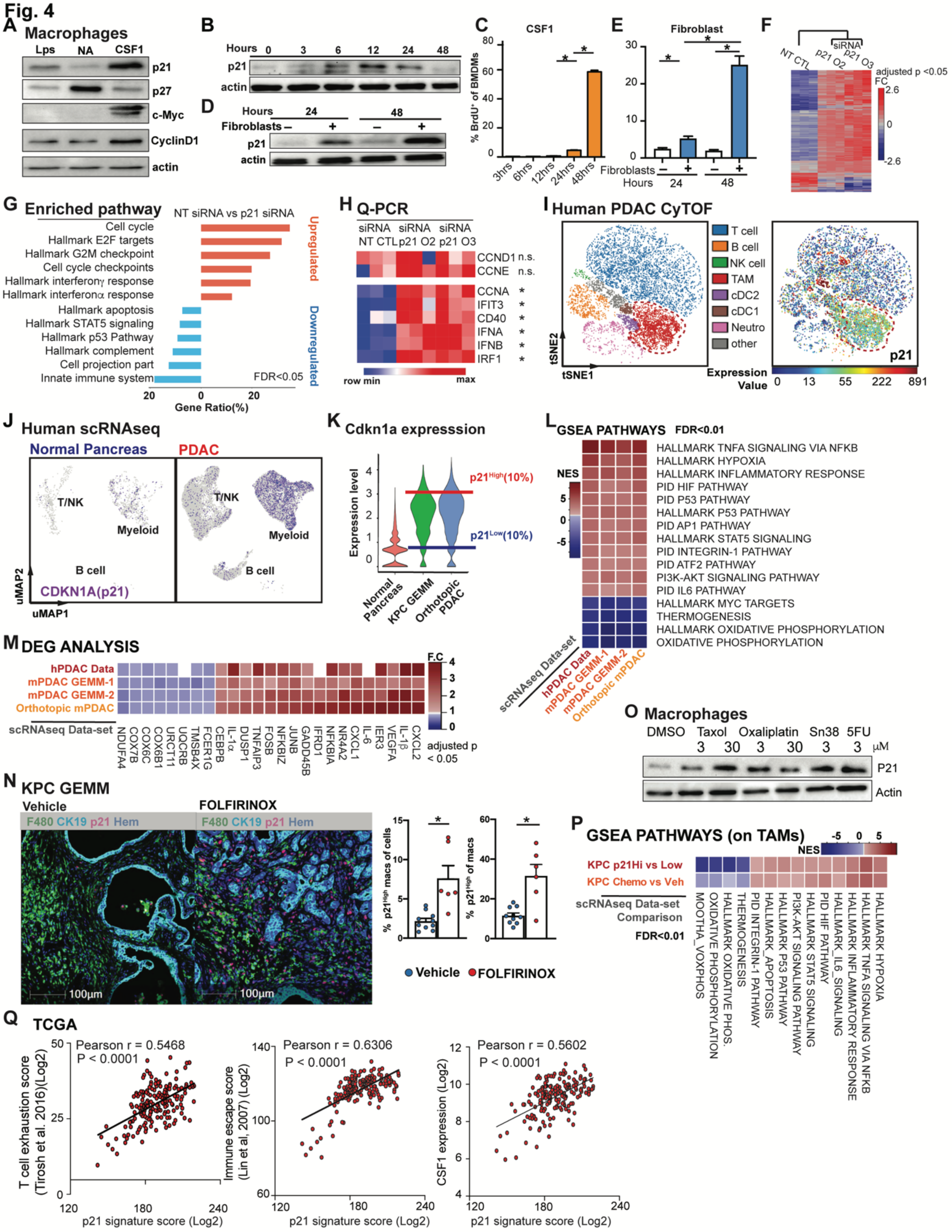
A Macrophages
Lps NA CSF1
p21
p27
c-Myc
CyclinD1
actin
B Hours 0 3 6 12 24 48
p21
actin
C CSF1
% BrdU+ of BMDMs
0 20 40 60 80
3hrs 6hrs 12hrs 24hrs 48hrs
D Hours 24 48
Fibroblasts – + – +
p21
actin
E Fibroblast
0 10 20 30
Fibroblasts – + – +
Hours 24 48
F NT CTL siRNA p21 O2 p21 O3
adjusted p <0.05
FC 2.6 0 -2.6
G Enriched pathway NT siRNA vs p21 siRNA
Cell cycle
Hallmark E2F targets
Hallmark G2M checkpoint
Cell cycle checkpoints
Hallmark interferonγ response
Hallmark interferonα response
Hallmark apoptosis
Hallmark STAT5 signaling
Hallmark p53 Pathway
Hallmark complement
Cell projection part
Innate immune system
Upregulated
Downregulated
FDR<0.05
20 0 20
Gene Ratio(%)
H Q-PCR
siRNA NT CTL siRNA p21 O2 siRNA p21 O3
CCND1 n.s.
CCNE n.s.
CCNA *
IFIT3 *
CD40 *
IFNA *
IFNB *
IRF1 *
row min max
I Human PDAC CyTOF
T cell
B cell
NK cell
TAM
cDC2
cDC1
Neutro
other
tSNE2
tSNE1
p21
Expression Value 0 13 55 222 891
J Human scRNAseq
Normal Pancreas
PDAC
T/NK
Myeloid
B cell
CDKN1A(p21)
uMAP2
uMAP1
K Cdkn1a expresssion
Expression level
0 1 2 3 4
p21High(10%)
p21Low(10%)
Normal Pancreas
KPC GEMM
Orthotopic PDAC
L GSEA PATHWAYS FDR<0.01
NES 5 0 -5
HALLMARK TNFA SIGNALING VIA NFKB
HALLMARK HYPOXIA
HALLMARK INFLAMMATORY RESPONSE
PID HIF PATHWAY
PID P53 PATHWAY
HALLMARK P53 PATHWAY
PID AP1 PATHWAY
HALLMARK STAT5 SIGNALING
PID INTEGRIN-1 PATHWAY
PID ATF2 PATHWAY
PI3K-AKT SIGNALING PATHWAY
PID IL6 PATHWAY
HALLMARK MYC TARGETS
THERMOGENESIS
HALLMARK OXIDATIVE PHOSPHORYLATION
OXIDATIVE PHOSPHORYLATION
scRNAseq Data-set
hPDAC Data
mPDAC GEMM-1
mPDAC GEMM-2
Orthotopic mPDAC
M DEG ANALYSIS
hPDAC Data
mPDAC GEMM-1
mPDAC GEMM-2
Orthotopic mPDAC
scRNAseq Data-set
NDUFA4 COX7B COX6C COX6B1 URCT11 UQCRB TMSB4X FCER1G CEBPB IL-1α DUSP1 TNFAIP3 FOSB NFKBIZ JUNB GADD45B IFRD1 NFKBIA NR4A2 CXCL1 IL-6 IER3 VEGFA IL-1β CXCL2
F.C 4 3 2 1 0
adjusted p < 0.05
O Macrophages
DMSO Taxol Oxaliplatin Sn38 5FU
3 30 3 30 3 3 μM
P21
Actin
N KPC GEMM
Vehicle
FOLFIRINOX
F480 CK19 p21 Hem
100μm
100μm
% p21High macs of cells
% p21High of macs
0 5 10 15
0 20 40 60
*
Vehicle
FOLFIRINOX
P GSEA PATHWAYS (on TAMs)
NES -5 0 5
KPC p21Hi vs Low
KPC Chemo vs Veh
scRNAseq Data-set Comparison
FDR<0.01
MOOTHA_VOXPHOS
OXIDATIVE PHOSPHORYLATION
HALLMARK OXIDATIVE PHOS.
THERMOGENESIS
PID INTEGRIN-1 PATHWAY
HALLMARK_APOPTOSIS
HALLMARK P53 PATHWAY
PI3K-AKT SIGNALING PATHWAY
HALLMARK STAT5 SIGNALING
PID HIF PATHWAY
HALLMARK_IL6_SIGNALING
HALLMARK INFLAMMATORY RESPONSE
HALLMARK TNFA SIGNALING VIA NFKB
HALLMARK HYPOXIA
Q TCGA
Pearson r = 0.5468
P < 0.0001
T cell exhaustion score (Tirosh et al. 2016)(Log2)
0 25 50
Pearson r = 0.6306
P < 0.0001
Immune escape score (Lin et al, 2007) (Log2)
60 100 140
Pearson r = 0.5602
P < 0.0001
CSF1 expression (Log2)
4 6 8 10 12
120 180 240
p21 signature score (Log2)

Figure 4.

The p21 cell cycle-dependent kinase inhibitor is induced by CSF1 and regulates the macrophage phenotype. **(A)** Immunoblots of p21, p27, c-Myc, and cyclinD1 in bone marrow-derived macrophages (BMDMs) after treatment with 100 ng/mL of lipopolysaccharide or colony stimulating factor-1 (CSF1) for 24 h. The experiments were repeated three times. **(B)** Immunoblot displaying p21 expression in BMDMs following 4 ng/mL CSF1 treatment at time 0 with quantification of BrdU$^+$ BMDMs shown in **(C)**, 5-bromo-2'-deoxyuridine (BrdU) was added at time 0 and pulsed until harvest. BMDMs were starved without CSF1 overnight. **(D)** Immunoblot displaying p21 expression in BMDMs combined with fibroblasts in Transwell assays at time 0. **(E)** Bar plot displaying the quantification of BrdU$^+$ BMDMs in **D**. **(F)** Heat map displaying the microarray analysis of differentially expressed genes (DEGs) between non-target siRNA treated or siRNA targeting for p21 treated BMDMs cultured in tumor-conditioned medium for 24 h; n = 3 per group. Genes were filtered with adjusted $p < 0.05$ and fold-change > or < 1.5. **(G)** Bar graph displaying top overrepresentation analysis of DEGs in **F** to known biological functions [Gene Ontology (GO), Kyoto Encyclopedia of Genes and Genomes (KEGG), REACTOME, and Molecular Signatures Database (MSigDB)] with a false discovery rate (FDR) < 0.05. **(H)** Heat map displaying qPCR analysis of gene expressions of cell cycle and interferon-related genes between non-target siRNA treated or siRNA targeting for p21 treated BMDMs cultured in tumor-conditioned medium for 24 h; fold-change > 1.5, n = 3/group of the comparison. **(I)** Representative tSNE plot displaying major cell types from CyTOF analysis of a human PDAC patient (same as in **Fig. 1 C**) with macrophages circled in red and p21 expression. **(J)** UMAP displaying CDKN1A gene expression in CD45$^+$ cells from the human PDAC scRNAseq dataset (Peng et al., 2019) with annotation of key cell types. **(K)** Violin plot showing the expression levels for p21 gene in macrophage clusters from integrated scRNAseq analyses of the mouse normal pancreas and pancreatic tissue from KPC GEMMs and orthotopic KP-2 tumor-bearing mice. Representative lines were drawn for two groups of stratified macrophages based on the top 10% of p21 expression and bottom 10% of p21 expression. **(L)** Heat map of net enrichment score (NES) of shared enriched pathways identified by GSEA analysis comparing the two groups of macrophages (p21^{High} vs. p21^{Low}) in human PDAC scRNAseq dataset (23), (27), KPC GEMM and orthotopic scRNAseq data. Enriched pathways were selected by FDR < 0.01. **(M)** Heat map displaying the shared DEGs when comparing p21^{High} to p21^{Low} tumor-associated macrophages (TAMs) in each dataset with adjusted $p < 0.05$ and fold-change > 1.2 or < 0.8. p21^{High} signature score was created utilizing filtered DEGs with fold-change > 1.5 across three mouse scRNAseq datasets. **(N)** Representative mpIHC image displaying F4/80$^+$ TAMs, CK19$^+$ tumor cells, and p21$^+$ cells in KPC GEMM treated with dimethyl sulfoxide or FOLFIRINOX for 24 h with quantification of p21$^+$TAMs as total cells and total TAMs on the right. **(O)** Immunoblots showing expressions of p21 in BMDMs after treatment with chemotherapeutics for 24 h. **(P)** Heat map of NES of shared enriched pathways identified by GSEA analysis in comparing p21^{High} to p21^{Low} TAMs in KPC GEMM PDAC and in comparing chemotherapeutic treated KPC GEMM PDAC to DMSO treated KPC GEMM PDAC with FDR < 0.05. **(Q)** Correlation plots with Pearson coefficients (r) of p21 signature score vs. T cell exhaustion score (Tirosh et al., 2016), Immune escape score (Lin et al., 2007), and CSF1 expression from TCGA PDAC PanCancer Atlas study (n=180).

All graphs are expressed as the mean ± SEM. n.s., not significant; *p < 0.05. All *in vitro* assays and immunoblots were consistent across more than two independent repeats. For comparisons between any two groups, Student's two-tailed *t*-test was used, except for **F, M** where the Bonferroni correction was used and for **L, P** where the FDR was used.

Fig.5

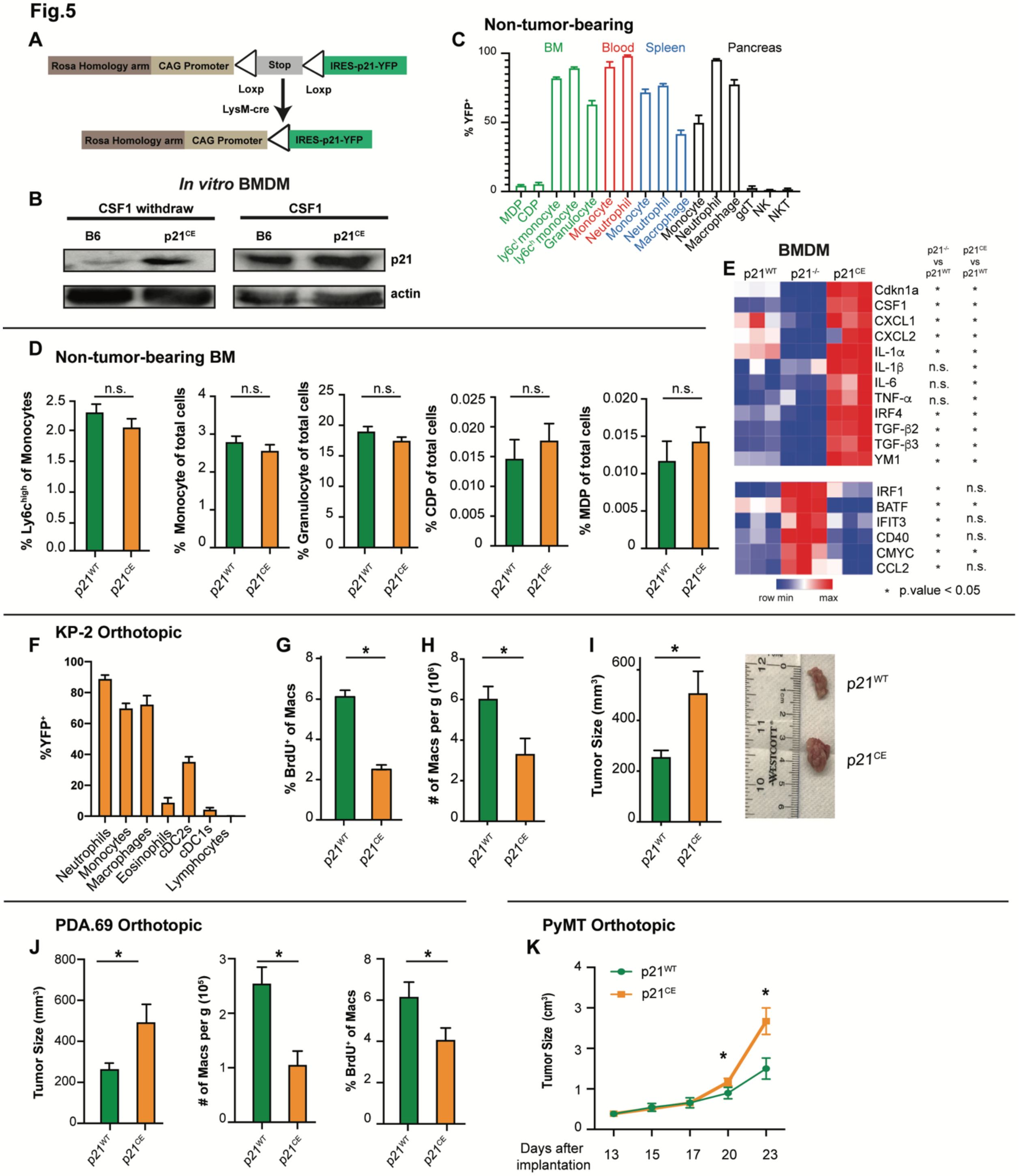
A
Rosa Homology arm
CAG Promoter
Stop
IRES-p21-YFP
Loxp
Loxp
LysM-cre
Rosa Homology arm
CAG Promoter
IRES-p21-YFP
B
In vitro BMDM
CSF1 withdraw
CSF1
B6
p21^CE
B6
p21^CE
p21
actin
C
Non-tumor-bearing
BM
Blood
Spleen
Pancreas
% YFP+
100
50
0
MDP
CDP
ly6c^hi monocyte
ly6c^lo monocyte
Granulocyte
Monocyte
Neutrophil
Monocyte
Neutrophil
Macrophage
Monocyte
Neutrophil
Macrophage
gdT
NK
NKT
D
Non-tumor-bearing BM
% Ly6c^high of Monocytes
% Monocyte of total cells
% Granulocyte of total cells
% CDP of total cells
% MDP of total cells
n.s.
p21^WT
p21^CE
E
BMDM
p21^WT
p21^-/-
p21^CE
p21^-/- vs p21^WT
p21^CE vs p21^WT
Cdkn1a * *
CSF1 * *
CXCL1 * *
CXCL2 * *
IL-1α * *
IL-1β n.s. *
IL-6 n.s. *
TNF-α n.s. *
IRF4 * *
TGF-β2 * *
TGF-β3 * *
YM1 * *
IRF1 * n.s.
BATF * *
IFIT3 * n.s.
CD40 * n.s.
CMYC * *
CCL2 * n.s.
row min
max
* p.value < 0.05
F
KP-2 Orthotopic
%YFP+
Neutrophils
Monocytes
Macrophages
Eosinophils
cDC2s
cDC1s
Lymphocytes
G
% BrdU+ of Macs
H
# of Macs per g (10^6)
I
Tumor Size (mm^3)
p21^WT
p21^CE
J
PDA.69 Orthotopic
Tumor Size (mm^3)
# of Macs per g (10^5)
% BrdU+ of Macs
K
PyMT Orthotopic
p21^WT
p21^CE
Tumor Size (cm^3)
Days after implantation
13
15
17
20
23
*

Figure 5.

Expression of p21 drives tumor promoting phenotypes in macrophages. **(A)** Genetic loci for the p21^{CE} model. **(B)** Immunoblot for p21 expression in p21^{CE} or B6-derived bone marrow-derived macrophages (BMDMs) with or without 10ng/ml of colony stimulating factor-1 (CSF1) treatment for 24 h. Experiments were consistent in two independent repeats. **(C)** Bar plot displaying the percentage of YFP^{+} cells in non-tumor-bearing p21^{CE} mice; n = 4. **(D)** Bar plot showing flow cytometry quantification of cellular composition in non-tumor-bearing bone marrow from p21^{CE} and p21^{WT} mice; n = 6–9 mice/group. **(E)** Heat map displaying gene expression analysis of BMDMs derived from non-tumor-bearing p21^{WT}, p21$^{-/-}$, and p21^{CE} mice treated with 10ng/ml of CSF1 for 24 h, by RT-qPCR; n = 3/group, data was consistent from three independent repeats. **(F)** Flow cytometry quantification of YFP^{+} cells in p21^{CE} mice bearing orthotopic KP-2 tumors; n = 6–7 mice. **(G,H)** Quantification of BrdU^{+} macrophages and density of macrophages in tumors of p21^{CE} and p21^{WT} mice; n = 6–7 mice/group. Data were pooled across multiple independent experiments. **(I)** Bar plot displaying the tumor sizes in p21^{CE} and p21^{WT} mice, 21–27 days following orthotopic implantation of KP-2 tumor cells; n = 8–10 mice/group. **(J)** Bar plot displaying tumor sizes, density of macrophages, and quantification of BrdU^{+} macrophages from p21^{CE} and p21^{WT} mice, 21–23 days after the orthotopic implantation of the PDA.69 cell line; n = 8–10 mice/group. Data were pooled from multiple independent experiments. **(K)** Caliper measurement of orthotopic PyMT in p21^{WT} and p21^{CE} mice; n = 6–8 mice /group. All graphs are expressed as the mean ± SEM. n.s., not significant; *$p < 0.05$. All *in vitro* assays were consistent across more than two dependent repeats. For comparisons between any two groups, Student’s two-tailed *t*-test was used.

Fig. 6

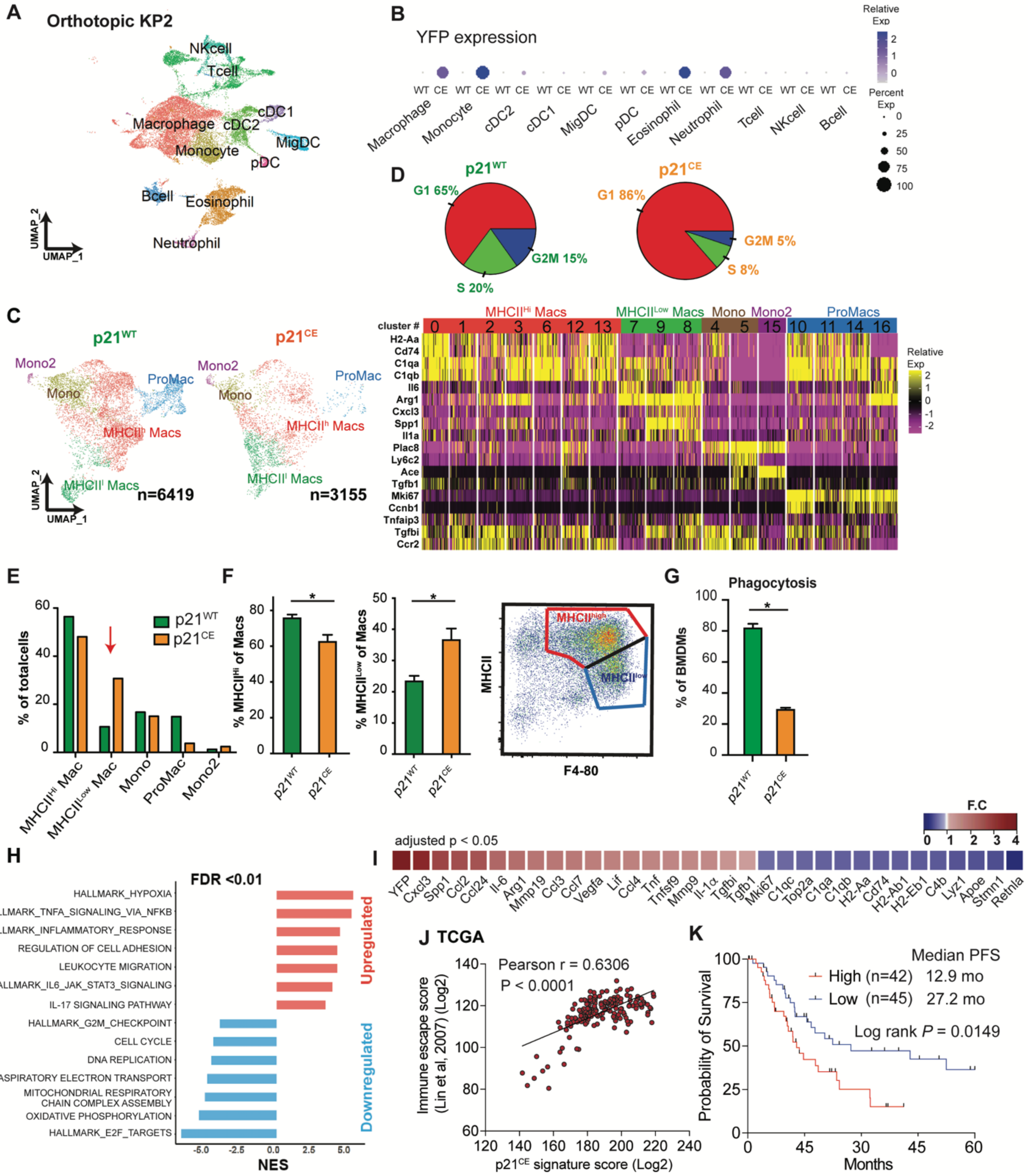
A
Orthotopic KP2
NKcell
Tcell
cDC1
Macrophage
cDC2
MigDC
Monocyte
pDC
Bcell
Eosinophil
Neutrophil
UMAP_2
UMAP_1
B
YFP expression
WT CE
Macrophage
Monocyte
cDC2
cDC1
MigDC
pDC
Eosinophil
Neutrophil
Tcell
NKcell
Bcell
Relative Exp
2
1
0
Percent Exp
0
25
50
75
100
D
p21WT
G1 65%
G2M 15%
S 20%
p21CE
G1 86%
G2M 5%
S 8%
C
p21WT
p21CE
Mono2
Mono
ProMac
MHCIIh Macs
MHCIIl Macs
n=6419
n=3155
UMAP_2
UMAP_1
cluster #
MHCIIHi Macs
MHCIILow Macs
Mono
Mono2
ProMacs
0 1 2 3 6 12 13 7 9 8 4 5 15 10 11 14 16
H2-Aa
Cd74
C1qa
C1qb
Il6
Arg1
Cxcl3
Spp1
Il1a
Plac8
Ly6c2
Ace
Tgfb1
Mki67
Ccnb1
Tnfaip3
Tgfbi
Ccr2
Relative Exp
2
1
0
-1
-2
E
% of totalcells
60
40
20
0
p21WT
p21CE
MHCIIHi Mac
MHCIILow Mac
Mono
ProMac
Mono2
F
% MHCIIHi of Macs
80
60
40
20
0
*
p21WT
p21CE
% MHCIILow of Macs
50
40
30
20
10
0
*
MHCIIhigh
MHCIIlow
MHCII
F4-80
G
Phagocytosis
% of BMDMs
100
80
60
40
20
0
*
p21WT
p21CE
H
FDR <0.01
HALLMARK_HYPOXIA
HALLMARK_TNFA_SIGNALING_VIA_NFKB
HALLMARK_INFLAMMATORY_RESPONSE
REGULATION OF CELL ADHESION
LEUKOCYTE MIGRATION
HALLMARK_IL6_JAK_STAT3_SIGNALING
IL-17 SIGNALING PATHWAY
HALLMARK_G2M_CHECKPOINT
CELL CYCLE
DNA REPLICATION
RASPIRATORY ELECTRON TRANSPORT
MITOCHONDRIAL RESPIRATORY CHAIN COMPLEX ASSEMBLY
OXIDATIVE PHOSPHORYLATION
HALLMARK_E2F_TARGETS
Upregulated
Downregulated
-5.0 -2.5 0.0 2.5 5.0
NES
I
adjusted p < 0.05
F.C
0 1 2 3 4
YFP
Cxcl3
Spp1
Ccl2
Ccl24
Il-6
Arg1
Mmp19
Ccl3
Ccl7
Vegfa
Lif
Ccl4
Tnf
Tnfsf9
Mmp9
Il-1α
Tgfbi
Tgfb1
Mki67
C1qc
Top2a
C1qa
C1qb
H2-Aa
Cd74
H2-Ab1
H2-Eb1
C4b
Lyz1
Apoe
Stmn1
Retnla
J TCGA
Pearson r = 0.6306
P < 0.0001
Immune escape score (Lin et al, 2007) (Log2)
140
120
100
80
60
120 140 160 180 200 220 240
p21CE signature score (Log2)
K
Median PFS
High (n=42) 12.9 mo
Low (n=45) 27.2 mo
Log rank P = 0.0149
Probability of Survival
100
75
50
25
0
0 45 30 45 60
Months

Figure 6.

The p21 expression in macrophages led to an inflammatory but immunosuppressive phenotype. **(A)** UMAP dimensionality reduction plot of total CD45$^+$ cells from p21^{WT} and p21^{CE} mice bearing orthotopic KP-2 tumors. Cells in each genotype were pooled from three mice and created as two libraries. Clusters were annotated with corresponding cell types. **(B)** Dot plot displaying YFP expression in each cell type between the two groups. The legend shows the dot size and corresponding percentage that are expressed as a color gradient of normalized expressions. **(C)** Reclustered UMAP plot of macrophage and monocyte clusters in **A** without cell cycle regression and split into p21^{WT} and p21^{CE}, and annotated with major subpopulations. on the right, heat map showing key gene expressions in each subpopulation in **C**. **(D)** Pie chart showing cell cycle analysis of macrophages (MHCII^{hi}, MHCII^{low}, and ProMac) in tumors from p21^{WT} and p21^{CE} mice. **(E),** Bar plot showing quantification of each population between p21^{WT} and p21^{CE} mice identified in **C**. **(F)** Quantification of flow cytometry analysis of the percentages of MHCII^{hi} and MHCII^{low} macrophages from p21^{CE} and p21^{WT} mice bearing orthotopic KP-2 tumors with the representative gating strategy; n = 6–10 mice/group. Data were consistent in four independent repeats. **(G)** Barplot displaying quantification of fluorescent-bead$^+$ bone marrow-derived macrophages from p21^{WT} and p21^{CE} mice. Data were consistent in three independent repeats. **(H)** Bar plot displaying Gene Set Enrichment Analysis results of comparing tumor-associated macrophages (TAMs) from p21^{CE} to p21^{WT} mice. The key upregulated and downregulated pathways are shown with a false discovery rate < 0.01. **(I)** Heat map showing the key differentially-expressed genes (DEGs) comparing TAMs from p21^{CE} and p21^{WT} mice. DEGs were filtered with an adjusted $p < 0.05$ and fold-change > 1.3 or < 0.75. All gene expressions were normalized by SCTransform. **(J)** Correlation plots with Pearson coefficients (r) of p21^{CE} signature score (included genes with LogFC >0.75) vs. Immune escape score from TCGA PDAC PanCancer Atlas study (n=180). **(K)** Kaplan-Meier survival analysis of PDA patients from TCGA whose samples were stratified by expression of the p21^{CE} signature (LogFC >0.75) by quartiles. All graphs are expressed as the mean ± SEM. n.s., not significant; $^*p < 0.05$ using the *t*-test, except for **I** where the Bonferroni-corrected adjusted p-value was used.

Fig. 7

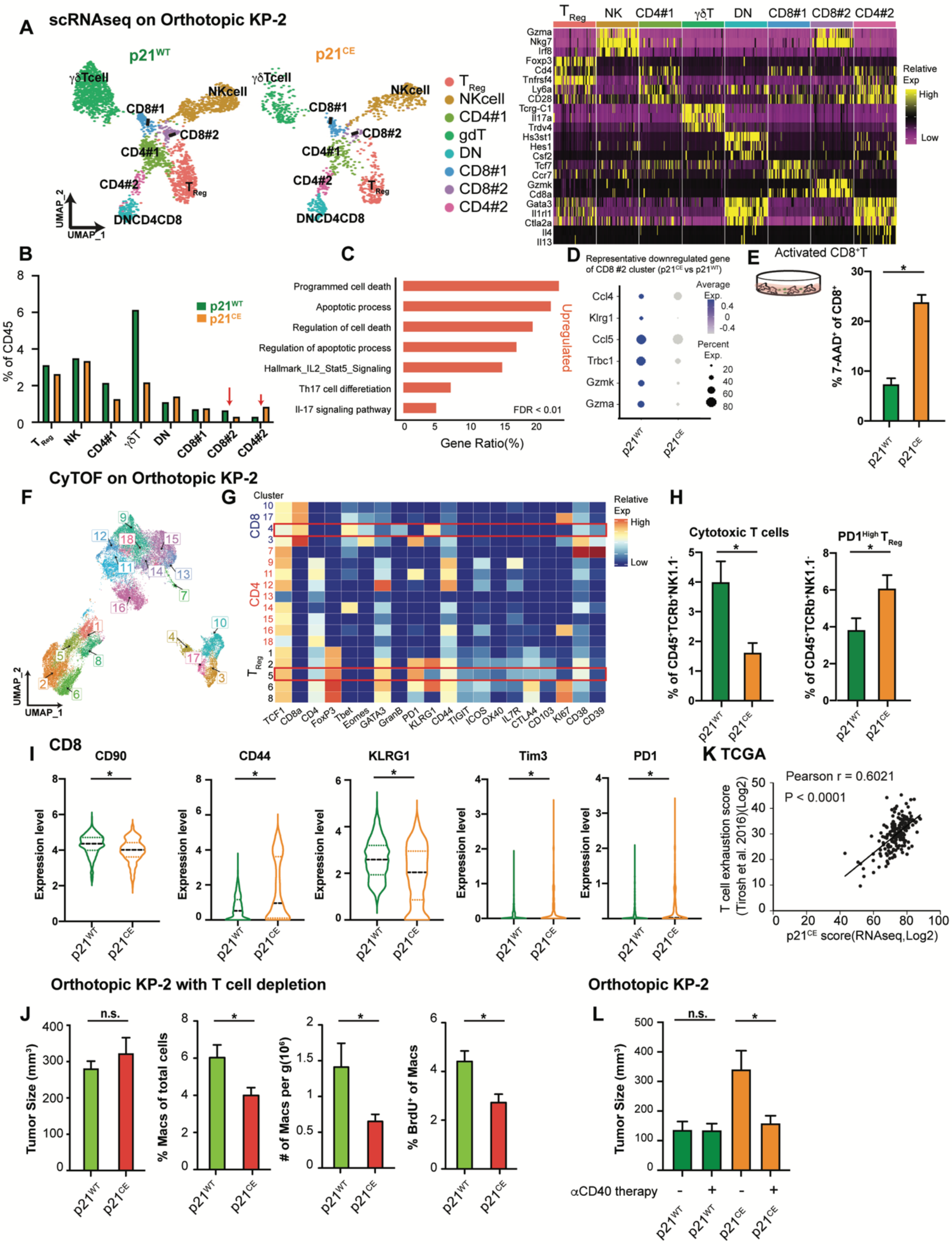
A
scRNAseq on Orthotopic KP-2
p21WT
p21CE
γδTcell
NKcell
CD8#1
CD8#2
CD4#1
CD4#2
TReg
DNCD4CD8
UMAP_1
UMAP_2
TReg
NKcell
CD4#1
gdT
DN
CD8#1
CD8#2
CD4#2
TReg NK CD4#1 γδT DN CD8#1 CD8#2 CD4#2
Gzma Nkg7 Irf8 Foxp3 Cd4 Tnfrsf4 Ly6a CD28 Tcrg-C1 Il17a Trdv4 Hs3st1 Hes1 Csf2 Tcf7 Ccr7 Gzmk Cd8a Gata3 Il1rl1 Ctla2a Il4 Il13
Relative Exp
High
Low
B
% of CD45
p21WT
p21CE
TReg NK CD4#1 γδT DN CD8#1 CD8#2 CD4#2
C
Programmed cell death
Apoptotic process
Regulation of cell death
Regulation of apoptotic process
Hallmark_IL2_Stat5_Signaling
Th17 cell differetiation
Il-17 signaling pathway
Upregulated
FDR < 0.01
Gene Ratio(%)
D
Representative downregulated gene of CD8 #2 cluster (p21CE vs p21WT)
Ccl4 Klrg1 Ccl5 Trbc1 Gzmk Gzma
Average Exp.
Percent Exp.
p21WT p21CE
E
Activated CD8+T
% 7-AAD+ of CD8+
*
p21WT p21CE
CyTOF on Orthotopic KP-2
F
UMAP_1
UMAP_2
G
Cluster
CD8
CD4
TReg
TCF1 CD8a CD4 FoxP3 Tbet Eomes GATA3 GranB PD1 KLRG1 CD44 TIGIT ICOS OX40 IL7R CTLA4 CD103 Ki67 CD38 CD39
Relative Exp
High
Low
H
Cytotoxic T cells
% of CD45+TCRb+NK1.1-
PD1High TReg
% of CD45+TCRb+NK1.1-
*
p21WT p21CE
I
CD8
CD90
CD44
KLRG1
Tim3
PD1
Expression level
*
p21WT p21CE
K TCGA
Pearson r = 0.6021
P < 0.0001
T cell exhaustion score (Tirosh et al. 2016)(Log2)
p21CE score(RNAseq,Log2)
Orthotopic KP-2 with T cell depletion
J
Tumor Size (mm3)
% Macs of total cells
# of Macs per g(106)
% BrdU+ of Macs
n.s.
*
p21WT p21CE
Orthotopic KP-2
L
Tumor Size (mm3)
αCD40 therapy - + - +
p21WT p21WT p21CE p21CE

Figure 7.

The p21 expression in macrophages impaired effector T cells. **(A)** UMAP dimensionality reduction plot of selected lymphocytes (clusters 6, 7, 8, 13, and 17 in Fig. S4, A and B) from p21^{WT} and p21^{CE} orthotopic KP-2 tumors. Clusters were annotated with corresponding cell types and heat maps displaying selected gene expressions in each cell type. **(B)** Bar graph displaying the composition of each cell type as the percentage of total CD45$^+$ cells in p21^{WT} and p21^{CE} tumor-bearing mice. CD8#2 and CD4#2 are highlighted with red arrows. **(C)** Bar graph displaying the upregulated pathways in the CD8#2 cluster from p21^{CE} using overrepresentation analysis of differentially-expressed genes (DEGs) to known biological functions (Gene Ontology, Kyoto Encyclopedia of Genes and Genomes, REACTOME, and the Molecular Signal Database). DEGs were filtered with a value of $p < 0.05$, fold-change > 1.2, and past MAST test. **(D)** Table showing the differentially expressed genes comparing CD8#2 cluster from p21^{CE} to p21^{WT} with p.value < 0.05. **(E)** Bar plot displaying the percentage of 7-AAD$^+$CD8$^+$ T cells activated with CD3/CD28 Dynabeads (Gibco) when cocultured with BMDMs from p21^{CE} and p21^{WT} mice for 48 h. Data were consistent in three independent repeats. **(F)** UMAP plot of selected CD45$^+$TCRb$^+$CD90$^+$NK1.1$^-$TCR$^-\gamma\delta$T$^-$ cells from p21^{CE} and p21^{WT} orthotopic KP-2 tumors with clusters annotated; n = 7 mice/group. **(G)** Heat map displaying the feature expressions in each cluster. Cytotoxic T cells (cluster 4) and PD1^{High} T$_{reg}$ (cluster 5) were highlighted. **(H)** Bar plot showing the percentages of cytotoxic T cells and PD1^{High} T$_{reg}$ in p21^{WT} and p21^{CE} tumors. **(I)** Violin plot visualizing the expression levels of CD90, CD44, KLRG1, TIM3, and PD1 in the CD8 cluster between tumors from two genotypes. **(J)** Bar graphs showing the tumor burden, macrophages as the percentage of total cells, or as per gram of tissue, and the percentage of BrdU$^+$ macrophages between p21^{WT} and p21^{CE} orthotopic KP-2 tumors after αCD4/CD8 treatment; n = 6 mice/group. **(K)** Correlation plots with Pearson coefficients (r) of p21^{CE} score vs. T cell exhaustion score from TCGA PDAC PanCancer Atlas study (n=180). **(L)** Bar graph showing the tumor burdens of p21^{WT} and p21^{CE} mice bearing orthotopic KP-2 tumors with or without CD40 agonist and gemcitabine treatment. n= 5-6 mice/group. All graphs are expressed as the mean ± SEM. n.s., not significant; $^*p < 0.05$ for comparisons between two groups **E,H,J,L**, Student's two-tailed *t*-test was used. For comparisons in **I**, the Bonferroni-corrected p-value was used.

Fig. S1

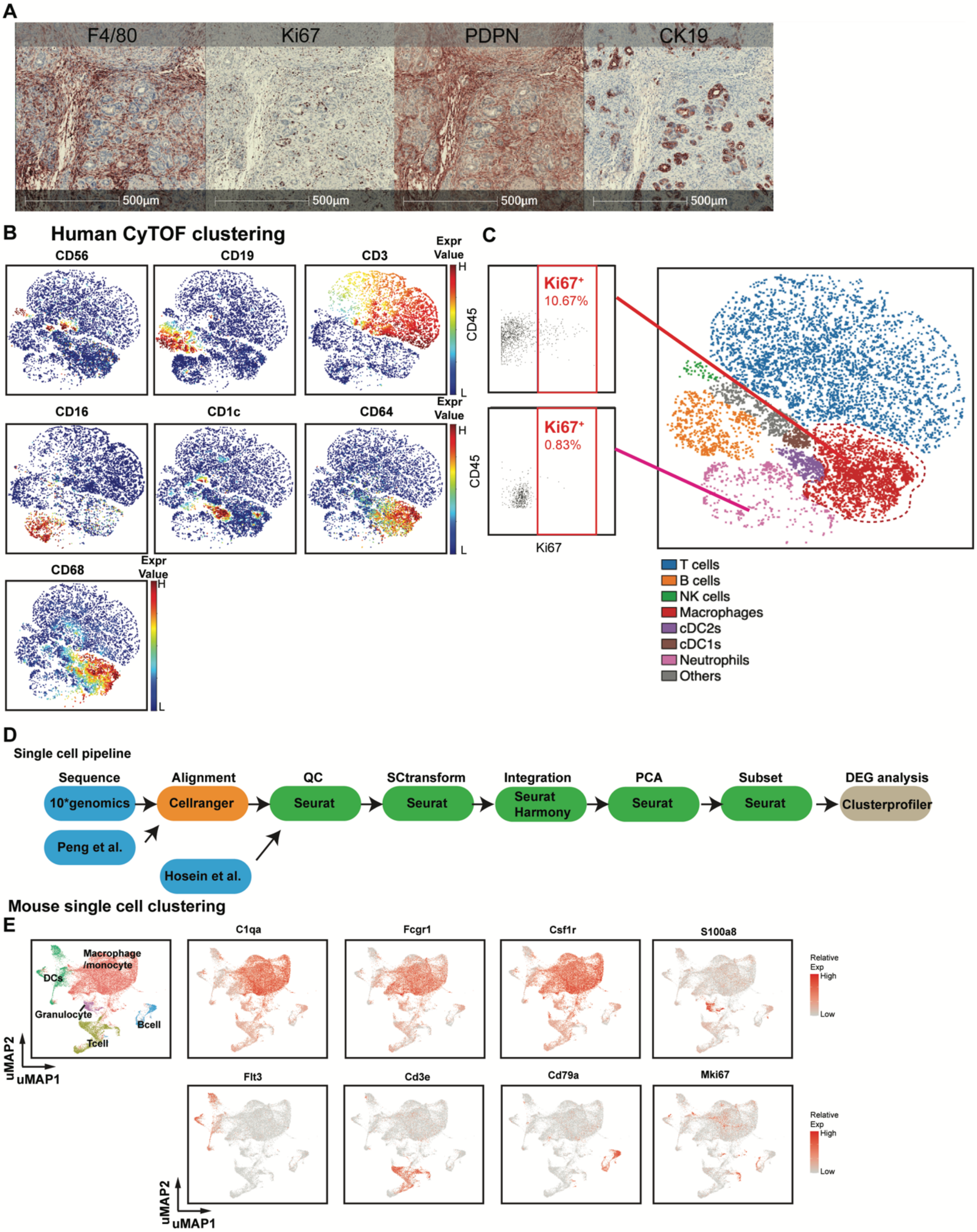
A
F4/80
Ki67
PDPN
CK19
500μm
500μm
500μm
500μm
B
Human CyTOF clustering
CD56
CD19
CD3
Expr Value
H
L
CD16
CD1c
CD64
Expr Value
H
L
CD68
Expr Value
H
L
C
Ki67⁺
10.67%
CD45
Ki67⁺
0.83%
CD45
Ki67
T cells
B cells
NK cells
Macrophages
cDC2s
cDC1s
Neutrophils
Others
D
Single cell pipeline
Sequence
10*genomics
Peng et al.
Alignment
Cellranger
Hosein et al.
QC
Seurat
SCtransform
Seurat
Integration
Seurat Harmony
PCA
Seurat
Subset
Seurat
DEG analysis
Clusterprofiler
Mouse single cell clustering
E
Macrophage /monocyte
DCs
Granulocyte
Bcell
Tcell
uMAP2
uMAP1
C1qa
Fcgr1
Csf1r
S100a8
Relative Exp
High
Low
Flt3
Cd3e
Cd79a
Mki67
Relative Exp
High
Low
uMAP2
uMAP1

Figure S1.

(A) Representative image of multiplex immunochemistry (mpIHC) staining for F4/80$^+$, Ki67$^+$, PDPN$^+$, and CK19$^+$ cells in p48$^-$Cre$^+$/LSL-Kras^{G12D}/p53$^{flox/flox}$ (KPC) genetically engineered mouse model (GEMM) pancreatic ductal adenocarcinoma (PDAC) tumors. Individual staining of the same samples were deconvoluted and merged through HALO software. Markers of interest were pseudo-colored and quantified through the Indica Labs-Highplex FL v.4.0.3 algorithm; n = 6.

(B) Representative tSNE plots of human pancreatic adenocarcinoma (PDAC) samples, displaying markers used for identifying major cell types, CD56$^+$ for natural killer cells, CD19$^+$CD3$^+$ for T cells, CD16$^+$ for neutrophils, CD68$^+$CD64$^+$CD14$^+$ for macrophages, CD1c$^+$ for cDC2, and CD141$^+$ for cDC1 cells; n = 9 PDAC patients.

(C) Representative Ki67$^+$ gating in macrophage and neutrophil clusters.

(D) Schematic of the scRNAseq analysis pipeline. Details of each step for the specific dataset are listed in **Methods.**

(E) UMAP plots of integrated sorted murine CD45$^+$ cells (from normal pancreas, pancreatic tissues from KPC GEMMs and orthotopic PDAC tumors) with normalized expression levels of key genes across subpopulations.

Fig. S2

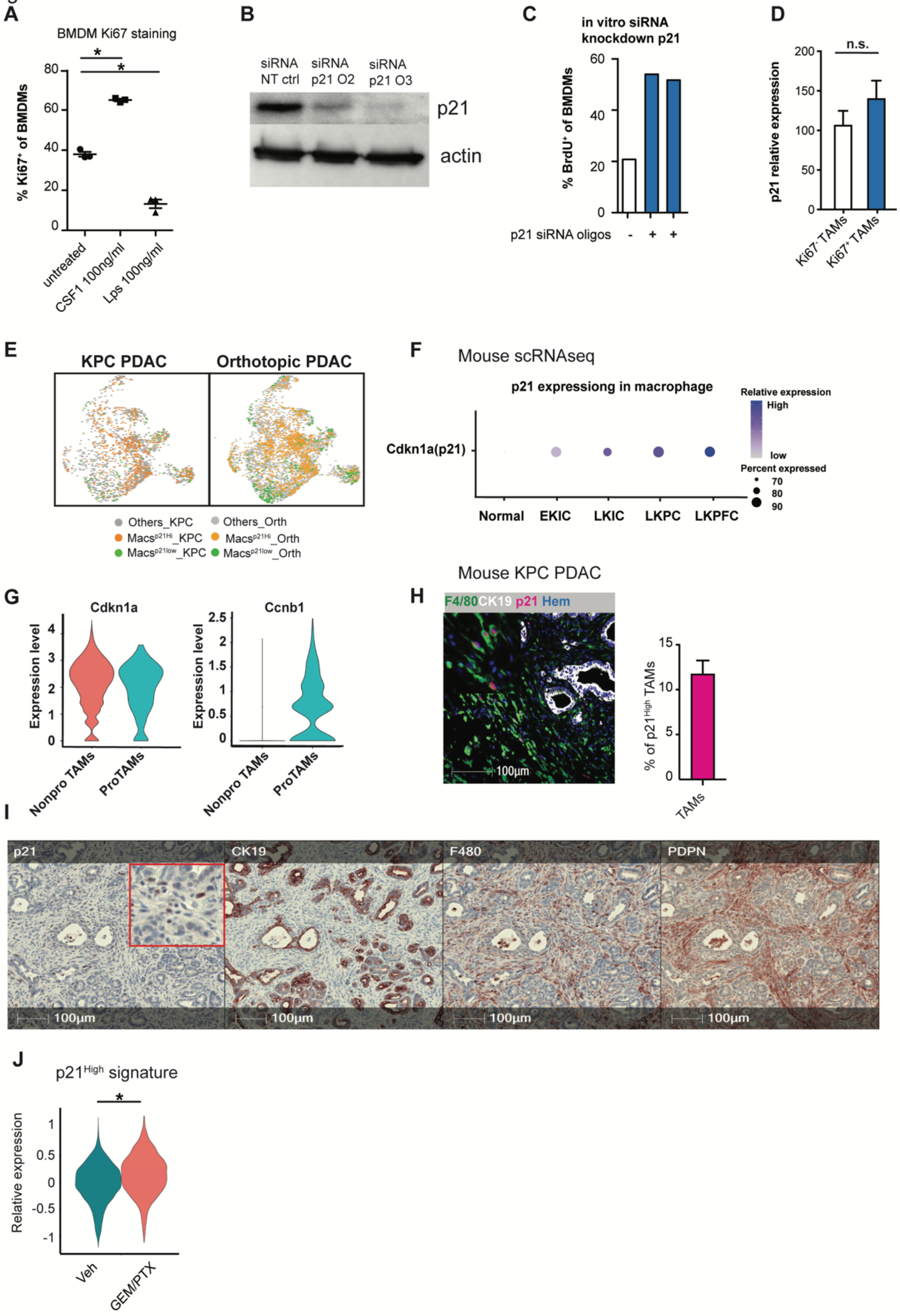
A
BMDM Ki67 staining
% Ki67⁺ of BMDMs
0
20
40
60
80
*
*
untreated
CSF1 100ng/ml
Lps 100ng/ml
B
siRNA NT ctrl
siRNA p21 O2
siRNA p21 O3
p21
actin
C
in vitro siRNA knockdown p21
% BrdU⁺ of BMDMs
0
20
40
60
p21 siRNA oligos
-
+
+
D
n.s.
p21 relative expression
0
50
100
150
200
Ki67⁻ TAMs
Ki67⁺ TAMs
E
KPC PDAC
Orthotopic PDAC
Others_KPC
Macs^p21Hi_KPC
Macs^p21low_KPC
Others_Orth
Macs^p21Hi_Orth
Macs^p21low_Orth
F
Mouse scRNAseq
p21 expressiong in macrophage
Cdkn1a(p21)
Normal
EKIC
LKIC
LKPC
LKPFC
Relative expression
High
low
Percent expressed
70
80
90
G
Cdkn1a
Expression level
0
1
2
3
4
Nonpro TAMs
ProTAMs
Ccnb1
Expression level
0
0.5
1
1.5
2
2.5
Nonpro TAMs
ProTAMs
H
Mouse KPC PDAC
F4/80 CK19 p21 Hem
100µm
% of p21^High TAMs
0
5
10
15
TAMs
I
p21
CK19
F480
PDPN
100µm
100µm
100µm
100µm
J
p21^High signature
*
Relative expression
1
0.5
0
-0.5
-1
Veh
GEM/PTX

Figure S2.

(A) Dot plot displaying the percentage of Ki67$^+$ macrophages in bone marrow-derived macrophages (BMDMs) after colony stimulating factor-1 (CSF1) or lipopolysaccharide treatment for 24 h; n = 3/group.

(B) Immunoblot showing expression of p21 in BMDMs after treatment with non-targeting siRNA or siRNA targeting for p21 in the presence of CSF1 for 24 h. Experiments were repeated in more than three independent repeats, and also included tumor conditioned-medium (TCM) treatment or were cultured with fibroblasts in Transwell assays.

(C) Bar plot displaying quantification of BrdU$^+$ BMDMs in **B.** The 5-bromo-2'-deoxyuridine (BrdU) was pulsed for 20 h. The experiments were repeated three times with three different siRNA oligonucleotides.

(D) Bar plot showing the expression levels of p21 in Ki67$^+$ and Ki67$^-$ tumor-associated macrophages (TAMs) identified in **Fig. S1 C**; n = 9.

(E) UMAP displaying p21^{High} and p21^{Low} macrophages in p48$^-$Cre$^+$/LSL-Kras^{G12D}/p53$^{flox/flox}$ (KPC) pancreatic ductal adenocarcinoma (PDAC) tumors and orthotopic KP-2 tumors.

(F) Dot plot showing Cdkn1a (p21) gene expressions in the normal pancreas and pancreatic tissue from EKIC, LKIC, LKPC, and LKPFC genetically engineered mouse models (Hosein et al., 2019).

(G) Violin plot of the expressions of p21 and Ccnb1 in non-proliferating and proliferating macrophages in the mouse scRNAseq dataset from the KPC, orthotopic KP-2, and normal pancreas in **Fig. 1 L**.

(H) Representative image of multiplex immunochemistry (mpIHC) for F4/80$^+$ macrophages, CK19$^+$ tumor cells, and p21$^+$ cells with quantification of p21$^+$ macrophages from KPC PDACs; n = 8.

(I) Representative mpIHC images of KPC mouse PDACs displaying p21, CK19, F4/80, and Pdpn staining; n = 8.

(J) Violin plot displaying the expressions of p21^{High} signature scores, identified in **Fig. 4 M**, in tumor-associated macrophages from KPC mice 24 h after gemcitabine and paclitaxel (GEM/PTX) or dimethyl sulfoxide treatment. All graphs are expressed as the mean ± SEM. n.s., not significant; *$p < 0.05$. All *in vitro* assays were consistent across more than two independent repeats. For comparisons between any two groups, Student's two-tailed *t*-test was used, except for **J** where the Bonferroni-corrected adjusted p-value was used.

Fig. S3

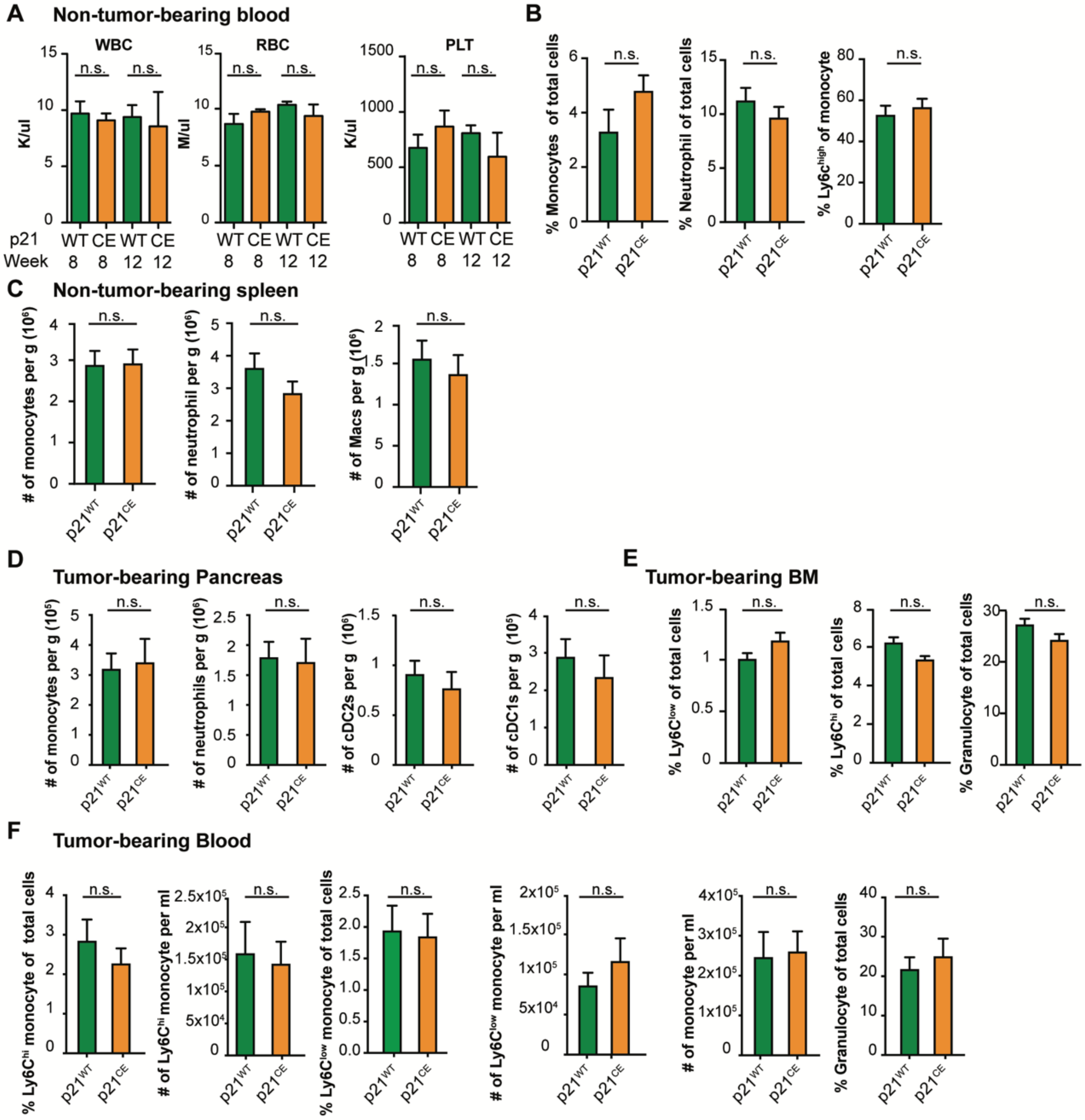
A
Non-tumor-bearing blood
WBC
RBC
PLT
K/ul
M/ul
K/ul
n.s.
p21 WT CE WT CE
Week 8 8 12 12
B
% Monocytes of total cells
% Neutrophil of total cells
% Ly6c^{high} of monocyte
p21^{WT}
p21^{CE}
C
Non-tumor-bearing spleen
# of monocytes per g (10^6)
# of neutrophil per g (10^6)
# of Macs per g (10^6)
D
Tumor-bearing Pancreas
# of monocytes per g (10^5)
# of neutrophils per g (10^6)
# of cDC2s per g (10^5)
# of cDC1s per g (10^5)
E
Tumor-bearing BM
% Ly6C^{low} of total cells
% Ly6C^{hi} of total cells
% Granulocyte of total cells
F
Tumor-bearing Blood
% Ly6C^{hi} monocyte of total cells
# of Ly6C^{hi} monocyte per ml
% Ly6C^{low} monocyte of total cells
# of Ly6C^{low} monocyte per ml
# of monocyte per ml
% Granulocyte of total cells

Figure S3.

(A) Quantification of white blood cells, red blood cells, and platelets in non-tumor-bearing $p21^{WT}$ and $p21^{CE}$ mice at weeks 8 and 12; n = 3–4 mice/group.

(B) Flow cytometry quantification of total monocytes, neutrophils, and $Ly6C^{hi}$ monocytes in blood of non-tumor-bearing $p21^{WT}$ and $p21^{CE}$ mice; n = 7–9 mice/group.

(C) Flow cytometry quantification of monocytes, neutrophils, and macrophages in the spleens of 8–12 weeks $p21^{WT}$ and $p21^{CE}$ non-tumor-bearing mice; n = 7–9 mice/group.

(D) Flow cytometry analysis of the number of monocytes, neutrophils, cDC2s, and cDC1s in the pancreas of $p21^{CE}$ and $p21^{WT}$ mice bearing orthotopic KP-2 tumors; n = 6 mice/group.

(E) Flow cytometry quantification of $Ly6C^{hi}$ monocytes, $Ly6C^{low}$ monocytes, and granulocytes in the bone marrow of tumor-bearing $p21^{CE}$ and $p21^{WT}$ mice; n = 6 mice/group.

(F) Flow cytometry quantification of myeloid cells in the blood of tumor-bearing $p21^{CE}$ and $p21^{WT}$ mice; n = 6 mice/group.

All graphs are expressed as the mean ± SEM. n.s., not significant; *$p < 0.05$. For comparisons between any two groups, the Student's two-tailed *t*-test was used.

Fig. S4

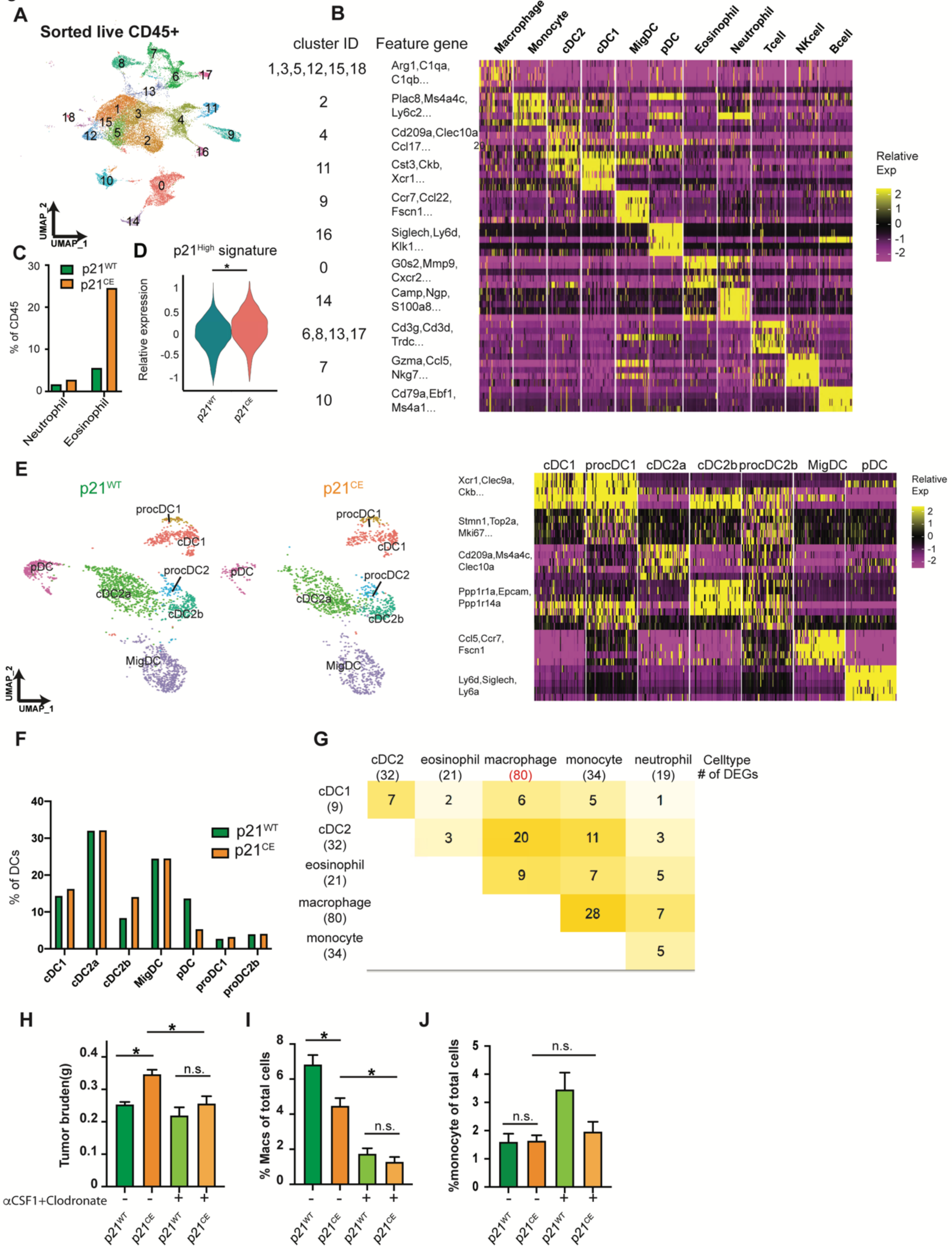
A
Sorted live CD45+
8
7
6
17
13
18
1
3
11
15
4
12
5
2
9
16
10
0
14
UMAP_2
UMAP_1
B
cluster ID
Feature gene
Macrophage
Monocyte
cDC2
cDC1
MigDC
pDC
Eosinophil
Neutrophil
Tcell
NKcell
Bcell
1,3,5,12,15,18
Arg1,C1qa,
C1qb...
2
Plac8,Ms4a4c,
Ly6c2...
4
Cd209a,Clec10a
Ccl17...
11
Cst3,Ckb,
Xcr1...
9
Ccr7,Ccl22,
Fscn1...
16
Siglech,Ly6d,
Klk1...
0
G0s2,Mmp9,
Cxcr2...
14
Camp,Ngp,
S100a8...
6,8,13,17
Cd3g,Cd3d,
Trdc...
7
Gzma,Ccl5,
Nkg7...
10
Cd79a,Ebf1,
Ms4a1...
Relative
Exp
2
1
0
-1
-2
C
30
20
10
0
% of CD45
p21^WT
p21^CE
Neutrophil
Eosinophil
D
p21^High signature
*
Relative expression
1
0.5
0
-0.5
-1
p21^WT
p21^CE
E
p21^WT
p21^CE
procDC1
cDC1
pDC
procDC2
cDC2a
cDC2b
MigDC
UMAP_2
UMAP_1
cDC1
procDC1
cDC2a
cDC2b
procDC2b
MigDC
pDC
Xcr1,Clec9a,
Ckb...
Stmn1,Top2a,
Mki67...
Cd209a,Ms4a4c,
Clec10a
Ppp1r1a,Epcam,
Ppp1r14a
Ccl5,Ccr7,
Fscn1
Ly6d,Siglech,
Ly6a
Relative
Exp
2
1
0
-1
-2
F
40
30
20
10
0
% of DCs
p21^WT
p21^CE
cDC1
cDC2a
cDC2b
MigDC
pDC
proDC1
proDC2b
G
cDC2 (32)
eosinophil (21)
macrophage (80)
monocyte (34)
neutrophil (19)
Celltype
# of DEGs
cDC1 (9)
7
2
6
5
1
cDC2 (32)
3
20
11
3
eosinophil (21)
9
7
5
macrophage (80)
28
7
monocyte (34)
5
H
Tumor bruden(g)
0.4
0.3
0.2
0.1
0
*
*
n.s.
αCSF1+Clodronate
-
-
+
+
p21^WT
p21^CE
p21^WT
p21^CE
I
% Macs of total cells
8
6
4
2
0
*
*
n.s.
-
-
+
+
p21^WT
p21^CE
p21^WT
p21^CE
J
%monocyte of total cells
5
4
3
2
1
0
n.s.
n.s.
-
-
+
+
p21^WT
p21^CE
p21^WT
p21^CE

Figure S4.

(A) UMAP plot of all sorted CD45$^+$ cell clusters on merged objects from p21^{CE} and p21^{WT} KP-2 orthotopic tumor-bearing mice. Three mice were pooled for each genotype.

(B) Heat map listing all clusters in **A** and corresponding cell type annotations and key gene expressions.

(C) Bar plot displaying the percentages of neutrophils and eosinophils in p21^{WT} and p21^{CE} tumor-bearing mice.

(D) Violin plot displaying the expression levels of p21^{High} signature scores, identified in **Fig. 4 M**, in TAMs from p21^{CE} and p21^{WT} mice. *Wilcox adjusted p.value < 0.05.

(E) UMAP plot of the reclustered DC populations in **Fig. 6 A**, annotated with cell type and associated key gene expressions in the heat map (right).

(F) Quantification of major DC populations identified in **D** from p21^{CE} tumors when compared with p21^{WT} tumors.

(G) Heat map showing the number of shared differentially-expressed genes (DEGs) between two genotypes in each cell population, including macrophage and close lineages. The number of DEGs for each single cell population when comparing p21^{CE} to p21^{WT} was listed in the parenthesis below.

(H-J) Bar plot showing the tumor burden, percentages of tumor-associated macrophages and monocytes in p21^{WT} and p21^{CE} mice bearing orthotopic KP-2 tumors with or without colony stimulating factor-1 and clodronate treatment; n = 8–10 mice/group. n.s., not significant; *p < 0.05. For comparisons between any two groups, the Student's two-tailed *t*-test was used.

Fig. S5


A
Upregulated Pathway
FDR VALUE
GALINDO_IMMUNE_RESPONSE_TO_ENTEROTOXIN <0.01
HALLMARK_TNFA_SIGNALING_VIA_NFKB <0.01
INFLAMMATORY RESPONSE <0.01
HALLMARK_INFLAMMATORY_RESPONSE <0.01
NEUTROPHIL DEGRANULATION <0.01
HALLMARK_IL6_JAK_STAT3_SIGNALING <0.01
Inflammatory Response
BP:CELL ADHESION <0.001
BP: BIOLOGICAL ADHESION <0.001
BP:CELL MIGRATION <0.001
BP: LOCOMOTION <0.001
BP: CELL-CELL ADHESION <0.001
BP: CELL MOTILITY <0.001
Adhesion & Migration
ZWANG_CLASS_3_TRANSIENTLY_INDUCED_BY_EGF <0.01
KIM_WT1_TARGETS_UP <0.01
PROTEOGLYCANS IN CANCER <0.001
EXTRACELLULAR MATRIX ORGANIZATION <0.01
HALLMARK_ANGIOGENESIS <0.01
CELL SURFACE INTERACTIONS AT THE VASCULAR WALL <0.01
Angiogenesis
BILD_HRAS_ONCOGENIC_SIGNATURE <0.01
ERK1 AND ERK2 CASCADE <0.001
SIGNALING RECEPTOR BINDING <0.001
HALLMARK_MTORC1_SIGNALING <0.01
CYTOKINE_CYTOKINE RECEPTOR INTERACTION <0.001
IL-17 SIGNALING PATHWAY <0.001
Cell Signaling
HALLMARK_HYPOXIA <0.01
WINTER_HYPOXIA_METAGENE <0.01
PID_HIF_TFPATHWAY <0.01
HIF-1 SIGNALING PATHWAY <0.001
Hypoxia
HALLMARK_EPITHELIAL_MESENCHYMAL_TRANSITION <0.01
HEMOSTASIS <0.01
HALLMARK_GLYCOLYSIS <0.01
PHAGOSOME <0.001
Other
0
2
4
NES
Downregulated Pathway
FDR VALUE
MITOCHONDRIAL PROTEIN COMPLEX <0.01
RIBOSOME <0.01
MOOTHA_VOXPHOS <0.01
WONG_MITOCHONDRIA_GENE_MODULE <0.01
LARGE RIBOSOMAL SUBUNIT <0.01
RESPIRATORY CHAIN <0.01
Respiration Metabolism
MITOCONDRIAL TRANSLATION TERMINATION <0.01
MITOCHONDRIAL TRANSLATION ELONGATION <0.01
MITOCHONDRIAL TRANSLATION <0.01
INNER MITOCHONDRIAL MEMBRANE PROTEIN COMPLEX <0.01
TRANSLATION <0.01
Translation Protein degradation
HALLMARK_E2F_TARGETS <0.01
ZHOU_CELL_CYCLE_GENES_IN_IR_RESPONSE_24HR <0.01
DNA REPLICATION <0.01
DNA RECOMBINATION <0.01
CELL CYCLE <0.01
DNA-DEPENDENT DNA REPLICATION <0.01
Cell Cycle
KOBAYASHI_EGFR_SIGNALING_24HR_DN <0.01
HALLMARK_INTERFERON_ALPHA_RESPONSE <0.01
Cell signaling
-6
-4
-2
0
NES

Figure S5.

(A) Bar plot showing significantly upregulated and downregulated pathways identified by GSEA in tumor-associated macrophages from $p21^{CE}$ compared with $p21^{WT}$ mice. The pathways were grouped into biological functions with a false discovery rate < 0.01.

Table S1: Array top regulated genes sip21 vs. siNT; n = 3 each.

Top downregulated genes

GeneSymbol	Fold Change (sip21o2 vs siNT)	adjusted p	Fold Change (sip21o3 vs siNT)	adjusted p
Hfm1	-9.000967	4.17E-06	-9.551253	3.30E-06
Olfr356	-6.310875	0.000277	-6.7342	0.000213
Cnn1	-4.243251	2.60E-05	-4.088136	3.23E-05
Supt3	-3.3844	6.81E-05	-5.437286	4.28E-06
Cdkn1a	-2.804869	1.44E-07	-5.631165	1.15E-09
Ear7	-2.404938	1.27E-06	-2.886804	2.29E-07
Cdkn1a	-2.396397	4.53E-07	-3.167768	3.54E-08
Spint1	-1.945373	0.000275	-2.055021	0.00015
Spint1	-1.826354	5.97E-05	-1.544564	0.000716
Slc36a2	-1.781509	2.15E-05	-1.581507	0.00014
Ldhb	-1.71729	0.000103	-1.817892	4.60E-05
0610009E02Rik	-1.704009	0.000111	-1.568371	0.000405
Hpgd	-1.689703	7.12E-05	-1.759566	3.89E-05
Rcbtb2	-1.67373	4.01E-05	-1.513442	0.000225
Gm9733	-1.579973	0.000145	-1.708255	4.09E-05
Aldoc	-1.547172	6.71E-06	-1.556962	5.93E-06
Ppp1r9a	-1.54189	5.78E-05	-1.602184	2.88E-05
Sult1a1	-1.538296	0.000123	-1.649467	3.66E-05
Cib2	-1.522033	0.000125	-1.524215	0.000121

Top 50 upregulated genes

GeneSymbol	Fold-change (sip21o2 vs TCM)	adjusted p	Fold-change (sip21o3 vs TCM)	adjusted p
Rrm2	-6.30647	3.17E-11	-7.95356	1.02E-11
Cdkn3	-6.28505	8.43E-10	-6.7755	5.76E-10
Pif1	-6.25111	2.88E-07	-8.06132	8.74E-08
Cxcl9	-5.11269	1.94E-05	-5.20062	1.78E-05
Hmmr	-4.85418	3.20E-05	-5.03176	2.65E-05
Hmmr	-4.31765	9.85E-05	-4.58722	7.12E-05
Mastl	-4.07957	9.67E-07	-4.21229	7.90E-07
Casc5	-3.96834	4.20E-05	-5.70901	5.80E-06
Pif1	-3.89545	2.18E-05	-4.68433	7.38E-06
Fancd2	-3.83321	2.11E-05	-4.92167	4.91E-06
Esco2	-3.67204	6.75E-06	-5.21945	8.15E-07
D17H6S56E-5	-3.60167	1.85E-08	-4.03994	8.27E-09
Mastl	-3.59825	4.18E-06	-4.83099	6.63E-07
Kif2c	-3.54186	1.80E-06	-4.37275	4.51E-07
Nek2	-3.52283	2.45E-08	-4.65013	3.78E-09
2010110K18Rik	-3.49874	1.67E-05	-4.71255	2.65E-06
Cdca2	-3.46713	0.000389	-4.92359	5.65E-05
Dlgap5	-3.41372	9.11E-08	-4.60248	1.20E-08
Xkr5	-3.39351	0.000359	-4.19719	0.000105
Foxm1	-3.38906	8.91E-08	-4.27792	1.76E-08

Prc1	-3.34136	3.54E-09	-4.5658	4.01E-10
Fbxo48	-3.29161	7.43E-06	-4.39264	1.10E-06
Prc1	-3.25269	3.85E-07	-4.169	6.68E-08
Sgol1	-3.21025	8.10E-07	-3.98796	1.72E-07
BC030867	-3.20821	2.85E-08	-4.46017	2.75E-09
Depdc1a	-3.19559	0.000114	-3.78934	3.79E-05
Ckap2l	-3.17264	0.000106	-4.27054	1.62E-05
Kifc5b	-3.13167	0.000538	-4.41533	7.18E-05
Cenpf	-3.11857	7.64E-05	-3.32338	4.92E-05
Nusap1	-3.0947	2.82E-09	-4.11654	3.34E-10
Kif4	-3.09329	0.000319	-3.63404	0.000115
Kifc1	-3.0841	5.61E-05	-3.56142	2.08E-05
Kif18b	-3.08083	1.24E-05	-4.31059	1.26E-06
Prc1	-3.07972	0.0001	-3.4257	4.83E-05
Rad51	-3.07141	6.81E-08	-3.88828	1.15E-08
Pbk	-3.06893	7.85E-06	-3.44022	3.38E-06
Aspm	-3.06868	1.39E-06	-4.04615	1.89E-07
Sgol1	-3.0153	1.27E-07	-4.3219	9.18E-09
Rad51ap1	-3.01418	2.51E-08	-4.12435	2.40E-09
Ccna2	-3.01189	1.32E-06	-3.30825	6.34E-07
Rad51ap1	-2.99682	1.99E-06	-3.89215	2.92E-07
Efcab6	-2.99481	2.19E-05	-2.63158	6.16E-05
Fam64a	-2.98438	8.13E-08	-4.08292	7.76E-09
Shcbp1	-2.9764	0.000173	-3.27637	8.95E-05
Ccnb2	-2.97509	1.24E-08	-3.76131	1.98E-09

Ccnb1	-2.97083	2.59E-09	-4.04031	2.45E-10
Cdc20	-2.96576	7.65E-08	-3.80712	1.12E-08
Ccnb1	-2.96254	2.22E-07	-3.57911	5.06E-08
Anln	-2.95577	1.58E-05	-3.15593	9.56E-06

Table S2: Sequences of siRNAs targeting p21 and CSF1

Clone Name	Target Gene ID	Sequence
mm.Ri.Cdkn1a.13.3	NM_007669 NM_001111099	5'rCrUrGrArCrArGrArUrUrUrCrUrArUrCrArCrGrCrUrUrGrGrArGrUrGrArUrArGrArArA
mm.Ri.Cdkn1a.13.2	NM_007669 NM_001111099	5'rArCrArGrUrCrCrUrArCrUrGrArUrArUrCrArGrArUrGrGrGrUrUrGrArUrArUrCrArGrU
mm.Ri.Csf1.13.1	NM_001113530 NM_007778 NM_001113529	5'rGrCrArGrCrAGrUrUrGrArUrCrGrArCrArCrArUrUrUrGrArCrUrGrUrCrGrArUrCrArA
mm.Ri.Csf1.13.2	NM_001113530 NM_007778 NM_001113529	5' rCrArGrGrUrGrGrArArCrUrGrCrCrArGrUrCrUrUrUrCrUrArUrArCrUrGrGrCrArGrUrU
siNC	Negative Control(DS NC1)	na
Primer:ROSA-CAG-ES-PC-For	This paper	5'CTAAAGAAGAGGCTGTGCTTTGGGGCTCVG
Primer:CAG-R2	This paper	5' CTCCACCCATTGACGTCAATGGAAAGTCCC
Primer:BGH-F3	This paper	5' CGACTGTGCCTTCTAGTTGCCAGCCATCTG
Primer:ROSA-R10	This paper	5' CACTTGTGGTCTTCAGACACACCAGAAGAG
Primer:ROSA-WT-F1	This paper	5'GTTATCAGTAAGGGAGTGCAGTGGAGTAG
Primer:ROSA-WT-R1	This paper	5'CCGAAAATCTGTGGGAAGTCTTGTCCCTCC
Primer:CAG-R2	This paper	5'CTCCACCCATTGACGTCAATGGAAAGTCCC

Primer:12427	C.Deng et.al(Deng et al., 1995)	5' GTTGTCCTCGCCCTCATCTA
Primer:12428	C.Deng et.al(1)	5' GCCTATGTTGGGAAACCAGA
Primer:12429	C.Deng et.al(1)	5' CTGTCCATCTGCACGAGACTA
Primer:oIMR3067	B E Clausen et.al(Clausen et al., 1999)	5' CTTGGGCTGCCAGAATTTCTC
Primer: oIMR3066	B E Clausen et.al(Clausen et al., 1999)	5' CCCAGAAATGCCAGATTACG
Primer:oIMR3068	B E Clausen et.al(Clausen et al., 1999)	5' TTACAGTCGGCCAGGCTGAC

1695
1696
1697 Table S3: Antibody list for flow cytometry

Name	Identifier	Clone#	Company	Dilution
CD45	RRID:AB_469625	30-F11	eBioscience	1:400
CD3e	RRID:AB_469315	145-2C11	eBioscience	1:200
CD4	RRID:AB_464900	RM4-4	eBioscience	1:200
CD8a	RRID:AB_2732919	53-6.7	BD Biosciences	1:200
Foxp3	RRID:AB_11218094	FJK-16s	eBioscience	1:100
CD19	RRID:AB_1659676	eBio1D3	eBioscience	1:200
CD11b	RRID:AB_657585	M1/70	eBioscience	1:400
CD11c	RRID:AB_1548652	N418	eBioscience	1:200
Ly6C	RRID:AB_1518762	HK1.4	eBioscience	1:400
Ly6G	RRID:AB_1186104	1A8	BioLegend	1:400
F4/80	RRID:AB_468798	BM8	eBioscience	1:400

MHCII	RRID:AB_1272204	M5/115.15.2	eBioscience	1:400
CD24	RRID:AB_464985	30-F1	eBioscience	1:200
CD44	RRID:AB_1272246	IM7	eBioscience	1:200
CD62L	RRID:AB_11125577	MEL-14	BioLegend	1:100
Flt3	RRID:1B_1877218	A2F10	BioLegend	1:20
CD115	RRID:AB_467428	AFS98	eBioscience	1:50
B220	RRID:AB_396673	RA3-6B2	eBiosciences	1:100
gdTCR	RRID:AB_842756	eBioGl3	eBioscience	1:200
Nk1.1	RRID:AB_467736	PK136	eBioscience	1:100
Sca1	RRID:AB_467778	D7	BioLegend	1:100
Cd49b	RRID:AB_395093	DX5	eBioscience	1:200

Table S4: Antibody list for multiplex immunochemistry (mpIHC) and immunoblotting

Name	Identifier	Clone#	Company	Dilution
P21	Ab188224	EPR18021	Abcam	1:200
Ck19	RRID:AB_469315	145-2C11	eBioscience	1:200
Ki-67	12202	D3B5	Cell Signaling	1:400
Podoplanin	Ab11936	RTD4E10	Abcam	1:800
F4/80	70076	D2S9R	Cell Signaling	1:200
pp65	3033	93H1	Cell Signaling	1:500
Cyclin d1	2926	DCS6	Cell Signaling	1:500
c-Myc	13987	D3N8F	Cell Signaling	1:500
P27	3686	D69C12	Cell Signaling	1:500

1705 Table S5: Antibody list for human mass cytometry time of flight

REAGENT or RESOURCE	SOURCE	IDENTIFIER
anti-human CD11b (ICRF44)	Fluidigm	#3209003B
anti-human CD11c (Bu15)	Fluidigm	#3159001B
anti-human CD14 (M5E2)	Fluidigm	#3160001B
anti-human CD141 (1A4)	Fluidigm	#3173002B
anti-human CD15 (W6D3)	Fluidigm	#3164001B
anti-human CD16 (3G8)	Fluidigm	#3148004B
anti-human CD163 (GHI/61)	Fluidigm	#3154007B
anti-human CD19 (HIB19)	Fluidigm	#3142001B
anti-human CD192 (CCR2) (K036C2)	Fluidigm	#3153023B
anti-human CD1c (L161)	BioLegend	#331502
anti-human CD20 (2H7)	Fluidigm	#3147001B
anti-human CD206 (MMR) (15-2)	Fluidigm	#3168008B
anti-human CD24 (ML5)	Fluidigm	#3166007B
anti-human CD3 (UCHT1)	BioLegend	#300402
anti-human CD32 (FUN-2)	Fluidigm	#3169020B
anti-human CD34 (581)	Fluidigm	#3149013B
anti-human CD38 (HIT2)	Fluidigm	#3167001B
anti-human CD40 (5C3)	Fluidigm	#3165005B
anti-human CD45 (HI30)	Fluidigm	#3089003B
anti-human CD54 (HA58)	Fluidigm	#3170014B
anti-human CD56 (NCAM16.2)	Fluidigm	#3176008B
anti-human CD64 (10.1)	Fluidigm	#3146006B
anti-human CD68 (Y1/82A)	Fluidigm	#3171011B

anti-human CD80 (2D10.4)	Fluidigm	#3162010B
anti-human CD81 (5A6)	Fluidigm	#3145007B
anti-human CD82 (ASL-24)	Fluidigm	#3158025B
anti-human CD86 (IT2.2)	Fluidigm	#3150020B
anti-human CX3CR1 (2A9-1)	Fluidigm	#3172017B
anti-human CXCR4 (12G5)	Fluidigm	#3175001B
anti-human HLA-DR (L243)	Fluidigm	#3174001B
anti-human Ki-67 (B56)	Fluidigm	#3161007B
Anti-human PCNA(PC10)	Abcam	Ab29
Anti-human p21(12D1)	CellSignal	2947

Table S6: Antibody list for mouse mass cytometry time of flight (CyTOF)

REAGENT or RESOURCE	SOURCE	Catalog
anti-mouse CD44(IM7)	Leinco	C382
anti-mouse GITR(DTA-1)	BioXcell	BE0063
anti-mouse CD25(PC61)	Leinco	C1194
anti-mouse CD38(90)	eBioscience	14-0381-82
anti-mouse CD90(G7)	Biolegend	105202
anti-mouse Lag-3(C9B7W)	Leinco	L306
anti-mouse CD27(LG.7F9)	eBioscience	50-124-94
anti-mouse KLRG1(2F1/KLRG1)	BioXCell	BE0201
anti-mouse CD103(2E7)	Biolegend	121402
Anti-mouse CD4(GK1.5)	BioXcell	BE0003-1
anti-mouse CD45(30-F11)	Fluidigm	3089005B
anti-mouse CD62L(MEL-14)	Leinco	C2118

anti-mouse ICOS(C398.4A)	eBioscience	14-9949-82
anti-mouse OX-40(OX-86)	BioXcell	BE0031
anti-mouse PD-1(RMP1-30)	eBioscience	14-9981-82
anti-mouse TIGIT(1G9)	BioXcell	BE0274
anti-mouse CD69(H1.2F3)	eBioscience	14-0691-82
anti-mouse TCRb(H57-597)	BioXcell	BE0102
anti-mouse CD127(A7R34)	BioXcell	BE0065
anti-mouse CD39(Duha59)	Biolegend	143802
anti-mouse NK1.1(PK136)	BioXcell	BE0036
anti-mouse CD8a(53-6.7)	Leinco	C375
anti-mouse TCRgd(GL3)	eBioscience	14-5711-82
anti-mouse Tim3(RMT3-23)	BioXcell	BE0115
anti-mouse 4-1BB(17B5)	BioLegend	106107
anti-mouse FoxP3(FJK-16s)	eBioscience	14-5773-82
anti-mouse GATA3(TWAJ)	eBioscience	14-9966-82
anti-mouse GranzymeB(GB11)	eBioscience	MA1-80734
anti-mouse CTLA-4(UC10-4B9)	eBioscience	50-129-16
anti-mouse Ki67(8D5)	Novus	NBP2-22112
anti-mouse TCF1(812145)	R&D	MAB8224
anti-mouse ROR-γτ(AFKJS-9)	eBioscience	14-6988-82
anti-mouse Eomes(Dan11mag)	eBioscience	50-245-556
Anti-mouse T-bet(4B10)	Biolegend	644802

Table S7: List of qPCR primers

Gene	Source	Assay ID

GAPDH	Taqman	Mm99999915_g1
TBP	Taqman	Mm01277042_m1
HPRT	Taqman	Mm03024075_m1
CCND1	Taqman	Mm00432359_m1
CCNE1	Taqman	Mm01266311_m1
CCNA2	Taqman	Mm00438063_m1
IFIT3	Taqman	Mm01704846_s1
CD40	Taqman	Mm00441891_m1
IFNA1	Taqman	Mm03030145_gH
IFNB1	Taqman	Mm00439546_s1
IRF1	Taqman	Mm01288580_m1
CDKN1A	Taqman	Mm04205640_g1
CSF1	Taqman	Mm00432686_m1
CXCL1	Taqman	Mm04207460_m1
CXCL2	Taqman	Mm00436450_m1
IL-1α	Taqman	Mm00439620_m1
IL-1β	Taqman	Mm00434228_m1
IL-6	Taqman	Mm00446190_m1
TNF-α	Taqman	Mm00443258_m1
IRF4	Taqman	Mm00516431_m1
TGF-β2	Taqman	Mm00436955_m1
TGF-β3	Taqman	Mm00436960_m1
YM1	Taqman	Mm00657889_mH
BATF	Taqman	Mm00479410_m1

c-Myc	Taqman	Mm00487804_m1
CCL2	Taqman	Mm00441242_m1

Table S8: Experimental Models: Organisms/strains

Strain	Source	Identifier
Mouse:B6.Cg-ROSA26tm1$^{\text{(LSL-p21-YFP)}}$	This paper	N/A
Mouse:C57BL/6J	The Jackson Laboratory	Stock# 000664
Mouse:B6.129S6(Cg)-Cdkn1a$^{\text{tm1Led}}$	The Jackson Laboratory	Stock # 016565
Mouse:B6.129p2-lyz2$^{\text{tm1(cre)ifo}}$	The Jackson Laboratory	Stock # 004781
Mouse:B6.p48-Cre;Kras$^{\text{LSL-G12D}}$;Trp53$^{\text{fl/fl}}$ i.e. KPC	N/A	N/A

Table S9: Software and Algorithms

Flowjo v10.7.2	Flowjo, L.L.C.	Flowjo, L.L.C.
Prism v9	Graphpad	www.graphpad.com
Docker	Rocker/rstudio:latest	https://hub.docker.com/r/rocker/rstudio
	cumulusprod/cellranger:4.0.0	https://hub.docker.com/r/cumulusprod/cellranger/tags
HALO v3.2.1851	Indica Labs-High Plex Fv4.0.3	https://indicalab.com/products/high-plex-fl/
	Indica Labs-Deconvolution v1.0.4	
Cytobank	Cytobank, Inc	Wustl.cytobank.org
FACSDiva	BD Biosciences	RRID: SCR_001456
Zen	Zeiss	Zeiss.com
Morpheus	Broad Institute	https://software.broadinstitute.org/morpheus/
Fiji v2.0.0	ImageJ	

R v3.6.3	R Core Team	https://cran.r-project.org/bin/windows/base/old/3.6.3/
	Clusterprofiler (Wu et al., 2021)	https://github.com/YuLab-SMU/clusterProfiler
	Seurat v 3.2.0(Stuart et al., 2019)	https://satijalab.org/seurat/
	Harmony(Korsunsky et al., 2019)	https://github.com/immunogenomics/harmony
	CATALYST(Nowicka et al., 2017)	https://github.com/HelenaLC/CATALYST

Table S10: Chemicals and recombinant proteins

Reagent	Source	Identifier
CSF1 neutralizing antibody(Clone 5A1)	BioXCell	BE0204
CSF1R depleting antibody(Clone AFS98)	BioXCell	BE0213
PBS Liposomes & Clodronate Liposomes	Liposoma	CP-005-005
Recombinant murine CSF1 peptide	Peprotech	315-02
Carboxyfluorescein succinimidyl ester(CFSE)	Invitrogen	C1157
Tamoxifen	Sigma-Aldrich	T5648
Halt Protease and Phosphatase Inhibitor	Thermo Scientific	78442
RIPA Buffer(10x)	Cell Signaling	UN3082
CD45 MicroBeads	Miltenyi Biotec	130-052-301

Table S11: Critical commercial assays

Resources	Source	Catalog number
Supersignal West Dura	Thermo	34075
FITC BrdU Flow Kit	BD Bioscience	557891
APC BrdU Flow Kit	BD Bioscience	557892
Proteome Profiler Mouse XL Cytokine Array	R&D systems	ARY028

E.Z.N.A. Total RNA Kit I	Omega	R6834-02
Taqman Gene Expression Master Mix	Thermo Fisher	4370074
qScript cDNA Supermix kit	Quantabio	95048-500
BOND Polymer Refine Detection Kit	Leica	DS9800
BOND Polymer Refine Red Detection Kit	Leica	DS9390
BOND Intense R Detection Kit	Leica	DS9263
Cytofix Kit	BD Bioscience	554655
MACS LS kit	Miltenyi	130042401
Mouse Macrophage Nucleofector Kit	Lonza	VPA-1009
Latex Beads-Rabbit IgG-PE Complex	Cayman	600541
Mouse M-CSF Matched Antibody Pair Kit	Abcam	Ab218788
Pierce BCA Protein Assay Kit	Thermo Scientific	23225
DuoSet ELISA Mouse M-CSF	R&D system	DY416-05
DuoSet Ancillary Reagent Kit2	R&D system	DY008